The Upper Atmospheric Fountain Effect in the Polar Cusp Region

Von der Fakultät für Elektrotechnik, Informationstechnik, Physik
der Technischen Universität Carolo-Wilhelmina
zu Braunschweig
zur Erlangung des Grades einer
Doktorin der Naturwissenschaften
(Dr.rer.nat.)
genehmigte
Dissertation

von Stefanie Rentz
aus Brandenburg

1. Referent: Prof. Dr. Hermann Lühr
2. Referent: Prof. Dr. Gerd W. Prölss
3. Referent: Prof. Dr. Andreas Hördt
eingereicht am 4. Dezember 2008
mündliche Prüfung (Disputation) am 11. März 2009
2009
(Druckjahr)

Vorveröffentlichungen der Dissertation

Teilergebnisse aus dieser Arbeit wurden mit Genehmigung der Fakultät für Elektrotechnik, Informationstechnik, Physik, vertreten durch die Mentorin oder den Mentor/die Betreuerin oder den Betreuer der Arbeit, in folgenden Beiträgen vorab veröffentlicht:

Publikationen:

- Rentz, S. and H. Lühr: Climatology of the cusp-related thermospheric mass density anomaly, as derived from CHAMP observations, Ann. Geophys., 26, 2807–2823, 2008.

Tagungsbeiträge:

- Rentz, S. and H. Lühr: Observation and modelling of the upper atmospheric density and winds and their dependence on geomagnetic activity, DFG SPP meeting, Kühlungsborn, Deutschland, Mai 2006.
- Rentz, S. and H. Lühr: THERMOCUSP - Density enhancements in the thermospheric cusp region, CAWSES SPP meeting, Bonn - Bad Godesberg, Deutschland, Januar 2007.
- Rentz, S., H. Lühr, K. Häusler and W. Köhler: Statistical studies on local thermospheric cusp density enhancements. IUGG-IAGA 2007, Perugia, Italien, Juli 2007.
- Rentz, S., H. Lühr and M. Rietveld: Combined CHAMP-EISCAT studies on local thermospheric mass density enhancements in the cusp, 13th International EISCAT Workshop 2007, Mariehamn, Finnland, August 2007.
- Rentz, S. and H. Lühr: Density enhancements in the thermospheric cusp region, GFZ PHD Day, Potsdam, Deutschland, November 2007.
- Rentz, S., H. Lühr and M. Rietveld: Dichteanomalien in der thermosphärischen Cusp-Region, beobachtet mit CHAMP, DPG Frühjahrstagung 2008 - Fachverband Extraterrestrische Physik, Freiburg, Deutschland, März 2008.
- Rentz, S. and H. Lühr: Cusp-related thermospheric mass density, observed with CHAMP, 2008 CEDAR Workshop, Zermatt Resort, Midway, UT, USA, Juni 2008.
- Rentz, S. and H. Lühr: Climatology of the cusp-related thermospheric mass density, as observed by CHAMP, DFG SPP Meeting, Berlin, Deutschland, September 2008.

- Rentz, S. and H. Lühr: EISCAT - European Incoherent Scatter Radar, PHD Day 2008, Potsdam, Deutschland, Dezember 2008.

Summary

The thermosphere and the ionosphere are highly coupled and influence each other in many ways. The high-latitude upper atmosphere has been investigated for more than 75 years but only recently it has gained attention also in the modeling community, for instance in simulating the neutral fountain effect in the polar cusp. The polar cusp is the confined region where the magnetic field lines from the magnetopause reach the ionosphere. In the cusp, penetration of magnetosheath particles is most direct. The CHAMP satellite experiences a significant deceleration when crossing the polar cusp regions. This effect has been prompted a thesis in which the obvious influence of the geomagnetically-induced cusp region on the neutral upper atmospheric dynamics has been investigated in detail. Therefore, the total mass density, as derived from the accelerometer readings onboard CHAMP, has been studied extensively. It reveals a significant enhancement in the vicinity of the cusp, only visible if displayed in geomagnetic coordinates. The cusp-related density anomaly is investigated climatologically in a statistical analysis. It has been found to be a continuous phenomenon in the dayside auroral regions of both hemispheres, which is driven partly by the strength of the solar flux (indicated by the solar flux index, P10.7), but more directly by the energy input of the solar wind (indicated by the merging electric field), and is depending on the background density. The amplitude of the anomalies strongly depends on P10.7. In a 2D-correlation analysis it has been revealed that an increase in density is proportional to the square of the merging electric field and that the merging electric field in mV/m has a weight that is by more than 50 times higher than that of P10.7 in solar flux units concerning the dependence of the density anomaly on these both parameters. The ambient air density has been found to be a prime controlling parameter of the amplitude. The northern hemispheric density anomaly amplitudes exceed the southern hemispheric ones by a factor of 1.6 - possibly a consequence of the larger offset between geographic and geomagnetic poles in the South. A neutral fountain effect in the polar cusp region has been considered as the cause of the density anomaly. Its activating mechanisms have been investigated by considering a combined CHAMP-EISCAT campaign, a model study on soft particle precipitation, and an analysis of periodic density anomaly variations and their controlling parameters. The CHAMP-EISCAT campaign has been executed to simultaneously observe the neutral thermospheric characteristics (with CHAMP) and the ionospheric parameters (with EISCAT incoherent scatter radar facilities). As a result, the Pedersen conductivity was found to peak at 140 km altitude, i.e. above the E region as it would have been expected for typical E region Joule heating. Joule heating has been assumed to be one of the main sources of the neutral fountain effect. Joule heating rates of up to 0.016 W/m^2 are obtained in the vicinity of the cusp. These values are larger than reported before from a similar campaign, probably due to the fact that we have been taken into account both the large-scale and the small-scale components of the effective electric field. Particle precipitation events have been found to enhance the conductivity layer, thus lifting up the altitude of effective Joule heating (e.g. to 140 km). This might change the heated population in favour of heavier particles to be transported upward. The harmonic analysis has been revealed that the solar wind provides the energy for forming the cusp-related density anomaly.

According to the results of this thesis the following mechanism is suggested to cause the cusp-related density anomaly: The energy input by the solar wind, as characterised by the merging electric field, provides the power for Joule heating of preferably neutral molecules. Soft particle precipitation in the cusp simultaneously enhances the altitude of maximal Pedersen conductivity, thus lifting up the heated layer in the cusp. The cusp-related density anomaly is then caused by local composition changes in the upper atmosphere due to the differential expansion of heavier particles. The density enhancement is more intensive during phases of high solar activity, i.e. a larger background density favours the formation of large anomalies.

The atmospheric fountain in the cusp region affects the upper atmosphere globally. The harmonic exitation of the fountain in 2005 caused a global density variation of the thermosphere.

Zusammenfassung

Die Thermosphäre und die Ionosphäre sind eng miteinander verkoppelt und beeinflussen sich gegenseitig in mannigfältiger Weise. Bereits seit mehr als 75 Jahren ist die polare Hochatmosphäre Gegenstand wissenschaftlicher Forschung, doch erst in letzer Zeit findet sie auch verstärkt Eingang in Modellstudien, z.B. bei der Simulation der Neutralgasfontäne in der polaren Cusp-Region. Die Cusp polarer Breiten ist das räumlich und zeitlich sehr begrenzte Gebiet, in dem die Magnetfeldlinien von der Magnetosphäre bis zur Ionosphäre reichen. Hier können Teilchen aus der Übergangsregion direkt in die Erdatmosphäre eindringen. Der Kleinsatellit CHAMP erfährt eine deutliche Abbremsung, wenn er die Cusp durchfliegt. Durch diesen Effekt wurde die vorliegende Dissertation angeregt, denn es liegt nahe zu untersuchen, warum die Cusp als Merkmal des Erdmagnetfeldes die Dynamik der (neutralen) Hochatmosphäre beeinflusst. Deshalb wurde das Verhalten der thermospärischen Gesamtmassendichte, die aus Beschleunigungsmessungen an Bord von CHAMP abgeleitet werden kann, analysiert und dabei eine signifikante Dichteerhöhung im Bereich der Cusp gefunden. Diese ist allerdings nur bei Auftragung in geomagnetischen Koordinaten, nicht jedoch in geografischen Koordinaten erkennbar. Die Dichteanomalie im Bereich der Cusp wurde in einer statistischen Analyse klimatologisch untersucht. Sie wurde als kontinuierliches Phänomen beider Hemisphären identifiziert, das zum Teil von der Stärke der solaren Aktivität, hauptsächlich aber vom Energieeintrag des Sonnenwindes und der Hintergrunddichte gesteuert wird. Die Amplitude der Dichteanomalie hängt stark vom Index des solaren Flusses, P10.7, ab. Eine 2D-Analyse ergab eine quadratische Abhängigkeit der Dichteanomalie vom Energieeintrag des Sonnenwindes. Dieser wird durch das sog. *merging electric field* in mV/m charakterisiert, dem zugleich eine mehr als 50-fache Wichtung gegenüber P10.7 (in 10^{-26} W m^{-2} Hz^{-1}) zukommt, wenn man die Abhängigkeit der Dichteanomalie von diesen beiden Parametern betrachtet. Als ein Hauptsteuerungsparameter der Dichteamplitude wurde die Hintergrunddichte identifiziert. Offenbar bedingt durch den größeren Abstand zwischen geografischem und geomagnetischem Pol auf der Südhalbkugel liegen die dortigen Dichteamplituden um das 1.6-fache unter den Werten der Nordhalbkugel. Das Aufsteigen von Luftmassen aus tieferen Schichten (Neutralgasfontäne) im Bereich der Cusp wird als Ursache der Dichteanomalie angesehen. Deren Auslösemechanismen wurden mit Hilfe einer kombinierten CHAMP- EISCAT-Kampagne, Modellstudien zum Einfall niederenergetischer Teilchen in der Cusp und einer harmonischen Analyse der Dichteanomalie und ihrer Steuerungsparameter untersucht. Die CHAMP-EISCAT-Kampagne wurde durchgeführt, um gleichzeitig die neutralen Merkmale der Thermosphäre (mit CHAMP) und die ionosphärischen Parameter (mit EISCAT-Radaranlagen) zu beobachten. Es stellte sich heraus, dass die Pedersen-Leitfähigkeit ihr Maximum bei 140 km Höhe aufwies, also oberhalb der E-Schicht, in der man es für den typischen Fall der Joule-Heizung in der E-Schicht erwartet hätte. Joule-Heizung wird als eine der Hauptursachen der Neutralgasfontäne angesehen. In der Cusp erreichte

die Joule-Heizrate einen Wert von 0.016 W/m^2. Dieser ist größer als Werte aus einer ähnlichen Kampagne, vermutlich, weil in unserem Fall sowohl die großskalige als auch die kleinskalige Komponente des effektiven elektrischen Feldes berücksichtigt wurde. Offensichtlich wird die Anhebung der Heizschicht (z.B. auf 140 km Höhe) durch Teilcheneinfall in der Cusp verursacht. Dadurch verändert sich die Population der aufgeheizten Luftmasse, möglicherweise zugunsten schwererer Partikel, die dann aufwärts transportiert werden. Aus der harmonischen Analyse geht hervor, dass die für das Entstehen der Dichteanomalie in der Cusp benötigte Energie aus dem Sonnenwind übertragen wird.

Ausgehend von den Ergebnissen dieser Dissertation wird folgender Mechanismus zur Entstehung der Neutralgasfontäne im Bereich der polaren Cusps vorgeschlagen: Der Energieeintrag durch den Sonnenwind (erkennbar am Verlauf des *merging electric field*) ermöglicht Joulesche Heizung des Neutralgases. Gleichzeitig wird durch Einfall niederenergetischer Teilchen in der Cusp die Höhe maximaler Pedersen-Leitfähigkeit und damit auch die Höhe der effektiven Heizschicht angehoben. Dadurch können auch schwerere Partikel aufsteigen und eine lokale Dichteerhöhung, die Dichteanomalie der Cusp, verursachen. Dieser Mechanismus ist in Phasen erhöhter solarer Aktivität stärker ausgeprägt, denn eine größere Hintergrunddichte bewirkt größere Amplituden der Dichteanomalie. Die Anregung der Neutralgasfontäne in der Cusp 2005 hatte eine globale Änderung der thermosphärischen Dichte zur Folge. Sie beeinflusst die Dynamik der Hochatmosphäre also weltweit.

Contents

List of Figures

List of tables

Essential symbols, acronyms and abbreviations

2D : 2-Dimensional

3D : 3-Dimensional

$\vec{a}$: Acceleration

A : Area

ACE : Advanced Composition Explorer satellite

AE : Geomagnetic Auroral Electrojet index

A_{eff} : Effective cross-sectional area

α : Angle between CHAMP's longitudinal axis and the along-track wind component

α_i : Observation direction

amu : Atomic mass unit

ap, Ap : Indices of geomagnetic activity

a_x, a_y : Acceleration components

A_x, A_y : Satellite's surface in x-, y-direction

$\vec{B}$: Magnetic field

B_E : East component of the magnetic field

B_h : Horizontal intensity of the magnetic field

B_N : North component of the magnetic field

$B_{||}$: Birkeland (parallel) current

B_{tot} : Total intensity of the magnetic field

B_v : Vertical intensity of the magnetic field

CAWSES : Climate and Weather of the Sun-Earth System

C_D : Drag coefficient

cgm : Corrected geomagnetic latitude

CHAMP : CHAllenging Minisatellite Payload satellite

CNES : Centre National d”Etudes Spatiales (French National Space Centre)

CTIP : Coupled Thermosphere-Ionosphere-Plasmasphere Model

DE-2 : Dynamics Explorer 2 satellite

δ : Solar declination

$\Delta\rho$: Cusp-related density anomaly

$\Delta\rho_{high}$: Density anomaly $> 1 \times 10^{-12}$ kg/m^3

$\Delta\rho_{max}$: Maximum of the density anomaly

DIDM : Digital Ion Drift-Meter

DMSP : Defense Meteorological Satellites Program
$d\rho_{rel}$: Background density
DS : December Solstice
E : East
$\vec{E}$: Electric field
$\vec{E}'$: Energy transfer from the magnetospheric electric field
$E_{||}$: Parallel part of the electric field
$E_{\perp}$: Perpendicular part of the electric field
E_{AC} : Small-scale component of the perpendicular electric field
E_{DC} : Large-scale component of the perpendicular electric field
E_e : Energy of (precipitating) electrons
EEJ : Equatorial Electro-Jet
E_i : Energy of (precipitating) ions
EISCAT : European Incoherent SCATter Radar
E_{merg} : Merging electric field
EMF : Earth Magnetic Field
ESA : European Space Agency
ESR : EISCAT Svalbard Radar
EUV : Extreme Ultra-Violet
F10.7 : Index for the strength of the solar activity
FAC : Field Aligned Current
$\vec{F}_B$: Magnetic force
$\vec{F}_e$: Electric force
FE : Error function
$\vec{F}_{Fr}$: Frictional force
FPI : Fabry-Pérot Interferometer
FWHM : Full Width at Half Maximum
γ : Direction of wind speed
γ_m : Optimal wind direction
GCM : General Circulation Model
GPS : Global Positioning System
GSM : Geo-Solar Magnetic coordinates
GUISDAP : Grand Unified Incoherent Scatter Data Analysis Program
GUVI : Global Ultra-Violet Imager
h : Altitude
H : Scale height
hmF2 : Height maximum of the F2 layer

i : Inclination
I : Amperage
$\vec{I}$: Current
IAGA : International Association of Geomagnetism and Aeronomy
IGRF : International Geomagnetic Reference Field
IMF : Interplanetary Magnetic Field
IMF B_x, B_y, B_z : Interplanetary Magnetic Field components
IR : Infra-Red
IRI : International Reference Ionosphere
ISR : Incoherent Scatter Radar
ISS : International Space Station
$\vec{j}$: Current density
$\vec{J}$: Electric current
j_e : Energy flux of (precipitating) electrons
J_H : Hall current
j_i : Energy flux of (precipitating) ions
J_P : Pedersen current
JS : June Solstice
kp, Kp : Planetary index of geomagnetic activity
KS-FAC : Kilometre-scale Field-Aligned Current
L : Conductance
λ : Wave length
LLBL : Low Latitude Boundary Layer
LSEM : Least-squares error minimisation (procedure)
LT : Local Time
m : Mass
Max : Maximum
m_e : Electron mass
ME : March Equinox
MFA : Magnetic Field Aligned
m_i : Ion mass
Min : Minimum
MJD : Modern Julian Day
MLT : Magnetic Local Time
m_{O+} : Mass of atomic oxygen ions
MSIS : Mass Spectrometer and Incoherent Scatter (Radar Model)
NmF2 : F2 layer peak electron density

μ_0 :	Magnetic constant
n :	Particle density
N :	North
NASA :	National Aeronautics and Space Administration
n_e :	Electron density
NH :	Northern Hemisphere
n_{N2} :	Density of molecular nitrogen
n_O :	Density of atomic oxygen
n_{O+} :	Density of atomic oxygen ions
n_{O2} :	Density of molecular oxygen
NRLMSIS-E00 :	Naval Research Laboratory Mass Spectrometer and Incoherent Scatter radar-Empirical atmospheric model
$\nu_{e,n}$:	Electron-neutral collision frequency
$\nu_{i,n}$:	Ion-neutral collision frequency
Ω_e :	Earth’s angular velocity
ω_{eB} :	Electron gyro-frequency
ω_{iB} :	Ion gyro-frequency
ONERA :	Office National d”Etudes et Recherches Aérospatiales (French Aerospace Laboratory)
p :	Pressure
P10.7 :	Index for the strength of the solar activity
PEJ :	Polar Electro-Jet
ϕ :	Geographic latitude
PLP :	Planar Langmuir Probe
p_m :	Magnetic pressure
POMME 3 :	POtsdam Magnetic Model of the Earth
q :	Charge
$q(h)$:	Height-dependent (Joule) heating rate
Q :	Height-integrated (Joule) heating rate
$Q_{.25}$, $Q_{.75}$:	Quantiles
R :	Correlation coefficient
R :	Resistance
R_E :	Earth radius
ρ :	(Thermospheric) total mass density
ρ_{400} :	Total mass density normed to 400 km altitude
ρ_{bias} :	Total mass density of the bias function
ρ_{ei} :	Density of charged particles

ρ_{MSIS} : Total mass density as derived from MSIS
S : South
SE : September Equinox
SH : Southern Hemisphere
SHL : Sheffield High-Latitude Model
σ_H : Hall conductivity
Σ_H : Hall conductance
$\sigma_{||}$: Parallel conductivity
σ_P : Pedersen conductivity
Σ_P : Pedersen conductance
SIRCUS : Satellite and Incoherent Scatter Radar Cusp Study
SM : Solar-Magnetic (coordinates)
SPIDR : Space Physics Interactive Data Resource
STAR : Space Three-axis Accelerometer for Research Missions
std : Standard deviation
$\Sigma O/N_2$: Column Density Ratio of O/N_2
SZA : Solar Zenith Angle
T_e : Electron temperature
TEC : Total Electron Content
θ : IMF clock angle
T_i : Ion temperature
U : Voltage
u_{cross_i} : Individual cross-track wind component
UHF : Ultra High Frequency
UT : Universal Time
UV : Ultra-Violet
$\vec{v}$: Neutral wind velocity
v_A : Alfvén velocity
$v_\perp$: Orbit velocity component perpendicular to the magnetic field
v_{c0} : Corotational wind component at the equator
v_i : Plasma drift velocity
VHF : Very High Frequency
v_{los} : Line-of-sight velocity
$v_{c\phi}$: Corotational wind component at latitude ϕ
v_{SW} : Solar wind speed
v_y : Transverse wind component
W : West

Chapter 1

Introduction

> *It is dangerous to misjudge the power of littleness; it resembles the power of a worm gnawing away an elm tree by eroding its bark.*
> *(Honoré de Balzac)*

The cusp. A little word. Only four letters. Nevertheless - or maybe even on account of this - it appears to be attended by a powerful meaning which seems to be more than the pure nomenclature of an atmospheric region.

Sometimes, journalists make use of such pithy sayings to concisely describe a complete issue. But leafing through the numerous scientific publications on high-latitude upper atmospheric research might suggest the impression that the little word cusp quite overtakes this part; see for instance Chisham et al. (2002), Neubert and Christiansen (2003), Ritter et al. (2004b), Liu and Lühr (2005), Rother et al. (2007), Förster et al. (2008), Buchert et al. (2008).

Actually, what is the cusp? This is illustrated in Section 2.3.
And why does this confined region play such an important role within the so much more voluminous thermosphere-ionosphere region?

We cannot answer this question. Instead, we want to make one step further than most of the publications on cusp issues. They address the ionised component of the upper atmosphere. This can easily be understood: The cusp-related activity is primarily referred to electromagnetic processes. We aim to focus on the neutral component of the dayside polar upper atmosphere and to examine its behaviour due to cusp-related impacts.

Our investigations are prompted by a case study (dedicated by Section 2.2.2) which reveales a significant deceleration of the CHAMP (CHAllenging Minisatellite Payload) spacecraft during cusp overflights. CHAMP provides the unique possibility to work on a dataset of continuous multi-year observations. Its coverage and resolution allows both time-relevant and global mapping and the detection of local phenomena like the cusp anomaly.

As described in Chapter 5 we make use of this dataset to investigate the behaviour of the thermospheric total mass density in the vicinity of the cusp statistically over a period of four years - not without searching for possible controlling parameters.

At this juncture, simulations of the empirical atmospheric model MSIS serve as a valuable comparison, in particular addressed in the Sections 4.4.3, 5.1, 5.5.1, and C.1.

However, the study of the controlling parameters alone cannot satisfy our curiosity. We intend to go one step further and examine possible causes of the detected density anomaly.
Well, this topic might be beat down in two sentences: There is upwelling of denser air from lower levels. This leads to a density anomaly which is observed by CHAMP. However, the question we are eager to answer is: What exactly causes the upwelling? Joule heating? Particle precipitation? Variations of the background density or the composition? Completely different processes? To tackle these questions we must not only consider the horizontal (CHAMP-observed) processes. An extension to the vertical distribution is required. Hence, apart from inclusion of model studies we run a combined CHAMP-EISCAT campaign to find support in ground-based Incoherent Scatter Radar (ISR) measurements. A periodicity analysis helps to clarify the influence of the solar wind and completes our investigations. These methods help to track the causes of the anomaly. They are addressed in Chapter 6 and 7.

Our results and findings are reviewed in Chapter 8. This leads to the conclusion which is judged to appear already here: We investigated an extremely fascinating but challenging field of research, where it is not unusual that answering one question instantly raises a new one (found at the end of Chapter 8). Though, is not this the appeal of research? A little word, four letters (and a little portion of motivation) suffice to pose a set of questions in the vast conglomeration of research topics.

Chapter 2

Thermosphere and ionosphere

This section outlines the area of interest, namely the upper atmosphere, the developments and the current status of the research field. In particular, during recent years the thermospheric research has obtained new impulses.

2.1 Thermosphere – ionosphere system

Based on the close relation between thermosphere and ionosphere in location, chemistry, dynamics, and electrodynamic properties, they are not meant to be treated as two separated systems but as one coupled thermosphere – ionosphere system in this study. The interaction within this region, especially the ionospheric effects on the thermosphere, are essential for the purpose of this work.

Altough the percentage of ionised gas in the upper atmosphere reaches only 0.1% at F2 peak altitude (Jee et al., 2008), its impact is exceedingly effective. It appears in both the momentum transfer processes by ion drag and as Joule heating in the energy balance (Zhu et al., 2005). Above the E region the ion gyrofrequency significantly exceeds the ion – neutral collision frequency. Therefore, the ions are forced to move along geomagnetic field lines. Instead of roaming freely with the streaming neutral particles, they exert a continuous drag on the neutral gas when it is moving across the geomagnetic field lines.
Conversely, in polar regions the ion drag can force neutral winds since strong plasma convection results in a continuous acceleration of the neutral air in the ion drift direction. Hence, the resulting wind circulation pattern (cf. Fig. 4.6) resembles to a certain degree the plasma convection pattern (Killeen et al., 1984). In addition, the plasma – neutral particle collision leads to neutral atmospheric heating (ion friction). This can be considered as the energy transfer from the magnetospheric electric field ($\vec{E'}$) to the ionospheric plasma motion followed by dissipation in the thermosphere due to collisions with neutral air particles:

$$q(h) \;=\; \vec{\jmath} \cdot \vec{E'} \;=\; \sigma_P E^2. \tag{2.1}$$

Here, $q(h)$ is the height-dependent heating rate per unit volume, $\vec{\jmath}$ is the current density, σ_P is the Pedersen conductivity, $\vec{E}$ is the externally applied electric field from the magnetosphere (E'), and from the neutral wind dynamo ($\vec{v} \times \vec{B}$): $\vec{E} = \vec{E}' + \vec{v} \times \vec{B}$. Basically, this process results in a temperature enhancement, which in turn causes variations in neutral winds, composition and - most important for this study - in the mass density distribution.
For the sake of completeness, some thermospheric impacts on the ionosphere should be mentioned: atmospheric heating and the corresponding expansion of the atmosphere are influencing the plasma density, especially during geomagnetic storms. During quiet days, they play a role for the sustainment of the nightside ionosphere or for the occurence of the so-called winter anomaly and semi-annual variation (Rishbeth et al., 2000, Zou et al., 2000).
Neutral winds generate electric fields by moving plasma across the geomagnetic field lines, thus varying ionospheric phenomena like the equatorial (EEJ) and polar (PEJ) electrojet or the equatorial ionisation anomaly (Lühr and Maus, 2006).

In this thesis, special emphasis is put on the high-latitude upper atmosphere.

2.2 High-latitude upper atmospheric research

People have always been fascinated by atmospheric phenomena. This fascination is not only restricted to near-ground phenomena like cloud formation, thunderstorms or wind vortices, but it extends to higher atmospheric layers, e.g. noctilucent clouds ($\approx$ 80 km above ground level) or auroras ($>$ 100 km altitude). Fascinating phenomena have been within the scope of (scientific) studies for a long time, and indeed, meteorology/aeronomy and geophysics rank among the earliest natural sciences. New instruments, measurement techniques and methods deliver "deeper and deeper" insights into the upper atmosphere. This permits the discovery of new phenomena on the one hand and to raise detailed questions on the other hand. Of course, this development includes any kind of research activity on the upper atmospheric polar cusp region.

2.2.1 Historical overview

The complex system of the thermosphere and the magnetosphere-thermosphere-ionosphere interactions have been studied since the beginning of spectroscopic measurements. The idea that the upper atmosphere is disturbed and heated by solar particles was first suggested in the 1930s (e.g. Appleton and Ingram, 1935). The existence of a cusp region was first mentioned in the work of Chapman and Ferraro in 1931. These authors report on a density depression in the solar wind which is caused by the Earth Magnetic Field (EMF). Heating, dissociation, and ionisation in the upper atmosphere were referred to solar ultra-violet (UV) radiation (Mitra, 1947). Solar UV radiation was the only energy input to the thermosphere that was considered in the early static diffusion models (Nicolet, 1960). The first empirical thermospheric models followed this concept. In the late 1950s, Jacchia first documented solar and geomagnetic energy effects from observations of Delta One 1958 and Beta Two 1958 satellites (Jacchia, 1959). In 1963, Jacchia and Slowey detected particle energy flow into the high-latitude thermosphere during geomagnetic storms. Besides the work of Jacchia (1961), Pätzold's model (Pätzold, 1963) is one of the first that contains a contribution to a density enhancement by geomagnetic heating. In 1964, a Kp- or Ap-dependent exospheric temperature contribution was included in the Jacchia model (Jacchia, 1964) and it was first reported on an anomalously large density increase in the polar region that was exceeding the expected effects at low latitudes by about 4 to 5 times (Jacchia and Slowey, 1964). Simultaneously, the first polar orbiting satellites in operation allowed inferring the density enhancements from orbital parameter analysis (Jacobs, 1967). First reports on particle fluxes in the cusp region date back to 1971: Heikkilä and Winningham (1971) refer to observations at low altitudes with the ISIS satellite, while Frank (1971) and Russell et al. (1971) accounted for high-altitude cusp observations with IMP-5 and OGO-5, respectively. They reported about direct observations of large fluxes of relatively low energy charged particles (~ 1 keV) which are precipitating continuously into the atmosphere through the magnetic field region at the magnetopause where the magnetic field lines diverge. With the help of Alouette and ISIS satellite data the influence of charged particle input during quiet times was studied and the average particle precipitation region could be localised (Olson, 1972). It was found to be best described in solar geomagnetic coordinates rather than in geographic coordinates. Based on data from Spades and Logacs satellites (Bruce, 1973, Moe et al., 1977), a global thermospheric density model was developed by Moe and Moe (1975). It takes account of the density bulge caused by energy deposition through the cusp. Between autumn 1981 and spring 1983, Dynamic Explorer DE-2 satellite data revealed an enhanced electron temperature in the dayside polar upper atmosphere. Its position is found to depend mainly on the level of geomagnetic activity (AE index) rather than on the B_z component of the interplanetary magnetic field, IMF (Prölss, 2006). The development of incoherent scatter radar techniques and their installation in auroral regions, such as EISCAT, revealed new possibilities for ground-based studies of the upper atmosphere, especially of the ionised component. Whilst this component has been subject of numerous scientific studies (e.g. Lathuillère and Brekke, 1985; Stubbe, 1996; Yordanova et al., 2007), due to a lack of suitable measurement methods, the investigation of the neutral component is gaining attention mainly in recent years (e.g. Bruinsma et al., 2004, Liu et al., 2005; Sutton et al., 2005; Lathuillère et al., 2008).

2.2.2 Present situation

The Earth observation satellite CHAMP contributes significantly to the investigations of the neutral component (Reigber et al., 2002). CHAMP is orbiting within this complex system of the upper atmosphere at ~ 400 km altitude. More details about CHAMP are presented in Chapter 4. The onboard high-sensitive tri-axial accelerometer allows for the first time continuous, physically clean and high resolution measurements of the neutral gas component with good global and spatial coverage for both the northern and the southern hemispheres (Bruinsma et al., 2004, Liu et al., 2005). From these data we can derive the total mass density as well as information about thermospheric neutral winds (H. Liu et al., 2006, Lühr et al., 2007). Liu et al. (2005) found that the air density at polar regions increases with increasing geomagnetic activity. The diurnal density variation dominates the total mass density distribution, but a cusp-related density enhancement is visible, even during geomagnetically quiet phases of 2002 (Liu et al., 2005). In a case study of 25 September 2000, Lühr et al. (2004) showed that the air drag measured along the CHAMP orbit sometimes contains superimposed small-scale features, which can reach almost a factor of 2 above the ambient drag under solar maximum conditions. These drag peaks occur during cusp crossings. A continuous occurrence was supposed.

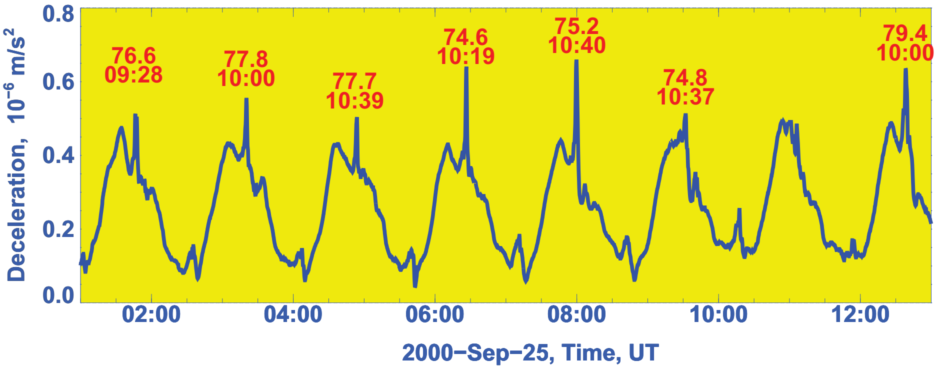

Figure 2.1: CHAMP deceleration due to air drag on 25 September 2000. Small-scale drag peaks occur during northern dayside cusp crossings. Adopted from Lühr et al. (2004).

Figure 2.1 displays the deceleration due to air drag which affected the satellite during several orbits on 25 September 2000. The harmonic large-scale structure represents the orbital variations, i.e. the deceleration which is typically experienced by the spacecraft along its orbital path. It is mainly caused by the orbital eccentricity. Somewhat more interesting for this work are the superimposed small-scale features, clearly visible in the northern auroral region. These drag peaks coincide - as marked by magnetic local time (MLT) and corrected geomagnetic (cgm) latitude in red - with cusp crossings.

As can be read in Section 2.3 the cusp is the region where magnetosheath plasma can enter lower altitudes most directly (Russell, 2000). According to Lühr et al. (2004), these incoming particles are supposed to be associated with field-aligned currents (FACs).

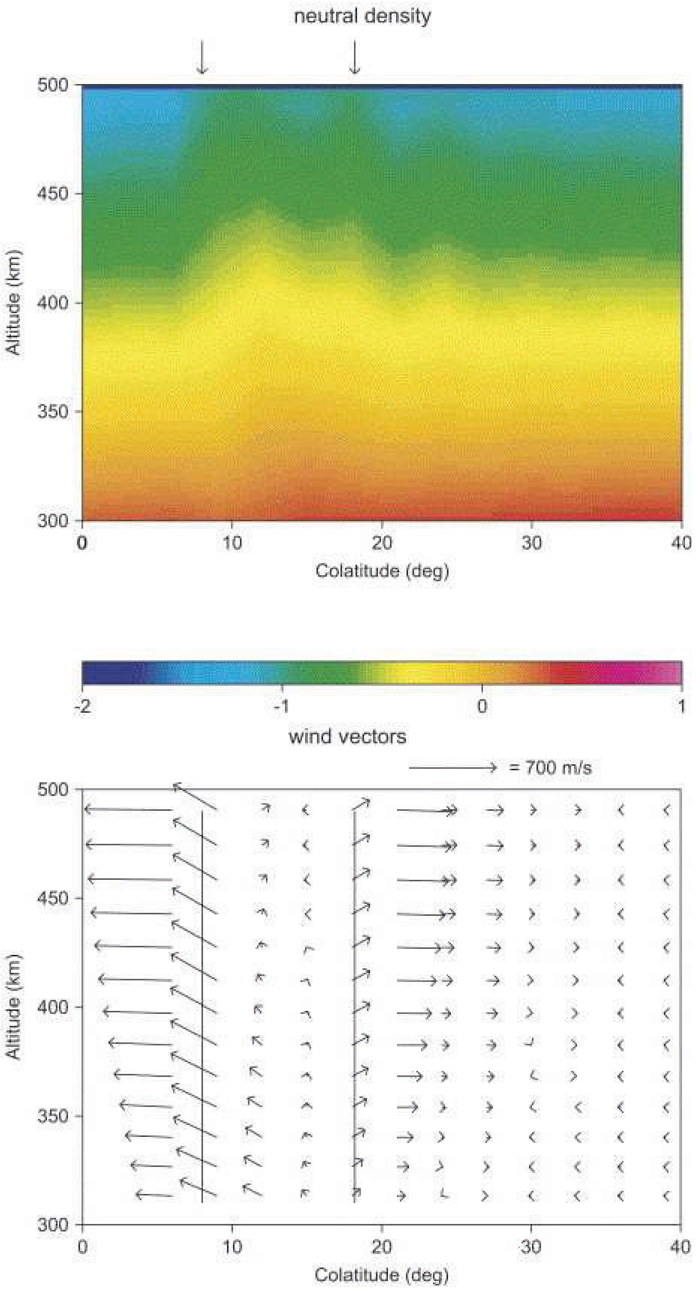

Figure 2.2: Neutral fountain effect as revealed by the model results of Demars and Schunk (2007). The upper panel dispalys the neutral density distribution in 10^{-11} kg/m^3 versus altitude, exhibiting a density enhancement in the heated region (between the arrows) in the upper atmosphere. The lower panel shows the corresponding wind pattern. Above the heated region the model simulates an upward motion of neutral air with divergence at the edges of the heated area. Both plots are adopted from Demars and Schunk (2007).

These currents may fuel local cusp heating, which can be responsible for air-upwelling, leading to density enhancements at higher altitudes. Lühr et al. (2004) suggested that in particular the simultaneously observed intense small-scale FACs may play an important role. They provide a strong coupling of the carried Alfvén waves with the high-latitude ionosphere, which means, magnetospheric energy is dissipated most efficiently in the atmosphere at ionospheric heights (Vogt, 2002).
Schlegel et al. (2005) were the first who combined CHAMP data with European Incoherent SCATter radar (EISCAT) measurements to investigate the density anomalies at cusp latitudes. During a seven-day campaign in February 2002, they frequently detected density maxima in the vicinity of the cusp with spatial scales of 100 km to 2000 km and with amplitudes of up to 50% above the ambient density. Only recently these local phenomena gained interest in the modeling community. Demars and Schunk (2007) succeeded in reproducing the CHAMP-observed density enhancements in the cusp with their high-resolution thermospheric model. According to their results, Joule heating in the cusp generates vertical transport which causes a neutral fountain effect. Hence, the neutral density is boosted up to higher altitudes and subsequently diverted into poleward and equatorward directions. In their model, Demars and Schunk (2007) had to gear up the heating in the E-layer by a factor of 110 to obtain a cusp density bulge as reported by Lühr et al. (2004). Figure 2.2 illustrates this effect. Above the heated region at cusp latitudes (i.e. between 8.7° and 18.1° colatitude in the plots) the vertical wind pattern reveals an upwelling of neutral particles which is accompanied by divergence at the poleward and equatorward edges of the heated region. The divergence occurs at all altitudes. It competes the general poleward wind velocity at the equatorward edge and adds to it at the poleward edge. The corresponding density, as presented in Fig. 2.2, clearly depicts an enhancement above the heated layer. It is considered to be a direct consequence of the air-upwelling.

The detailed reports on cusp air density enhancements are limited so far to event studies which may be regarded as a valuable tool for identifying relevant heating mechanisms. We extend the work of event studies by considering a larger number of cases. The identification of the role of the various possible contributors to the air density enhancement (like solar extreme ultra-violet (EUV) radiation, magnetic activity or atmospheric composition changes) requires a longer observational period. Analysing a multi-year period helps to reveal systematic features of the phenomenon, then identifying possible controlling parameters, and then searching for the causative mechanisms and processes.

2.3 The polar cusp

The polar cusp is defined as the location where the magnetic field lines from the magnetopause reach the ionosphere. Its location in the context of the terrestrial magnetosphere is illustrated in Fig. 2.3. According to Newell and Meng (1988) the cusp is the "dayside region in which the entry of magnetosheath plasma to low altitudes is most direct. Entry into a region is considered more direct if more

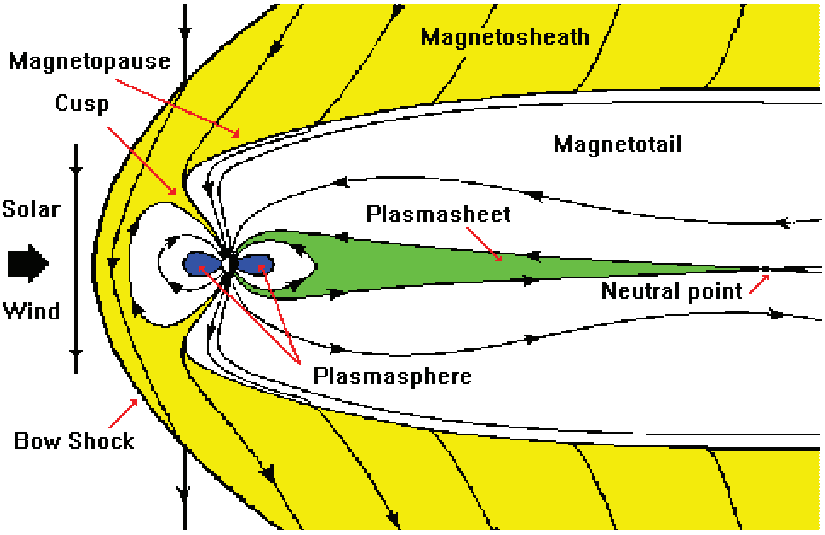

Figure 2.3: Schematic diagram of the cusp location in the terrestrial magnetosphere. Adapted from http://helios.gsf.nasa.gov/magneto.jpg.

particles make it in (the number of flux is higher) and if such particles maintain more of their original energy spectral characteristics". The cusp was first mentioned in Chapman and Ferraro (1931a,b). Fourty years later Heikkilä and Winningham (1971) and Frank (1971) reported on experimentally observed particle fluxes. Newell and Meng (1988) documented its occurence from DMSP measurements at about 800 km altitude between 11-13 MLT with a very confined latitudinal width of 0.8 - 1.1° cgm latitude, depending on the geomagnetic activity level. Russell (2000) finds the cusp to be located between 77° - 90° invariant latitude for an intermediate shape of the magnetopause; its position changes with varying magnetospheric plasma distribution, reconnection rate and reconnection location. Using realistic magnetospheric conditions by fitting the observed magnetic field yields a cusp position at 78° invariant latitude in the Tsyganenko model. According to Newell and Meng (1988) the most reliable way of identifying the cusp is based on the energy of the incoming particles ($E_e < 200\, eV$, $j_e > 6 \times 10^{14}\, eVm^{-2}\, s^{-1}\, sr^{-1}$, $E_i < 2700\, eV$, $j_i > 10^{14}\, eVm^{-2}\, s^{-1}\, sr^{-1}$). However, these authors divide the dayside auroral zone affected by soft precipitation into four regions (cusp, mantle, low latitude boundary layer (LLBL), and dayside extension of the boundary plasma sheet) out of which the cusp is the most poleward one (Newell et al., 1991).

Other researchers prefer to distinguish between cusp proper, cusp, mantle and cleft region (Kremser and Lundin, 1990), in which the cusp proper mostly corresponds to the above mentioned cusp definition of Newell and Meng (1991). In our study we will not limit our observations to the very confined area of the cusp proper but regard the neutral atmosphere in a wider catchment area around the cusp. Therefore, talking about cusp-related phenomena of the neutral thermosphere includes observation in surrounding areas. Indeed, a response of the thermospheric mass density to cusp-specific features, processes and characteristics does not remain restricted to the cusp location. The cusp can change its position from orbit to orbit. This behaviour depends on the variability of the IMF, the insulation, or the dipole tilt angle (Zhou et al., 1999).

Chapter 3

Aims of the thesis

Why is it important to improve our knowledge about the thermospheric density distribution and its variability?

First, the US Airforce monitors more than 14 000 objects in the Earth's environment, among them about 700 active spacecraft (e.g. ISS). Therefore, it becomes more and more important to precisely track their orbits and predict their ephemeris in order to prevent collisions and/or to allow the controlled re-entry into the atmosphere.
Second, it is indispensable to understand the physical processes related to solar perturbations, including their propagation through the interplanetary space and the Earth's environment down to the interaction with the atmosphere. The results might be incorporated in models which link variable solar conditions to the thermospheric density.

Thus, this study might not only be understood as a pure documentation of a magnetosphere-thermosphere-ionosphere phenomenon, but ideally serves as a basic proposal for continuing practice-related investigations. The Sections 3.1 – 3.2 refer to these aims in more detail.

3.1 Practical relevance of this study – space debris, a set of problems

The monitored artificial objects orbiting in the near-Earth environment can be added to 6% operating spacecraft, 13% intentionally disposed and separated objects, 17% upper stages of rockets and tanks, 25% inoperative satellites, and 39% satellite fragments (Flury (1994) and updates at NASA websites: http://www.nasa.gov).
Additionally, there are countless artificial objects of very small sizes which can neither be tracked by optical telescopes nor by radar.
In most cases, debris smaller than 1 cm does not cause damage due to robust wall constructions. Most problematic are particles of 1 – 10 cm size, since they can hardly be tracked but are heavy enough to cause serious damage.
Robust covering of spacecraft provides direct protection from space debris impacts.

This is, however, only sufficient for small and slow debris. It is avoided to put operating spacecraft into debris-crowded orbits. Early enough detected objects are compassed. For that purpose, various spacecraft carry special fuel reservoirs on board. Fuel is also needed to intentionally dispose satellites or to bring them to nonhazardous orbits.
Anyhow, large and heavy objects (more than 6 tons) might be a risk when not burned down completely at re-entry. The aeronomic forces cause them to break apart at altitudes of 70 – 80 km; solar panels are even destroyed at about 90 km altitude. To predict time and position of the re-entry as well as the impact area the knowledge of atmospheric conditions, particularly density and wind distribution is essential.

For effective manoeuvres it is of outstanding importance to be able to predict the path of both operating spacecraft and fragments as precisely as possible. In general, density and wind data derived from accelerometer readings contribute to the mitigation of this set of problems. In particular, CHAMP-STAR accelerometer measurements and the thereof derived density and wind distribution provide an excellent global overview over the atmospheric conditions in the densily spacecraft-populated 400 km niveau. Additionally, they allow for a diversification of local features with perceptible effects on a satellite orbit and fuel budget.

One of these local features is the cusp-related density anomaly. In this study, it is investigated and analysed for a statistically relevant time period. Therefore, it might help to pave the way to adjust the models and allow for efficient orbit determination and fuel calculation methods.

3.2 Motivation for studying the cusp-related thermospheric mass density anomaly

Up to now the thermospheric mass density distribution in the vicinity of the cusp was at best investigated in the frame of case studies (e.g. Lühr et al., 2004; SIRCUS campaign, Schlegel et al., 2005). The thereof obtained results raised some questions which have not been answered sufficiently yet:

1. Is the density anomaly in the cusp region a continuous phenomenon?
2. What magnitude and scale size does the density anomaly reveal?
3. Is the cusp-related density anomaly observed in both hemispheres? If so, does it show systematic differences?
4. Does the anomaly show dependences on certain parameters/atmospheric conditions?
5. Why is the density anomaly not reproduced (sufficiently) in most of high-latitude/upper atmosphere models?
6. What causes, releases, excites the cusp-related density anomaly? Which causes can come into question? What are the roles of Joule heating, composition

changes, particle precipitation? Are there other processes/mechanisms that have to be taken into account?

CHAMP observations provide an excellent potential to scan a longer time period and compile a statistically meaningful, climatological description. The data are used as the basis for answering the above questions.

Chapter 4

CHAMP mission

The following lines briefly outline some facts about the CHAMP satellite and the onboard STAR accelerometer. The subsequent information has been adopted from the work of Reigber et al. (2002), Rentz (2005), and the reports accumulated in the books about the CHAMP mission (Reigber et al., 2003; Reigber et al., 2005).

4.1 CHAMP CHAllenging Minisatellite Payload

The CHAMP mission was designed to create a link between ground-based observations (precise, but restricted to a confined part of the atmosphere and to a short time interval) and classical satellite observations (monitoring of large-scale phenomena, short-sequence snapshots, but a limited resolution due to the orbital altitude). Therefore, it allows deep insight into various phenomena, out of which we would like to focus on the thermospheric density at cusp latitudes.

4.2 The satellite

Launched on 15 July 2000 the spacecraft has a multi-instrument payload. Its design parameters and key data are compiled in Table 4.1; an illustration of the satellite's design can be found in Fig. 4.1.

CHAMP moves along a quasi-polar, quasi-circular orbit, meant to cover preferably every point on Earth at regular intervals in order to provide a global, homogeneous, continuous dataset. Due to the orbital precession, it takes about 11 days to pass one hour of local time. Hence, CHAMP covers all local times once in about 131 days (considering data from both ascending and descending branch of the orbit).

Among the payload are the star sensors, the GPS receiver and the Fluxgate magnetometer which provide a precise attitude and position control. The Fluxgate magnetometer at the satellite boom additionally measures the ambient magnetic field at high sampling rate and precision for all three components. The Overhauser magnetometer at the tip of the boom provides absolute magnetic field readings,

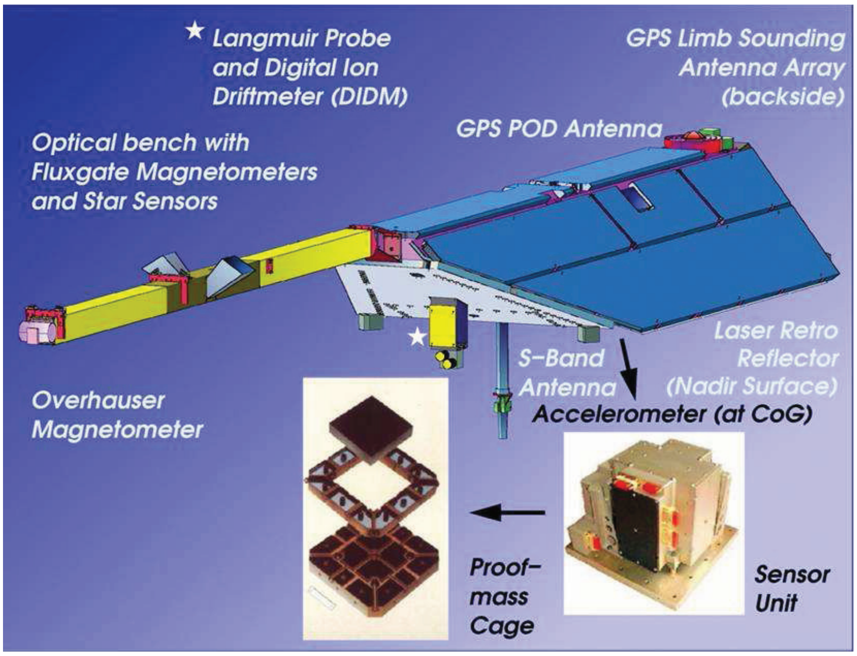

Figure 4.1: Illustration of the CHAMP satellite (front view) and its payload. By courtesy of Dr. Martin Rother, Dr. Ludwig Grunwaldt, Dr. Matthias Förster, 2005.

namely the scalar field magnetic field strength. The GPS Blackjack receiver serves for receiving GPS signals for the determination of the position and time, for data communication and for navigation. The Laser-Retro-Reflector at the Nadir surface allows for high-precision distance measurements, and the GPS Limb Sounding antenna array enables Radio Occultation measurements with a sampling rate of 50 records per second. Thus, the GPS instruments allow to derive stratospheric temperature profiles and tropospheric water vapor profiles. The front side of CHAMP is equipped with the Digital Ion Driftmeter (DIDM) and the Langmuir probe. They provide ion drift velocity, electron density and electron temperature along the orbit. The most important instrument concerning this study is the STAR accelerometer. An instrument of comparable design and sensitivity has never been in operation before in such low orbits. It is described in Section 4.3.

4.3 The accelerometer

Our special interest concerns the onboard sensitive accelerometer. It was constructed by the French Space Agency, ONERA, and provided by the French Centre for Space Sciences, CNES.
It is an electrostatic accelerometer measuring the non-gravitational accelerations acting on the spacecraft body. Therefore, a proof mass of about 100 g is placed inside an electrode cage exactly in the satellite's centre of gravity. Thus, it is kept acceleration-free as long as no non-gravitational forces act on the satellite. In case of

parameter	
length	8333 mm (with 4044 mm boom)
height	750 mm
width	1621 mm
total mass at launch	522.5 kg
orbital altitude after launch	456 km
area-mass ratio in ram direction	0.00138 m^2/kg
inclination	87.25°
orbit period	93 min

Table 4.1: CHAMP key parameters.

such an acceleration the proof mass is deflected from its rest position. Its surface and the electrodes at the cage walls form a capacitor, i.e. the impact of non-gravitational forces can be read from variations of the capacity. All cage walls are equipped with electrodes. Hence, the capacity changes and therefrom derived accelerations can be precisely derived for all three spatial directions. The two horizontal components have a resolution of $3 \times 10^{-9}\, m/s^2$. Consequently, a resolution of more than $1 \times 10^{-14}\, kg/m^{-3}$ is obtained for the thermospheric mass density (cf. Section 4.4). The vertical component is less sensitive ($3 \times 10^{-8}\, m/s^2$), but due to a malfunction the readings are not reliable. This does not affect our study as outlined in Section 4.4.1. Due to the satellite's very low eccentricity it is possible to employ accelerometer readings equally well from the whole orbit, not only from the perigee or apogee height.

4.4 Thermospheric mass density as derived from CHAMP

The accelerometer readings are used to obtain the thermospheric mass density as presented in the following.

4.4.1 Estimation of thermospheric mass density

To estimate the thermospheric mass density in the environment of the CHAMP satellite we make use of the following assumption: The denser the air, the larger the air drag, and the stronger the spacecraft's deceleration. Like most of the aeronomic problems this relationship is nonlinear. When crossing a considered air volume, the satellite's cross sectional area, A_{eff}, experiences the pressure norm $p = m \cdot a/A_{eff}$, which practically amounts to the dynamic ram pressure, $p = \frac{1}{2}\rho C_D v^2$. Here, $m \cdot a$ is the amount of Newtonian friction, which generally occurs at high velocities: the moving spacecraft body thrusts aside the gas volume in front of it (Rentz, 2005). We obtain for the density, ρ:

$$\rho = \frac{2ma}{C_D v^2 A_{eff}} = \frac{2ma}{C_D v^2 \left(A_x \, cos\alpha + A_y \, sin\,|\alpha|\right)}, \tag{4.1}$$

where m is the mass of the satellite, $a = |\vec{a}| = \sqrt{a_x^2 + a_y^2}$ is the norm of the satellite's acceleration (the vertical acceleration is negligible compared to the acceleration in the horizontal plane). The vertical component can be neglected since the deviation angle in z-direction (pitch rotation around the y-axis) is very small (root mean squares values of less than 0.5°) due to usually small vertical winds. According to Smith (1998) they amount to 0.01 – 0.04 km/s, i.e. they are very small compared to the flight velocity of 7.6 km/s and the corotational impact of at the most 0.492 km/s in cross-track direction. C_D is the drag coefficient, and v is the spacecraft's velocity with respect to the air at rest. The effective cross-sectional area, A_{eff}, can be composed of the surface elements, $A_x \, cos\alpha$ and $A_y \, sin\,|\alpha|$, with A_x (A_y) being the satellite's surface in x- (y-) direction, and α being the angle between CHAMP's longitudinal axis and the ram direction.

Due to the circular orbit and the weak vertical wind the vertical component of the spacecraft's velocity is neglected, yielding:

$$v^2 = v_x^2 + v_y^2. \tag{4.2}$$

A scale analysis justifies this assumption: According to Liu et al. (2005) vertical winds with speeds of only 10-40 m/s are acting on the satellite body. Such speeds are very small compared to the flight velocity (7.6 km/s) and the cross-track wind component of the order of the corotational wind ($\approx$ 492 m/s at the equator).

Since the velocity components cannot be measured directly, we assume for deriving v^2:

1. The component in x-direction, v_x, is described by the flight velocity, thus yielding $v_x = 7600$ m/s.
2. The acceleration vector and the velocity vector are aligned. We can therefore equate the ratios of the components: $v_y = v_x \frac{a_y}{a_x}$. This allows to derive the cross-track wind velocity.
3. From 1. and 2. and the geometric relations it follows: $tan\alpha = a_y/a_x$, which is used to calculate the effective cross-sectional area.

For some interpretations the density measurements have been normalised to a common altitude. Our study concerns CHAMP measurements in the altitude range of 356 – 426 km. Special emphasis is put on the year 2003 (418 – 396 km). Therefore, the common height is chosen to be 400 km. The density data are height-corrected via the relation:

$$\rho_{400} \; = \; \rho(h) \frac{\rho_{MSIS}(400km)}{\rho_{MSIS}(h)}, \tag{4.3}$$

where h is the actual height of CHAMP above the ellipsoid. The model density, ρ_{MSIS}, is taken from the NRLMSISE-00 atmospheric model (Picone et al., 2002; cf. Appendix C.1).

4.4.2 Corrections and biases, errors and uncertainties

It is necessary to apply some corrections and remove some biases before the estimation of density values:

The accelerometer provides originally Level 1 data (1 Hz sampling rate). They have to be pre-processed in order to correct or remove disturbed readings before deriving the density. Most of the fake accelerations are due to attitude manoeuvres, activation/deactivation of the heaters or system reboots (Förste and Choi, 2005), but some of them remain unexplained. We use Level 2 data (0.1 Hz sampling rate) which are free from spurious accelerations. The 10 second sampling corresponds to a spatial resolution of ∼76 km or 2/3° in latitude. Due to the instrument's resolution we have to accept an uncertainty in the density readings of $6 \times 10^{-14}\, kg/m^3$.

The acceleration which is acting on the proof mass inside the accelerometer is composed of several contributions, namely the acceleration on the spacecraft's surface, the acceleration due to attitude control manoeuvres, the acceleration due to the offset between proof mass and spacecraft's centre of gravity, and the acceleration due to the Lorentz force (Bruinsma et al., 2004). Our special interest concerns the acceleration acting on the satellite body's surface, in particular the portion due to air drag. All of the other components have been removed or are negligible: Apart from the acceleration due to air drag the surface experiences an acceleration which is caused by solar radiation pressure and infrared radiation pressure from the Earth's surface. These contributions have been removed, just like the acceleration due to attitude control manoeuvres. The offset between the proof mass and the centre of gravity does not exceed 2 mm. Hence, the corresponding acceleration component is negligible. Likewise negligible is the acceleration due to the Lorentz force which might act on a charged proof mass. Since the STAR proof mass is shielded by the metallic electrode cage, the Lorentz force, $q(\vec{v} \times \vec{B})$, has no effect.

An important contribution to the observed deceleration comes from the thermospheric winds. As already mentioned in the assumptions in Section 4.4.1 we neglect the effect of head and tail winds. They are generally small at low and middle latitudes where the meridional wind component is of the order 100 m/s, but they can exceed 10% of the flight velocity in polar areas. This can cause an error of more than 20% in the density estimates, thus being the largest contribution to the error budget.

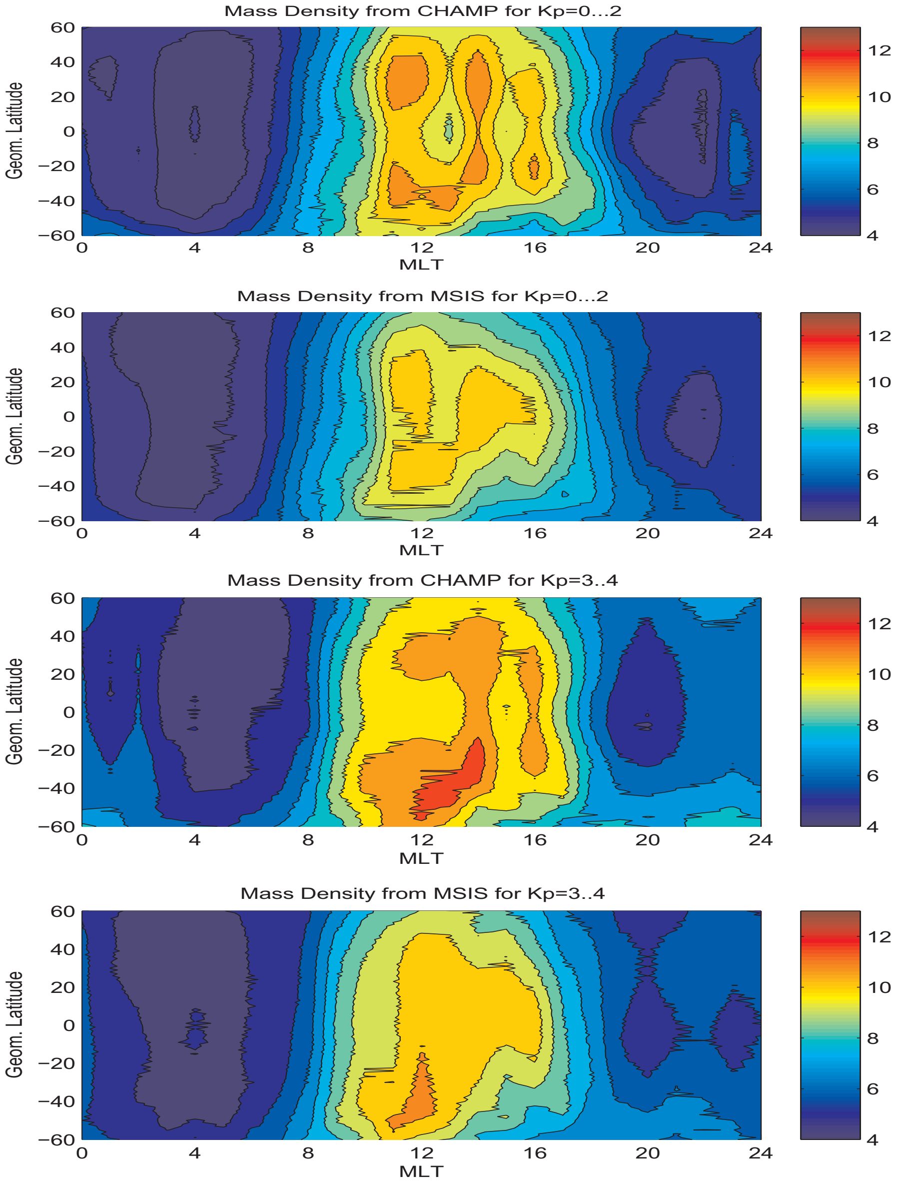

Figure 4.2: 2002 thermospheric mass density from CHAMP (first and third panel) and MSIS (second and fourth panel) for geomagnetically quiet (first and second panel) and moderately disturbed (third and fourth panel) conditions. The Figures are adopted from Liu et al. (2005).

In Section 4.5 we will address the properties of high-latitude winds in more detail. Nonetheless, for the statistical analysis we can assume that head and tail winds average out over the long observation period. Apart from that there has never been observed a systematic deviation due to a continuous head or tail wind in CHAMP measurements. Smaller contributions come from the instrument's precision (20 m/s) and other systematic errors (15 m/s) as outlined by H. Liu et al. (2006).

4.4.3 General aspects of the thermospheric mass density

Liu et al. (2005) investigated the CHAMP-observed thermospheric mass density on a global scale. The authors used 2002 data, separated them for quiet ($Kp = 0...2$) and moderate ($Kp = 3...4$) geophysical conditions, sorted them into a geomagnetic coordinate system, and normed them to a common altitude of 400 km (to exclude vertical density variations as observed due to the satellite decay).

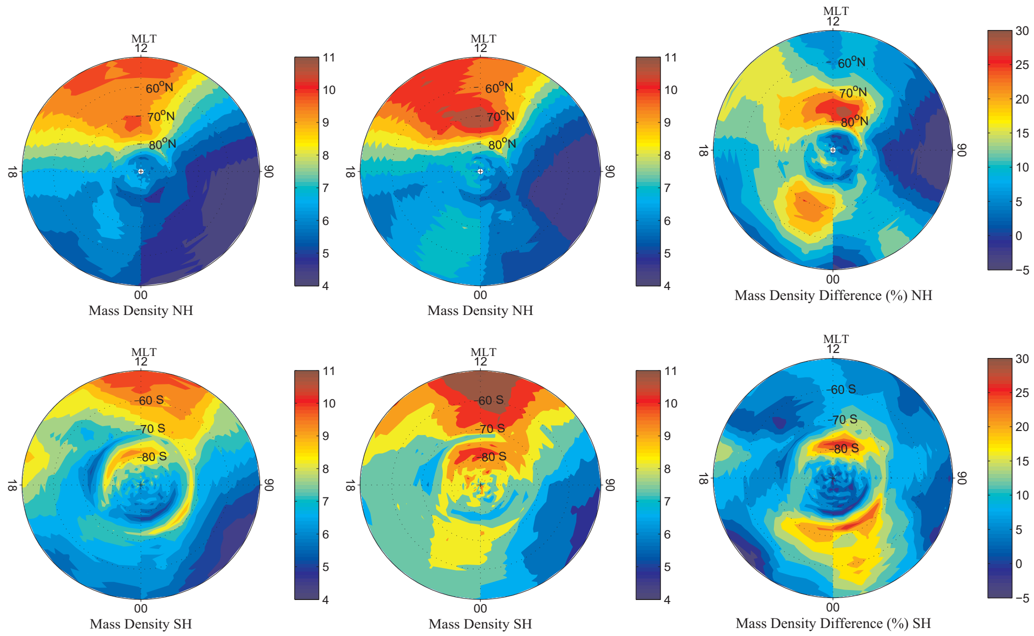

Figure 4.3: 2002 polar thermospheric density distribution as derived from CHAMP for geomagnetically quiet conditions (first column) and moderately disturbed conditions (second column), and the percentual mass density difference between CHAMP and MSIS estimates (third column) for the northern (upper row) and southern (lower row) hemispheric conditions. The Figures are adopted from Liu et al. (2005).

The results are presented in Fig. 4.2. It displays the thermospheric total mass density, as derived from CHAMP (Fig. 4.2, first and third panel) and from the atmospheric model MSIS (Fig. 4.2, second and fourth panel) in a Magnetic Local Time

(MLT) versus 60° to -60° magnetic latitude frame. For both quiet (Fig. 4.2, first and second panel) and moderate (Fig. 4.2, third and fourth panel) conditions the CHAMP data roughly correspond to the model simulations, but the Figure reveals an increasing density magnitude with increasing geomagnetic activity in the data and in the model.

Analogue to the diurnal variation in the troposphere the thermospheric density is characterised by a minimum in the early morning ($\approx$ 0400 MLT) and a maximum in the early afternoon ($\approx$ 1400 MLT). The density maximum drags behind the solar radiation-induced temperature maximum by about two hours due to the atmosphere's inertia, as described by Maruyama et al. (2003). A correlation analysis between F10.7 as an index for the solar EUV radiation and the CHAMP-observed density reveals a significant dependence on the strength of the solar activity. The correlation is found to be higher at low latitudes than at high latitudes, and higher on the dayside than on the nightside. This is expected in view of the typical insulation conditions (c.f. Section 5.4).

A prominent feature in the CHAMP data is the dayside double maximum: Between about 1000 – 2000 MLT the density maxima can be found $\approx$ 20° northward and southward of the equator, separated by a trough in the equatorial region. As revealed in Liu et al. (2007), Fig. 4, the trough follows the geomagnetic equator during equinoxes. This distribution resembles the low latitude electron density, which also shows an equatorial anomaly with a trough near the equator and maxima about 15° northward and southward of it. Liu et al. (2005) regard this as an indicator for the strong neutral-plasma coupling in this region.

The model MSIS, however, does not reproduce the double maxima. Consequently, the CHAMP densities can overestimate the MSIS densities by about 20% in the area of density crests. At other latiudes the MSIS values are overestimated by about 5%.

Figure 4.3 depicts the thermospheric density distribution at high latitudes. The top (bottom) row displays for northern (southern) latitudes above $|50°|$ magnetic latitude the density for quiet ($Kp = 0...2$) geomagnetic conditions in the first column, for moderately disturbed geomagnetic conditions ($Kp = 3...4$) in the second column, and the mass density difference between CHAMP observations and MSIS results in the third column.

Under quiet conditions, the typical diurnal variation (as already detected at low and middle latitudes) can be seen. A slight enhancement at cusp latitudes is seen, especially in the northern hemisphere. The density pattern becomes disturbed under elevated geomagnetic activity: the area of large densities is extended. In the southern hemisphere, it can reach the polar cap or even cross it to form a zone of enhanced density values in the pre-midnight sector.

Again, the results of MSIS and CHAMP roughly agree. However, MSIS does not depict distinct features like the enhanced density values at cusp latitudes or in the pre-midnight sector. Here, the CHAMP densities can exceed the MSIS predictions by up to 30%. This can be easily seen in the third column of Fig. 4.3. However, averaging over all latitudes results in a percentage difference of 5.9% log_e (CHAMP/MSIS90) for quiet and 8.0% log_e (CHAMP/MSIS90) for moderately disturbed conditions in the dataset of Liu et al. (2005). These authors suggest Joule heating as an explanation for the enhancement at cusp latitudes, which occurs under the influence of intense small-scale field aligned currents (FACs), as supposed by Lühr et al. (2004) and FACs confined to the cusp (at least under quiet conditions) as found by Neubert and Christiansen (2003).

4.5 The average wind distribution in the polar upper atmosphere

The different influences on the polar upper atmosphere do not only impact the neutral mass density but also the neutral wind. In fact, the neutral wind and the neutral density are affecting each other. The wind provides the pressure compensation between areas of different mass density. In addition, plasma convection, Coriolis force, and centrifugal force are affecting the net motion of air parcels.
Indeed, scanning the globe for maximal wind speeds leads to the polar regions. Dependent on geomagnetic activity, wind speeds of up to 200 m/s at solar minimum and 800 m/s at solar maximum have been observed with Fabry-Pérot interferometer (FPI) measurements (Killeen et al., 1995). In anticipation of our dataset CHAMP measurements generally reveal maximal wind speeds of 800 m/s. In extreme cases, however, speeds of more than 1000 m/s can be found, which have not been classified unreliable in the pre-processing.
Roble et al. (1984), Thayer et al. (1987), Killeen and Roble (1988) interpreted DE-2 observations and concluded that the thermospheric winds are driven mainly by ion – neutral coupling processes. McCormac and Smith (1984), however, analysed FPI measurements to find a significantly lower dependence of the neutral winds on the ion drift velocity. A description of density and wind derivation from CHAMP accelerometer readings is given in the Appendix A. Although the accelerometer measurements onboard CHAMP allow only for the estimation of one velocity component in the x-y-plane it is possible to retrieve the average horizontal 2D-wind fields for the polar regions.

4.5.1 The derivation of 2D-wind estimates

To derive a polar wind pattern a statistical approach was attempted which is described in the following, and the binning concept is illustrated in Fig. 4.4. It has been published in Lühr et al. (2007).

The polar region between |55°| and |89°| cgm latitude is divided into 918 quasi equal-area bins of about 222 × 232 km each. Therefore, first of all, 17 rings with a width of 2° latitude each are colocated concentrically around the cgm poles. Consequently, the innermost ring (ring 1) ranges from |89°| to |87°| cgm latitude, ring 2 from |87°| to |85°| ... and the outermost ring (ring 17) from |57°| to |55°| cgm latitude. Every ring is subdivided in $m * 6$ bins, where m is the ring number (increasing with increasing distance from the pole). Then, all CHAMP overpasses over the polar region are considered. For the generation of Figs. 4.5 – 4.6 all available overpasses out of 131 days symmetrically distributed around June solstice 2003 (i.e. 2053 overpasses per hemisphere) are analysed. During this time interval, CHAMP traverses all local times once. The arrangement symmetrically around June solstice allows the simultaneous view on summer and winter polar areas. Due to this binning procedure 100–600 observations can be counted per bin. It happens that up to three consecutive measurements are dropped into the same bin. The number of records per bin allows statistically relevant results. It exceeds 100 below |70°| cgm latitude and increases with decreasing distance from the pole.

The satellite crosses the polar region at a certain angle α with respect to the noon/midnight meridian (cf. Fig. 4.4). During an overpass over a bin this angle α and the observed cross-track wind velocity component are dropped into the bin. Finally, all values in a bin are averaged and the velocity components, u_x and u_y are returned in Cartesian solar-magnetic (SM) coordinates. Here, the x-axis points sunward, parallel to the magnetic noon meridian, the y-axis points dawnward, and the z-axis points from the geomagnetic North pole towards the Earth's centre. As mentioned in Lühr et al. (2007) the winds are retrieved applying the least-squares error minimisation (LSEM) procedure, which is a modification of the method described in the Appendix of Codrescu et al. (2000). A detailed description of the LSEM procedure can be found in the Appendix B.

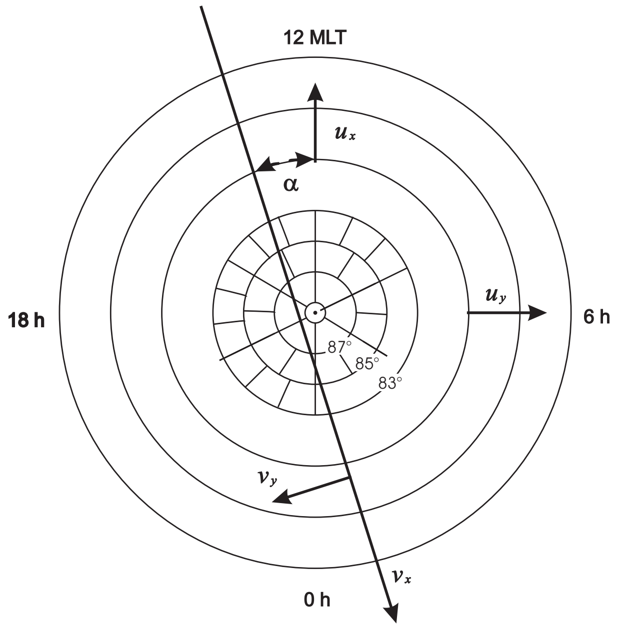

Figure 4.4: Illustration of the binning concept which is applied to derive 2D-wind vector estimates. The centre of the dial plot marks the geomagnetic pole, the polar region is divided into quasi equal-area bins. The long arrow symbolises a CHAMP overpass. Adopted from Lühr et al. (2007).

The cross-track wind speed, u_{cross}, is deduced from the acceleration ratio a_y/a_x and the flight velocity, v_x:

$$u_{cross} \;=\; \frac{a_y}{a_x} v_x - v_c. \tag{4.4}$$

Since the situation is considered from an Earth-fixed frame, the wind velocity due to corotation, $v_{c\phi} \;=\; 492\, cos(latitude)$ m/s, is subtracted.

For the LSEM procedure, each bin is scanned for the direction and magnitude of the vector which best supports all individual cross-track measurements. By assuming that all observed cross-track winds are related to a mean wind with a speed v blowing in the direction γ we can compute an error function, FE:

$$FE(v, \gamma) \;=\; \sum_{i=1}^{n} \left(u_{cross_i} - v sin\left(\gamma - \alpha_i\right)\right)^2, \tag{4.5}$$

where n is the number of samples in a bin. The α_i give the observation directions. According to Coderescu et al. (2000) the optimal wind direction, γ_m, can be found by searching the value of γ in Eq. (4.5) through all directions and identifying the minimum of FE.
The mean wind speed can then be computed:

$$v \;=\; -\frac{\sum_{i=1}^{n} u_{cross_i} sin\left(\gamma_m - \alpha_i\right)}{\sum_{i=1}^{n} sin^2\left(\gamma_m - \alpha_i\right)}. \tag{4.6}$$

In practice, the determination of the optimal wind direction, γ_m, was not always a straightforward task in this study, since the minima of FE are in some cases very shallow. In those cases the maxima of FE are, however, well developed. The maximum of FE is expected to be achieved at an angle γ, which is 90° away from γ_m. It turned out that most consistent wind distributions are obtained by using a suitably weighted average of the two angles derived from the minima and maxima of the error function.

4.5.2 Polar thermospheric neutral wind pattern

Figure 4.5 displays the distribution of the averaged thermospheric wind velocities for the northern hemisphere (left panel) and southern hemisphere (right panel) for 2003 June solstice conditions.

The result of Lühr et al. (2007) is presented here to provide insight in the high-latitude thermospheric wind distribution. The authors used CHAMP data of 131 days around June Solstice, thus displaying the northern hemisphere as the summer pole and the southern hemisphere as the winter pole.
Figure 4.5 shows the thermospheric wind speeds as derived with the explained binning approach for 2003 June Solstice conditions in a geomagnetic coordinate system.

The colour-coded wind speed is given in m/s. In the northern hemisphere, the wind speed is fairly low (≈ 100 m/s) in subpolar latitudes in the noon and afternoon sectors. In the polar cap and at auroral latitudes in the morning sector, however, large wind speeds of more than 600 m/s can be found. The southern hemispheric distribution is qualitatively comparable to the northern one with two exceptions: First, the northern features are more distinct since the wind speeds are generally larger than the southern ones. For instance, the reduction of the day-to-night velocity over the polar cap is by about 35% reduced in the southern hemisphere. Second, the southern pre-midnight sector is characterised by larger wind speeds than the same region at northern latitudes. Further insight is provided by the vector plots of Fig. 4.6. They present the mean thermospheric wind vector pattern in the same format as Fig. 4.5.

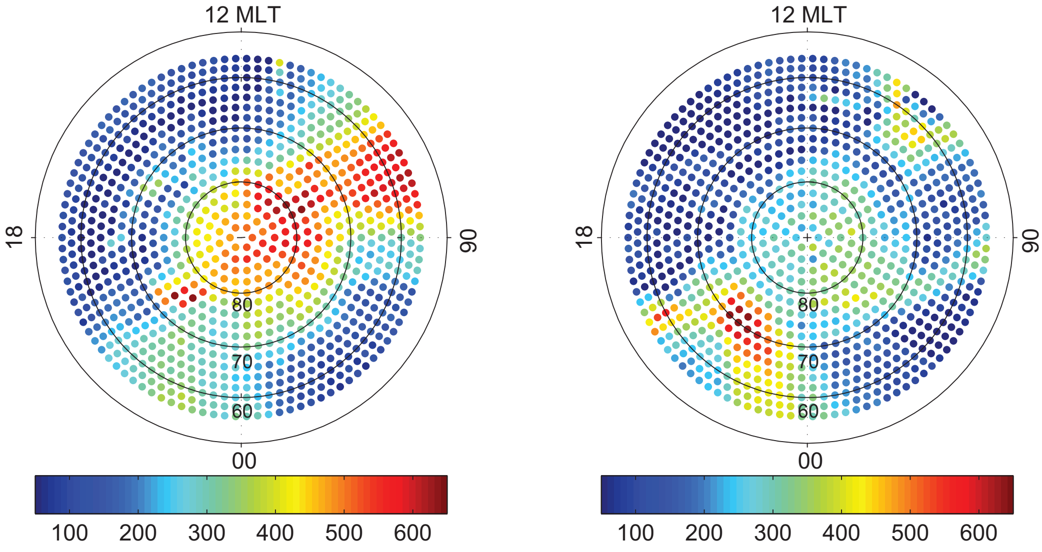

Figure 4.5: Distribution of wind speeds in m/s at polar cgm latitudes. The northern (southern) hemispheric dial plots depict the summer (winter) hemispheres. In both hemispheres, highest wind speeds occur in the morning sector and in the evening sector. Adopted from Lühr et al. (2007).

According to Fig. 4.5, longest arrows can be found in the northern polar cap. They have an antisunward direction. This can be explained by the alignment of the neutral pressure gradient force and plasma drift in that area. Both forces are expected to control the neutral wind.

In the midnight sector westward zonal winds are dominating. In the early morning low wind speeds primarily in zonal directions are observed at subpolar latitudes. On the dawn side, we find zonal dayside-to-nightside winds with larger velocities. At noon-to-dusk auroral latitudes a wind stagnation zone can be retrieved aligned with the auroral oval. Poleward of this zone the pattern displays an anticyclonic vortex with a focal point near 70° magnetic latitude and 1830 MLT. These features

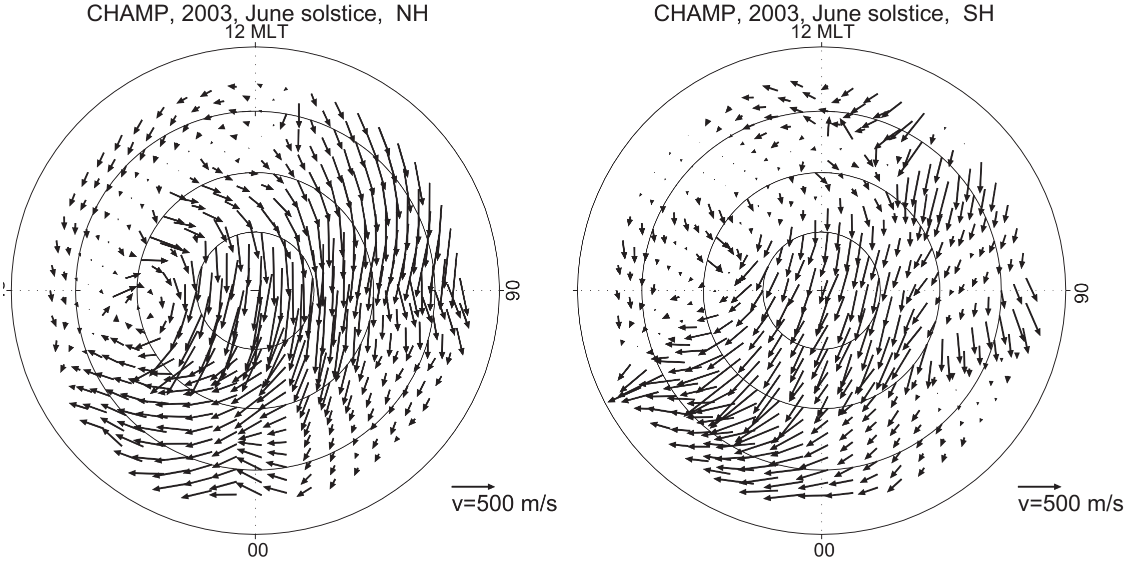

Figure 4.6: Horizontal wind vectors in the northern hemisphere (left) and southern hemisphere (right) polar regions, as derived via the LSEM method. The format and the time period is the same as in Fig. 4.5. Highest wind velocities occur in the antisunward flow over the polar caps. Near the cusp hardly any horizontal wind speed can be observed. Adopted from Lühr et al. (2007).

can be explained by the impact of Coriolis force and plasma drift: The plasma drift is generally sunward in the auroral dawn and dusk sectors. Hence, it competes with the neutral aerodynamic forces. The velocities in the dawn sector are enhanced by the support of the Coriolis force. Its direction also forces the vortex generation in the dusk sector. Its radius is consequently controlled by the initial wind speed and the focal point's distance to the pole.

Demars and Schunk (2007) offered an explanation for the wind stagnation in the cusp region: Their model simulations predict upward winds in the cusp, accompanied by divergence in all directions. In a snapshot of the horizontal x-y-plane this would lead to a stagnation point with surrounding wind vectors pointing away from the stagnation in all directions. This feature can be identified in Fig. 4.6.

The other part of the stagnation zone can be explained by the competing influence of sunward plasma drift in that area.

The southern hemispheric velocities amount to about 2/3 of the northern one, but the pattern remains fairly the same. However, the distribution is less well-ordered, possibly due to the larger offset between the southern hemispheric geographic and geomagnetic poles, and due to the seasonal differences between summer and winter hemispheres.

From Fig. 4.7 we can gain information about the variability of the prevailing wind. It displays the relative standard deviation. We find small relative uncertainties

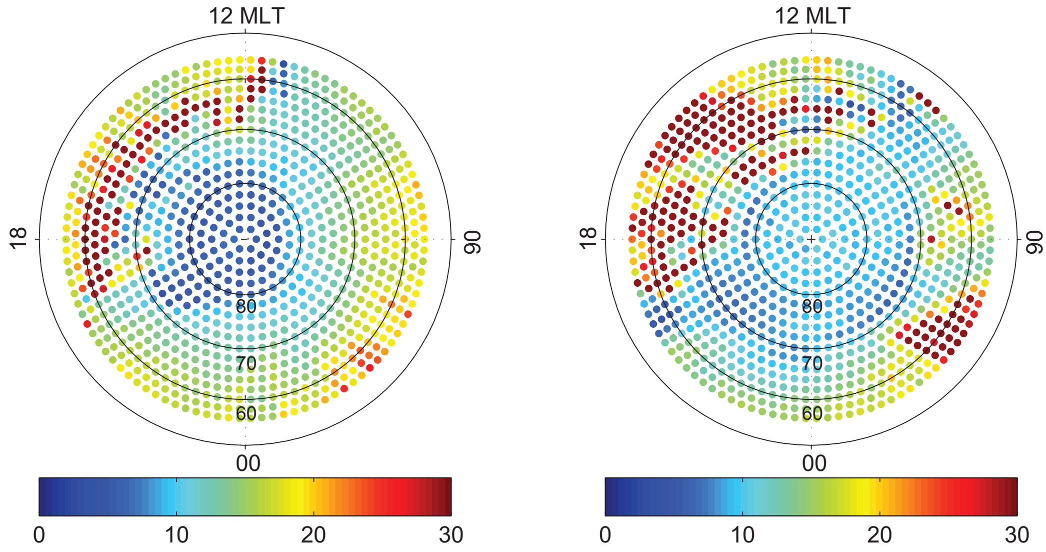

Figure 4.7: Relative standard deviation of wind speeds in %, as derived via the LSEM method. The format is the same as in Fig. 4.5. The standard deviation increases towards the fringes of the plot. Adopted from Lühr et al. (2007).

(<10%) in the polar cap and in most of the auroral oval. Towards the equatorward edges (where the number of records per bin decreases) the uncertainty amounts to about 20%. In areas with very low wind speeds it can reach up to 30%. Apart from this, the absolute uncertainty of the wind speed amounts to 50 m/s in all cases.

Another aspect of the high-latitude wind was investigated by Förster et al. (2008). The authors found that:

- For IMF B_y positive (northern hemisphere) and IMF B_y negative (southern hemisphere) a large-scale clockwise wind vortex is observed in the evening sector. It is colocated with the plasma convection dusk cell.
- The neutral wind speed is influenced by the magnetospheric ion drift, which in turn depends on the solar wind conditions. Hence, maximal northern hemispheric wind speeds occur for IMF B_y negative, IMF B_z negative conditions. Asymmetrically, they are observed for IMF B_y positive, IMF B_z negative in the southern hemisphere. In general, maximal wind speeds occur in the polar caps.
- In the morning sector, the Coriolis force and the centrifugal force balance each other and a disturbed wind pattern at about 70° cgm latitude is obtained.
- While the plasma convection pattern shows a vortex in the polar cap the neutral wind flow crosses the polar cap almost laminary.

- The southern hemispheric wind pattern is much more disturbed (ca. 25% larger standard deviations) than the northern hemispheric one. This might be due to the larger offset between the geographic and geomagnetic poles. Such a difference in the standard deviation might be reflected in larger differences in the heating rates of the two hemispheres.

The results give reason to a continuative investigation of a longer time period in order to study behaviour and variations of the polar thermospheric dynamics.

Chapter 5

Climatology of the cusp-related thermospheric mass density anomaly

CHAMP ranks among the few minisatellites (launched in recent years) which offer a precise coverage of northern and southern hemispheric polar regions. Prompted by Fig. 2.1 we investigated the thermospheric mass density characteristics in the vicinity of the dayside cusp region over a four-year interval.

5.1 Choice of coordinate systems

The polar thermosphere experiences the influence of different forces of both electrodynamic and aerodynamic nature. For an adequate treatment of associated effects a suitable coordinate system should be chosen. The Coriolis force for example depends on the geographic latitude. The effect of the pressure gradient force is best investigated in a geographic – solar local time frame; plasma drift and ion drag are best described in MLT and geomagnetic coordinates. Here, we intend to find the most suitable coordinate system to display the upper atmospheric density in the polar (cusp) regions.

	median density (10^{-12} kg/m^3) (height-normalised to 400 km)	cgm latitude	MLT
NH	5.69 ± 1.14	56° ± 1°	1338 ± 7.0 min
SH	5.96 ± 1.19	-58° ± 1°	1200 ± 7.5 min

Table 5.1: Characteristic parameters for density maxima in the polar regions in 2003.

For 2003, the density distribution in geomagnetic and geographic coordinates is faced in Figs. 5.1 and 5.2, respectively.

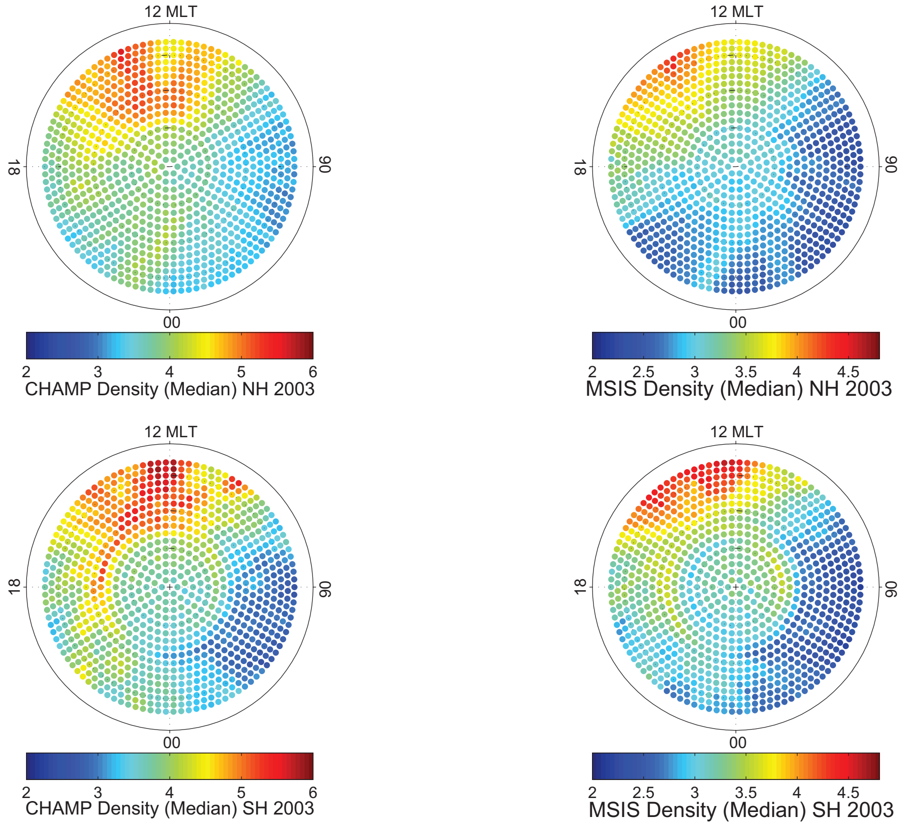

Figure 5.1: Annual average of the thermospheric neutral mass density in the polar regions of the northern (NH) and southern (SH) hemispheres in 10^{-12} kg/m^3, as derived from CHAMP (left column) and MSIS model (right column) in corrected geomagnetic coordinates between $|55°|$ and $|89°|$. The dial plots in MLT have been retrieved by binning all available density readings of the year 2003. The MSIS colour scale amounts to 80% of the CHAMP colour scale.

Figure 5.1 discloses a synoptic view of the density distribution in MLT as derived from CHAMP accelerometer data throughout the year 2003. This time period has been chosen due to its representative characteristics (average or elevated solar activity, increased geomagnetic activity). The dial plots present the annual average of the northern (upper row) and southern (lower row) hemisphere in cgm coordinates, reaching from $|55°|$ to $|89°|$ cgm latitude. The colour spots in the left dial plots describe the thermospheric mass density that has been derived from accelerometer readings. For comparison the right dial plots depict the corresponding MSIS model density. Section 4.5.1 shed light on the binning procedure.

The obtained pattern is comparable to that of Liu et al. (2005), cf. Fig. 4.3. In essence, we see the diurnal variation of the thermospheric mass density with its maximum in the afternoon and a minimum in the early morning. On the dayside, the air density increases with increasing distance from the poles. This is mirrored in the list of the bins that contain maximal density values (together with MLT and cgm latitude), where we refer to median values of the particular bin. These values are listed in Table 5.1.

Both effects, the diurnal variation and the increase of air density towards lower latitudes are expected to be Sun-driven. Thus, we expect to identify them clearly in geographic coordinates.

Fairly definitely, the absolute maximum at lower latitudes belongs to the mid-latitude maximum (visible in Fig. 4.2), which secondarily depends on geomagnetic activity variations but is primarily controlled by the position of the Sun and the solar EUV radiation (Liu et al., 2005).
However, the region of larger densities is extended towards the dayside auroral regions. It is important for the scope of this work that it is located in the vicinity of the magnetospheric cusp - the region where magnetosheath particles can directly penetrate down to lower atmospheric layers. Indeed, the density values at ≈ 72° – 74° (NH), ≈ -70° – -74° (SH) are slightly enhanced compared to the values of the neighbouring bins. Therefore, it seems reasonable to look for the cause of this enhancement in the domain of geomagnetic processes. This secondary density maximum is accentuated here, because the main task, reason and aim of this study are based on it. We do not expect to recognise this feature in geographic coordinates.

Beside these areas of enhanced density we can pinpoint another secondary maximum in the pre-midnight sector at both hemispheres. Albeit its significantly poor specification - on average its amplitude amounts to about 35% (NH), 40% (SH) of the dayside maximum amplitude - it is worth to be mentioned, since it is probably a geomagnetic-influenced structure which was also identified by Liu et al. (2005) in CHAMP accelerometer data. The investigation of this behaviour was also addressed in Ritter et al. (2008), where the heating efficiency of medium and large-scale FACs at auroral latitudes was considered.
For large-scale FACs (> 150 km) a seasonal dependence with equally distributed currents during equinoxes, strong currents on the dayside during June Solstice and weak currents on the dayside during December solstice were obtained for the NH.
The northern hemispheric medium-scale FACs (15–150 km) are strongest during June Solstice, moderate during equinoxes and weakest during December Solstice. Their local time behaviour remains fixed, showing largest FACs at cusp latitudes and in the pre-midnight sector. Thus, the medium-scale FAC's behaviour resembles that of the thermospheric density. This effect becomes enhanced when considering the average over all seasons.

The observed behaviour is fairly similar to the low latitude observations analysed by Müller et al. (2008): They reveal lowest day-to-night density ratios from CHAMP accelerometer data for a local time sector of 0730/1930 LT and conclude a thermospheric response time to the solar input of 1.5 hours. At least the northern hemispheric distribution in Fig. 5.1 also displays a response time of $\sim$ 1.5 hours, regarding the occurence of the diurnal maximum.

Hitherto, the differences between northern and southern hemispheres have not been mentioned. Indeed, a view on the polar regions reveals a similar large-scale structure

with large mass density values on the dayside, which decline when tracking it over the pole away towards the night/dawn sector.
This reduction happens markedly more rapidly throughout the morning sector (steeper density gradients of $\frac{Max}{Min} = 1.65$ in 4.67 hours in the NH ($\frac{Max}{Min} = 1.93$ in 7.62 hours in the SH) than in the evening sector ($\frac{Max}{Min} = 1.43$ in 5.67 hours in the NH; $\frac{Max}{Min} = 1.79$ in 9.78 hours in the SH). However, this distribution - as indicated by the figures above - is less well-ordered in the southern polar thermosphere. The southern-specific arc-like structure is an artefact of the binning procedure. It has to be noted that this behaviour is not universal. It depends on the season-MLT-distribution.

It remains the comparison of the satellite data with the atmospheric model NRLMSISE-00, briefly referred to as MSIS throughout this study. The MSIS-derived density for an altitude of 400 km is displayed in the right column of Fig. 5.1, again for both hemispheres of 2003, but with a different colour scale.

The model densities in both hemispheres reflect only the diurnal density variation. We find peak values of $4.09 \times 10^{-12} kg/m^3$ at 1414 MLT and 56° cgm latitude (NH), $3.21 \times 10^{-12} kg/m^3$ at 1224 MLT and -56° cgm latitude (SH) in the afternoon sector. The asymmetry of the density gradients in the dial plots is in debt of the presentation in geomagnetic coordinates. The same is seen in the satellite data distribution on the left. Apart from that, the model data exhibit only few local features. A marked-off maximum in the vicinity of the cusp cannot be identified.

Besides the expectedly low (up to no) resolution of local or small-scale events in the model data we notice that the MSIS values underrate the satellite data by 31.3% (NH); 46.8% (SH) on average in all bins. This underestimation becomes markedly enhanced in the vicinity of the cusp ($\approx$ 36.9% (NH); $\approx$ 50.3% (SH)), especially in the southern hemisphere. Vicinity of the cusp in this context was chosen to be between 0800 – 1600 MLT and poleward of $|65°|$ cgm latitude.

Figure 5.2 displays the density distribution in a geographic frame and solar local time. Analogue to Fig. 5.1 the CHAMP density can be found in the left column, the MSIS density in the right column, each of them separated by hemispheres (top: NH, bottom: SH). To obtain a better contrast the colour scales are shifted down compared to Fig. 5.1. The same dataset was applied, but sorted to geographic latitudes between $|55°|$ and $|89°|$. The innermost ring does not contain any data due to the spacecraft's orbit inclination.

As supposed, the presentation in geographic coordinates mainly reflects the diurnal density variation. Maximal CHAMP density values of $5.71 \times 10^{-12} kg/m^3$ at 1510 LT and 56° (NH); $5.12 \times 10^{-12} kg/m^3$ at 1042 LT and -56° (SH) can be found at the equatorward edge of the dial plots. The density amplitude decreases both, with decreasing distance to the geographic pole, and with increasing distance to the geographic noon sector. As expected, minima occur in both hemispheres in the early morning ($2.16 \times 10^{-12} kg/m^3$ at 0528 LT and 60° (NH); $1.27 \times 10^{-12} kg/m^3$ at 0446 LT and -64° (SH)).

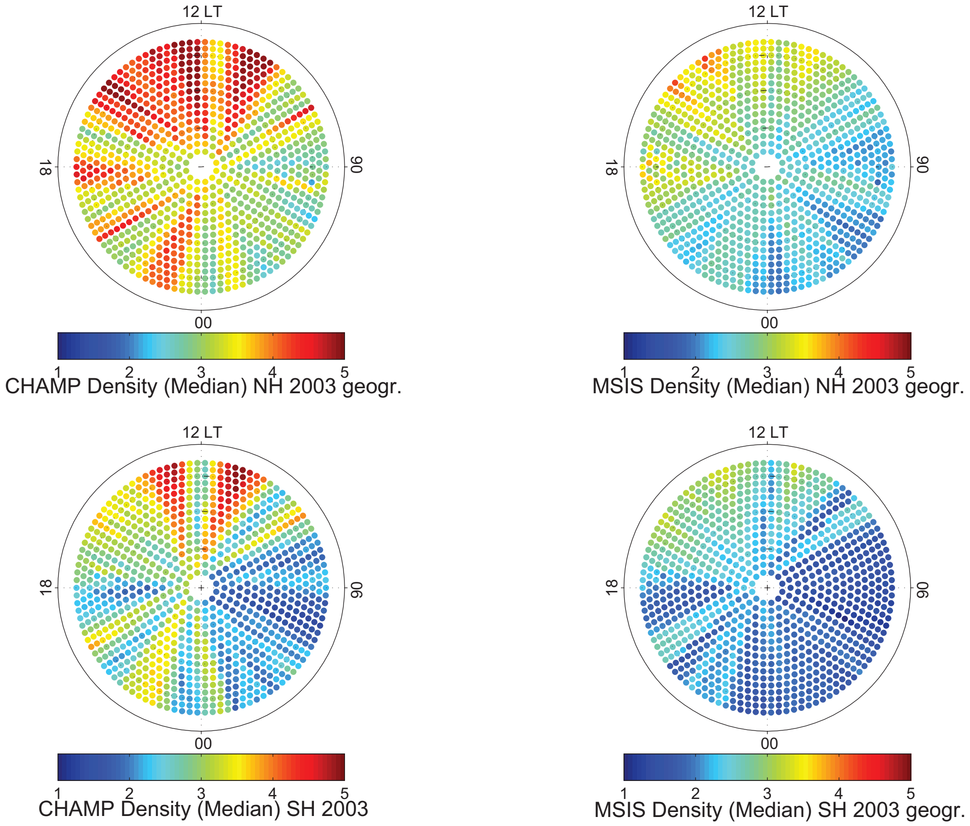

Figure 5.2: Snapshot of the thermospheric neutral mass density in the polar regions of the northern (NH) and southern (SH) hemispheres in 10^{-12} kg/m^3, as derived from CHAMP (left column) and MSIS model (right column) in geographic coordinates. The dial plots have been retrieved by combining all available density readings of the year 2003.

The satellite passes through one hour of local time in about 11 days. In the binning process, 2-3 consecutive readings can be dropped into the same bin. If this 11-day period is characterised by elevated activity, the corresponding density values are larger, too. After a 131-day interval the satellite visits the same local time sector again. If this happens in another high activity phase, the density values are possibly larger than in the neighbouring bins. Analogue incidents hold for sectors and phases of low activity/low densities and explain the spokelike pattern.
Additionally, 131 days almost correspond to the 135-day period of five complete rotations of the Sun. This may support a superposition of activity phases. As a consequence, a pattern with ten ”density spokes” can be expected. Indeed, Fig. 5.2 reveals 9–10 ”density spokes”.

MSIS shows a similar behaviour, but - just like in Fig. 5.1 - with weaker amplitudes: While the density maxima only amount to $4.37 \times 10^{-12} kg/m^3$ at 1400 LT and 56° (NH); $3.43 \times 10^{-12} kg/m^3$ at 1317 LT and -58° (SH), even the minima are poor: $1.82 \times$

$10^{-12} kg/m^3$ at 0538 LT and 60° (NH); $0.99 \times 10^{-12} kg/m^3$ at 0433 LT and -68° (SH). Indeed, the presentation in geographic coordinates demonstrates the dependence of the neutral density at high latitudes on solar/geomagnetic activity, but it solely depicts the diurnal variation. Thus, it implies that other phenomena like the local density enhancements in the vicinity of the cusp and in the pre-midnight sector have to be understood as geomagnetic signatures.

Upshot: The density distribution in 400 km altitude is mainly characterised by the superposition of solar and geomagnetic effects (e.g. Rentz (2005), Guo et al. (2007), Liu et al. (2005)). The solar effects are primarily described best in geographic coordinates but the geomagnetic effects in geomagnetic coordinates. This implies that the hemispheric differences can be related to the larger offset between geographic and geomagnetic poles in the southern hemisphere. According to IGRF model results for 2003, the geomagnetic pole in the northern hemisphere was located at 82.3° N, 114.0° W, the geomagnetic pole in the southern hemisphere at 64.6° S, 138.1° E. This influences the balance between ion drag, Coriolis force and the curvature term, leading to a less well-ordered distribution of neutral air features in the South compared to the northern hemispheric distribution. Similar conclusions have been drawn in the work of Förster et al. (2008) or Wang et al. (2005), for instance.

The analysis of the Figs. 5.1 and 5.2 reveals

1. solar-induced features such as the diurnal variation and the latitudinal density gradient can be identified in both coordinate systems,
2. the influence of magnetospheric effects and electrodynamic forces, for instance the density enhancement in the vicinity of the cusp and in the pre-midnight sector, are not visible in the geographic frame,
3. binning in geographic coordinates emphasises the appearance of artificial effects like the beating between local time variations and activity periods.

Consequently we decided to use for our study exclusively the geomagnetic frame to display the density phenomena at auroral latitudes.

5.2 Approach for the density anomaly estimation

Our approach for deriving the mass density from CHAMP accelerometer and performing the height-normalisation is described adequately in Section 4.4 and Appendix A.

Based on the obtained density data (according to Eq. (4.1)) of all available overflights over the dayside northern and southern auroral regions during the years 2002-2005 the density anomalies have been estimated and analysed as illustrated in the following.

In order to focus on the density anomaly at cusp latitudes we remove large-scale features, such as the diurnal and/or latitudinal variations from the records. This is

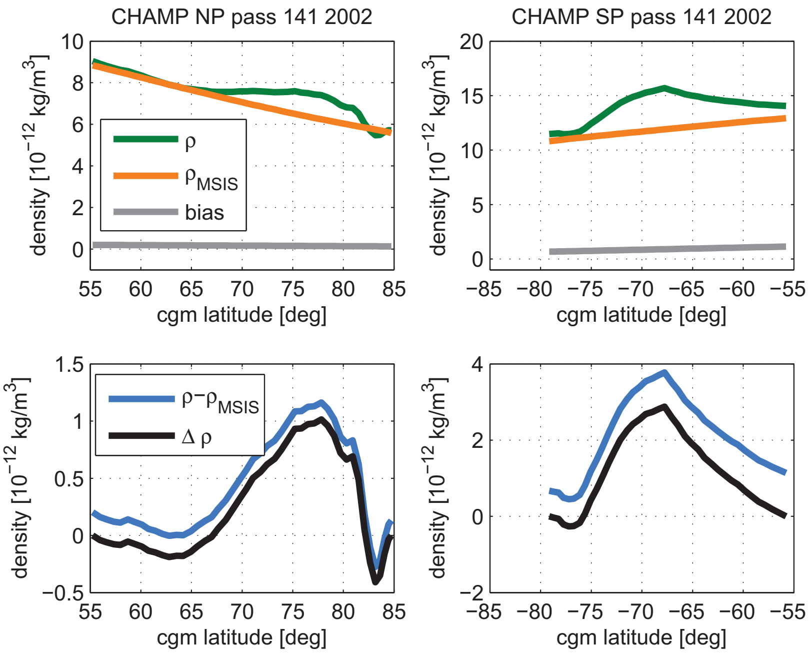

Figure 5.3: Schematic overview of the anomaly identification procedure for the example of the overpass 141/2002 (10 January 2002). The left panels refer to the northern hemisphere and the right panels to the southern hemisphere part of the pass. The upper panels display the density from CHAMP data (green), the corresponding model density from NRLMSISE-00 (orange), and the linear bias function (grey). In the lower panels, the blue line indicates the difference between CHAMP-measured and NRLMSISE-00 density. The black line denotes the final density anomaly, $\Delta\rho$, which is used in this study.

done by subtracting the corresponding NRLMSISE-00 density. In addition a remaining density bias between model and observation is removed. For the determination of the bias we take the differences between observed and predicted densities at 55° and 89° corrected geomagnetic (cgm) latitude and interpolate linearly between these points. Figure 5.3 illustrates the background removal approach for one cusp crossing in both hemispheres. The CHAMP density, ρ, and the corresponding NRLMSISE-00 density, ρ_{MSIS}, are derived for the same location and point in time and for the same geophysical conditions. MSIS does not reproduce local features at high latitudes well. Therefore it is appropriate for separating the large-scale background features from the detailed CHAMP density readings. As expected, a latitude dependent trend is left in the observations along an overpass, which is removed by the so-called linear bias. In Fig. 5.3 this linear trend is displayed in grey. It is also subtracted from the observed density data. Hence, the density anomaly, $\Delta\rho$, is calculated:

$$\Delta\rho \;=\; \rho - \rho_{MSIS} - \rho_{bias}. \tag{5.1}$$

Here, ρ is the density derived from the accelerometer readings according to Eq. (4.1), ρ_{MSIS} is the MSIS model density related to the measurement of ρ, and ρ_{bias} is the corresponding density value from the linear bias function. Therewith, we are able to eliminate the influence of large-scale variations from our mass density anomaly, $\Delta\rho$.

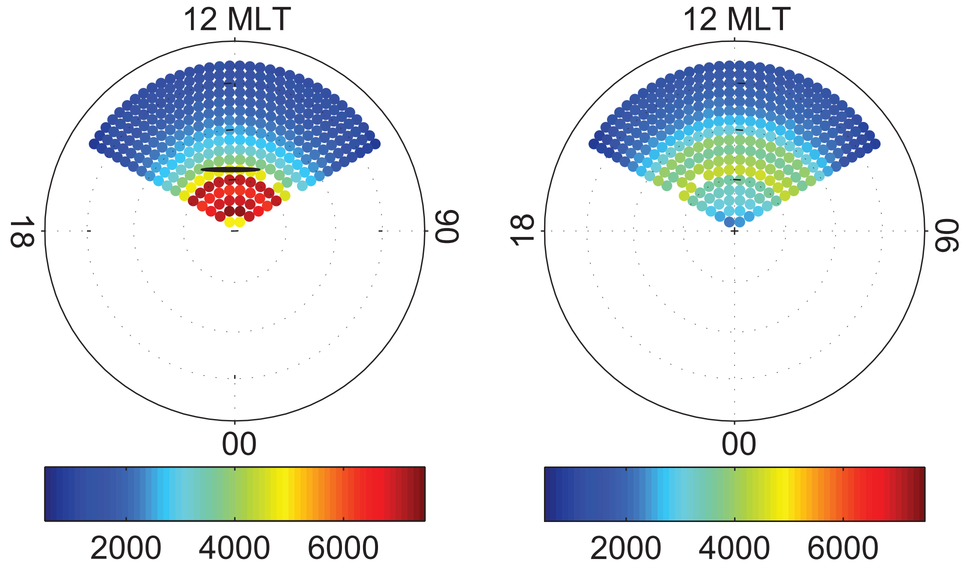

Figure 5.4: Sample number per bin, distribution from all CHAMP passes 2002-2005 over the dayside northern (left) and southern (right) hemisphere. The northern hemispheric magnetospheric cusp location quoted by Newell and Meng (1992) was inserted in black.

We make use of four years of CHAMP data (1 January 2002 - 31 December 2005) to investigate the statistical features of the mass density anomaly in the dayside high-latitude thermosphere. From the selected interval a total of 22734 passes over the northern polar area and 22668 passes over the southern polar area are considered. The data are sorted by cgm coordinates using the APEX system (Richmond, 1995) in order to emphasise the magnetospheric input. The advantages of the geomagnetic coordinate system are demonstrated in Section 5.1. Since we are interested in daytime features, we pick all measurements taken between 0800 and 1600 MLT. A range of $|55|\ldots|89|^\circ$ cgm latitude is selected. By choosing this segment of latitude and local time we intend to cover the cusp location and the surrounding areas since we want to capture the whole density anomaly distribution for various geophysical conditions.

For a binning of the data, the polar region is divided into 918 quasi equal-area bins. The binning procedure is equivalent to the one applied in Lühr et al. (2007) and was already used to derive the density distribution in Section 5.1. All available density value samples, ρ, from a pass over a bin are dropped into the appropriate bin. The large number of passes ensures many entries in each bin, ranging from >8000 near

the pole to at least 500 at 55° cgm latitude.
The sample distribution is shown in Fig. 5.4, where all available overflights have been combined. Figure 5.5 shows the distribution of anomaly detection numbers for the different P10.7 levels, separately for the two hemispheres. If the $\Delta\rho$ maximum of an overpass was detected between $|60°|$ and $|80°|$ cgm latitude and 0800 and 1600 MLT we regard it as an anomaly event.

We use P10.7 values as a controlling parameter with a time lag of 1 day, as recommended by Guo et al. (2007). Most density peaks occur during phases of low solar activity ($P10.7 \leq 130$) with highest occurrence rates within the interval $95 \leq P10.7 \leq 105$. There are rather few events in the interval around $P10.7 = 140$. This local minimum can be regarded as a demarcation line between high and low solar fluxes. The occurrence number in the last bar is an accumulation of all events with $P10.7 \geq 215$. The distribution is almost the same in both hemispheres. All together, we have detected 13787 (13051) density anomalies in the northern (southern) hemisphere.

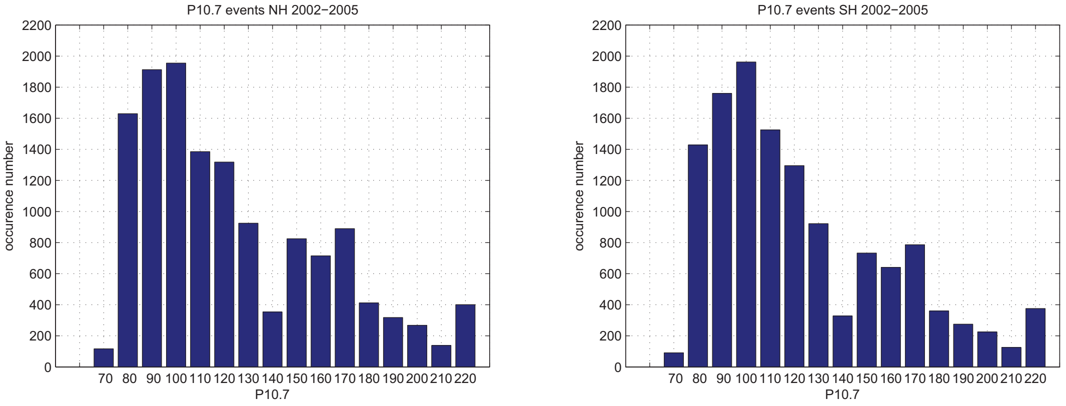

Figure 5.5: Occurrence distribution of density anomaly detections at different P10.7 levels. In the bar $P10.7 = 220$ all events from higher flux levels are accumulated.

5.3 Statistical analysis and climatological representation of the density anomaly

This section synopses the density anomaly distribution over the course of the considered four years and during the different seasons. Both hemispheres are examined. Height-normalised density anomaly values are displayed.

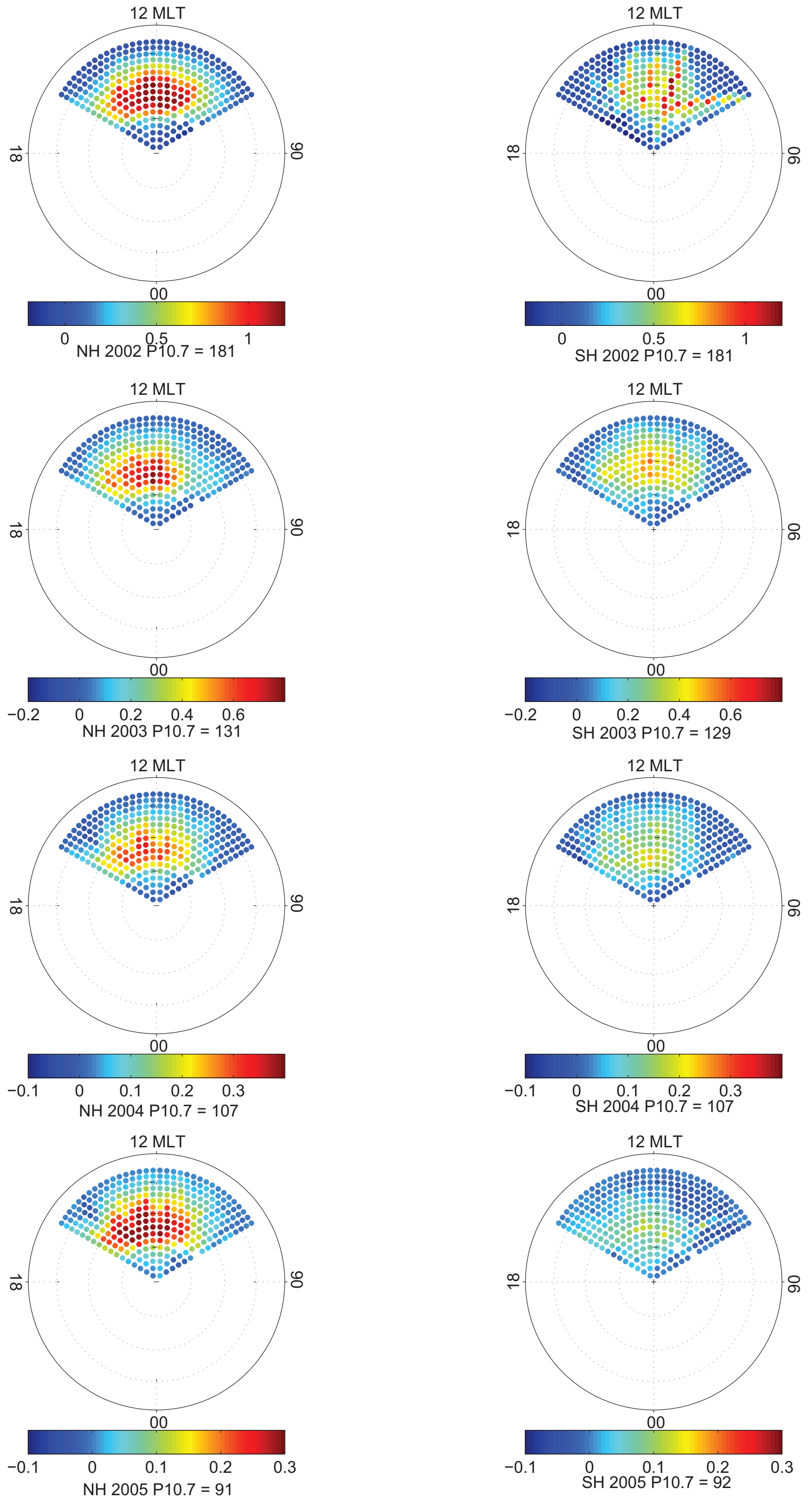

Figure 5.6: Statistical survey over four years of the density anomaly amplitude (in $10^{-12} kg/m^3$) within the dayside polar region of the northern (left column) and the southern (right column) hemisphere. Note the different scales. Yearly averaged P10.7 values are listed below the plots.

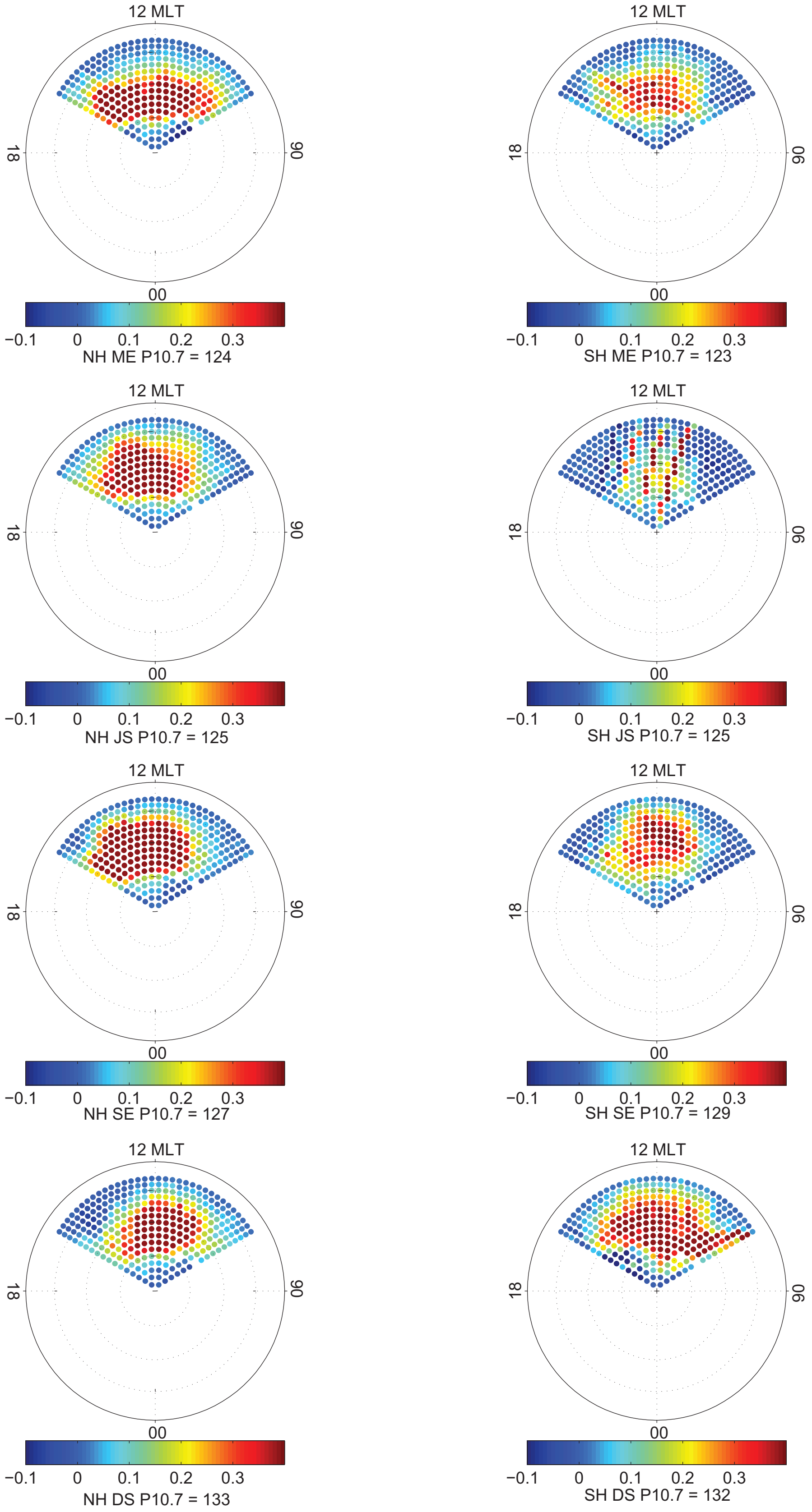

Figure 5.7: Seasonal dependence of the density anomaly in the dayside polar region of the northern (left column) and southern (right column) hemisphere for March Equinox (ME, first row), June Solstice (JS, second row), September Equinox (SE, third row), and December Solstice (DS, fourth row). Average solar flux values (P10.7) are listed below the plots.

Figure 5.6 presents the observed density anomaly distribution, $\Delta\rho$ (mean values, normalised to 400 km altitude) in the dayside polar cusp separately for the years 2002 - 2005. The left column displays the northern hemispheric situation; the right column reflects the southern hemispheric distribution. Concentric rings mark the magnetic latitudes 60°, 70°, 80°. The numbers outside the circle flag the magnetic local time. We present density values, $\Delta\rho$, in the 0800–1600 MLT sector between $89\ldots55^\circ$ ($-89\ldots-55^\circ$) cgm latitude for the northern (southern) hemisphere. Due to the large change of the density anomaly amplitude with time, we use different scales for the years.

The density enhancement is visible in each frame. At northern cusp latitudes, it is most intensive in 2002 with average density anomalies of up to $1.43 \times 10^{-12} kg/m^3$. However, it is decreasing by a factor of almost 6 until 2005. The latitudinal spread of the area of large density anomalies decreases continuously from 2002 to 2005. Considering the full latitudinal width at half maximum (FWHM, cf. Table 5.2) of the mean density anomaly distribution as a characteristic number, it reduces from

time period	max $[10^{-12} kg/m^3]$	std	cgm lat [°] ± 1°	FWHM [°]	MLT ± 15 min
			NH		
2002	1.43	1.75	74	13.8	1145
2003	0.83	1.16	74	13.6	1215
2004	0.37	0.67	72	12.8	1240
2005	0.24	0.49	72	12.9	1307
ME	0.69	1.07	74	12.3	1115
JS	0.70	0.97	72	15.9	1213
SE	0.85	1.16	72	14.0	1333
DS	0.83	1.50	74	12.8	1145
			SH		
2002	1.33	9.01	-68	16.7	1105
2003	0.58	0.95	-70	14.6	1213
2004	0.25	0.59	-76	16.1	1217
2005	0.14	0.44	-76	13.0	1109
ME	0.42	0.84	-76	12.7	1217
JS	0.71	8.23	-	-	-
SE	0.64	1.44	-68	16.8	1105
DS	1.14	8.41	-68	15.2	0854

Table 5.2: Peak and standard deviation (std) of the longitudinally averaged amplitude, its cgm latitude, full latitudinal width at half maximum (FWHM) and the magnetic local time (MLT) of the density anomaly peak in the northern (NH) and southern (SH) hemisphere for the different years and seasons. The standard deviation and the mean error of the average of the FWHM amount to about 10° and 2.43° in latitude in all cases, respectively.

13.8° in 2002 to 12.9° in 2005 in the northern hemisphere. However, the latitude of the average peak is found to stay between 72° and 74°. We obtained the peak density, the cgm latitude and FWHM by averaging the values along each latitude ring and then plotting the profile across all rings. The resulting curve is used for identifying the average amplitude and latitude of the anomaly, as well as for calculating the FWHM. This method (of FWHM derivation) is not straightforward. It requires a Gaussian distribution of the averaged latitudes. That is why we applied the Wilcoxon rank sum test to evaluate the statistical significance of changes in FWHM. The probability of observing equal medians between the given profile and the corresponding Gaussian distribution at an uncertainty level of 5% is > 0.89 except for SH JS. The centre MLT of the density peak moves towards the afternoon with the years. As can be seen in Table 5.2, it appears ≈ 80 minutes later in 2005 than in 2002. This may, however, be an effect of the diminishing anomaly amplitude in the later years so that other auroral processes can have comparable influences on the thermospheric density distribution.
Furthermore we have to take into account the possible influence of height normalisation effects. They may enhance the variation of the background density. This aspect is further discussed in Section 5.5.2.

For comparison, we decided to apply the same scale in Fig. 5.6 for the northern and southern hemispheres. This scale was chosen to fit the northern hemisphere observations, where the phenomenon is more distinct. In the southern polar region the density anomaly is less convincing. Although it can be identified in each year, its structure does not hold any common features. With density values up to $0.58 \times 10^{-12}\, kg/m^3$ it is maximal in 2003 ($\approx 70\%$ of the northern hemispheric 2003 maximum density). The anomaly seems to be shifted to the morning hours compared to the northern hemisphere density distribution.
In the southern hemisphere, the FWHM is largest in 2002 (16.7°) and it reduces to 13.0° in 2005. The central latitude varies more than in the North, ranging from -68° in 2002 to -76° in 2004.
In Fig. 5.6, we noted the yearly averaged P10.7 values below each dial plot. They have been retrieved by averaging the P10.7 values of the considered overpasses. Synchronously with the intensity of the density peaks, but at a lower rate, the P10.7 index decreases with the years. In fact, it reduces by a factor of 2 between 2002 and 2005. This indicates a significant and over-proportional dependence of the density anomaly on the solar cycle.
To separate other dependences independently from the year/P10.7 distribution, the dataset was sorted by season. The results are presented in Fig. 5.7. The format is the same as for Fig. 5.6. Again, the left column displays the northern hemispheric situation, the right column the southern hemispheric one. The expressions March Equinox (ME), June Solstice (JS), September Equinox (SE), and December Solstice (DS) refer to the day-of-year episodes 40-128, 129-220, 221-312, and 313-39, respectively. The density anomaly appears in every season. As expected, it is more distinct at northern latitudes. The peaks appear at 74° cgm latitude during ME and DS, but they are shifted by almost 2° towards the equator during JS and SE.

While the FWHM is 15.9° for JS, it ranges only between 12.3° and 14.0° in the other seasons. The P10.7 values are more balanced between the seasons than between the years, attaining values from 123 (southern ME) up to 133 (northern DS).

The seasonal dependence of the southern hemispheric density anomaly is quite different from the northern hemispheric one: First, the amplitudes are on average smaller by 10%. The smallest amplitudes occur during JS (southern winter), where the anomaly is hardly visible. Instead, we see single tracks from very active days. Second, the area of maximal density is less confined at southern latitudes, especially during ME and DS. Third, the seasonal variation of the peak location is less pronounced in the South. Owing to the fact that we took into account also active periods (when the neutral mass density is strongly enhanced) the maxima in JS and DS are governed by single tracks of storm days. They are not considered as cusp-related. Since they introduce large variations, they are not further included in the interpretation.

Similar seasonal density variations have been found by Liu et al. (2007) for low latitudes. These authors presented annual and semi-annual variations with density maxima around equinoxes and a minimum at JS. A possible explanation for that was given to be the thermospheric spoon mechanism, suggested by Fuller-Rowell (1998) and related to the stronger mixing of the atmosphere during equinoxes.

We observe an almost permanent occurrence of the density enhancement but with a significant variability. The density bulge changes with time and season both in intensity and position. Hence, we infer a multi-parameter dependence which is considered in the following section.

5.4 Controlling parameters

To efficiently characterise the density anomaly its dependence on different parameters has been investigated. As demonstrated in Section 5.2 the solar activity (P10.7) has been identified as a controlling parameter. The merging electric field, (E_{merg}), and the background density ($d\rho_{rel}$) are even more important driving parameters, as will be presented below. A minor role is played by solar zenith angle and tilt angle.

5.4.1 Set of parameters

F10.7 / P10.7

The solar flux variation is approximated by the F10.7 and P10.7 indices, which reflect the strength of the EUV radiation. According to Guo et al. (2007) a use of multiple solar irradiance indices, in fact a combination of F10.7, and the solar flux contributions S_{EUV} (30-120 nm) and S_{FUV} (120-130 nm) with a time lag of 1 day provides a higher correlation than using exclusively F10.7. Similarly good results can be obtained when applying the P10.7 index from the previous day, which is calculated as:

$$P10.7 = \frac{1}{2}\left(F10.7 + \overline{F10.7_{81days}}\right), \tag{5.2}$$

(Richards et al. 1994). Previous studies have shown that P10.7 is more appropriate as a linear indicator also for the ionospheric response to solar EUV radiation (L. Liu et al., 2006). As can be seen from their Fig. 1, P10.7 gives smoother solar flux variations than F10.7 which gives more emphasise to the shorter activity phases. Since we are interested in the climatological behaviour, we prefer P10.7. The F10.7 values are downloaded from the SPIDR website http:/spidr.ngdc.noaa.gov/.

Merging electric field

An important quantity controlling the solar wind-magnetosphere coupling processes is the interplanetary magnetic field (IMF). The IMF components B_y and B_z, which are considered in this study, are derived from the 1-min final data of the Advanced Composition Explorer (ACE) satellite, published by the NASA Science Center. The transit time of each reading from the ACE location at the Lagrange point between Sun and Earth, $L1$, to the magnetopause was computed individually using the actual solar wind speed data. Following Vennerstrøm et al. (2002) another time delay of 15 minutes was added to take account of the distance between the magnetopause and the polar ionosphere. The merging electric field, E_{merg}, has been derived from merging theory assuming that there is an equal magnitude of the electric field in the solar wind, the magnetosheath and on the magnetospheric side of the magnetopause (Kan and Lee, 1979):

$$E_{merg} \;=\; v_{SW}\sqrt{{B_y}^2 + {B_z}^2}\;\sin^2\left(\frac{\theta}{2}\right), \tag{5.3}$$

where B_y and B_z are the IMF components, v_{SW} is the solar wind speed, and θ the IMF clock angle in Geocentric-Solar-Magnetospheric (GSM) coordinates. In a superposed epoch analysis Ritter et al. (2004a,b) found the merging electric field to be a suitable geoeffective solar wind parameter. Therefore, in our study the merging electric field will be used as a measure for the solar wind input to the magnetosphere.

Background density

The total mass density, ρ, as calculated via Eq. (4.1) is subject to both large-scale and small-scale influences. We intend to find the dependence of the size of the anomaly, $\Delta\rho$, on the ambient air mass density. Therefore we calculated the relative density anomaly, $d\rho_{rel}$:

$$d\rho_{rel} \;=\; \frac{\rho}{\rho - \Delta\rho}. \tag{5.4}$$

It is used to investigate the impact of the background density on the anomaly.

Solar zenith angle

The dependence on the solar irradiation of the Sun can be sufficiently described by the solar zenith angle (SZA). It is the Sun's angular distance from the vertical and depends on season and local time. It can be calculated as:

$$\cos\left(SZA\right) = \sin\phi\sin\delta + \cos\phi\cos\delta\cos t \tag{5.5}$$

where ϕ is the geographic latitude, δ is the solar declination, and t is the local time as angle. For $SZA > 100°$ the ionospheric E region is in darkness, for $SZA \leq 100°$ it is sunlit (Schlegel, 1988). The SZA is used in this study for estimating the ionospheric conductivity.

FACs and tilt angle

Apart from the merging electric field FACs are able to transfer energy and momentum from the solar wind into the high-latitude thermosphere-ionosphere system. Lühr et al. (2004) supposed the density anomaly to be connected to small-scale FACs. Vogt (2002) stated that the energy transfer from field-aligned electric currents into heat is most effective for scales of the order of 10 km when assuming typical ionospheric conductivities.

The tilt angle describes the angle between the Earth's dipole axis (North) and the GSM z-axis. When the northern hemisphere tilts towards the Sun, the tilt angle counts positive and negative when tilted towards the nightside.

The cusp position depends on the tilt angle (Russell, 2000). As the dipole tilts towards the Sun, the cusp moves poleward. The larger the positive tilt angle the more poleward is the cusp position in the northern hemisphere. Newell and Meng (1991) report on a shift of 1° in latitude per 17° tilt angle variation. Zhou et al. (1999) found a dislocation of 1° per 14°. Since the process is influenced by further parameters, e.g. IMF orientation and variability, and since Newell and Meng (1991) investigated lower altitudes (830 km) with DMSP, and Zhou et al. (1999) investigated higher altitudes (several Earth radii) with the Polar satellite, the reported values can be considered consistent.

5.4.2 Influence of the controlling parameters

The solar wind plasma and the embedded IMF feed kinetic and electric energy into the magnetosphere. We therefore investigate a possible dependence of the density anomalies on the IMF B_z component and/or the IMF merging electric field, E_{merg}, as proxies for an energy input. Figure 5.8 presents results of a superposed epoch analysis applied to IMF B_z and E_{merg} data observed around the density peak detection time. Only the maximum $\Delta\rho$ values of each overflight, called $\Delta\rho_{max}$, have been taken into account. Here we make use of air density estimates which are not normalised to 400 km altitude. This decision is explained in Section 5.5.2. To avoid smearing-out effects we focused on well-developed anomalies with amplitudes of more than $1 \times 10^{-12}\, kg/m^3$, called $\Delta\rho_{high}$, leaving 5121 (2672) events in the northern (southern) hemisphere for investigtion. This might imply that we prefer values of active periods, but as we discovered in Fig. 5.6, the phenomenon is more distinct at an elevated activity level. Each CHAMP overpass was checked for a sufficiently large density maximum, and the detection time was defined as the key time, $t = 0$. We considered the respective solar wind parameters in time segments of ±1.5 hours around the key time, stacked the data of all overpasses and averaged the compiled index curves as running means with time steps of 10 minutes. The analysis has been performed separately for the four seasons. Due to the small number of peaks

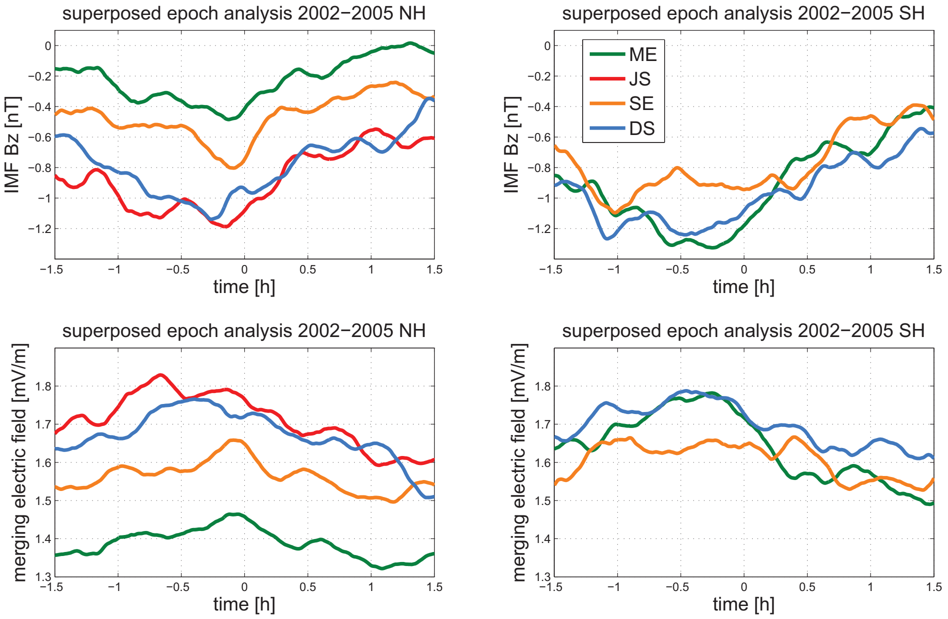

Figure 5.8: Average variation of the IMF B_z component (upper panels) and the IMF merging electric field, E_{merg}, (lower panels) during the ±1.5 hours around the density peak, as resulting from a superposed epoch analysis. Results from the different seasons are plotted separately. The green line indicates March Equinox (ME) conditions, the red June Solstice (JS), the orange September Equinox (SE), and the blue line the December Solstice (DS) conditions.

with amplitudes above $1 \times 10^{-12}\, kg/m^3$ we did not take into account the southern hemispheric JS conditions in the superposed epoch analysis.

The purpose of the superposed epoch analysis is more a qualitative rather than a quantitative one. We wanted to find out to which processes in the solar wind the density anomalies are related. The left column of Fig. 5.8 displays the IMF B_z/E_{merg} variations for northern hemispheric events and the right column those for the southern events. The IMF B_z variations show an absolute minimum shortly before the key time for every season. This feature is more prominent in the northern hemisphere, where it occurs between 16 minutes (DS) and 6 minutes (JS) before the key time. In the southern hemisphere, the time interval between the IMF B_z minimum and the time of the density peak detection amounts to 15 minutes on average. Oppositely to B_z the superposed epoch analysis for E_{merg} reveals a maximum shortly before the key time. The positive excursion stretches over a longer period of 96 min on average (NH) and 102 min (SH). According to the mean error of the average we have to expect a temporal uncertainty of $0.6 - 1.9\%$ for B_z and $0.1 - 0.2\%$ for the E_{merg}. The analysis of both parameters, B_z and E_{merg}, indicates that an enhanced energy input occurs shortly before the detection of a cusp density peak. In order to get a representative number for the solar wind input related to the events, we calculated the mean value of E_{merg} from the 40 minutes preceding the key time. With the help of this procedure each cusp density anomaly is affiliated with an E_{merg} value. An additional 15 minutes delay of the thermospheric response to the solar wind impact at the magnetopause has been taken into account.

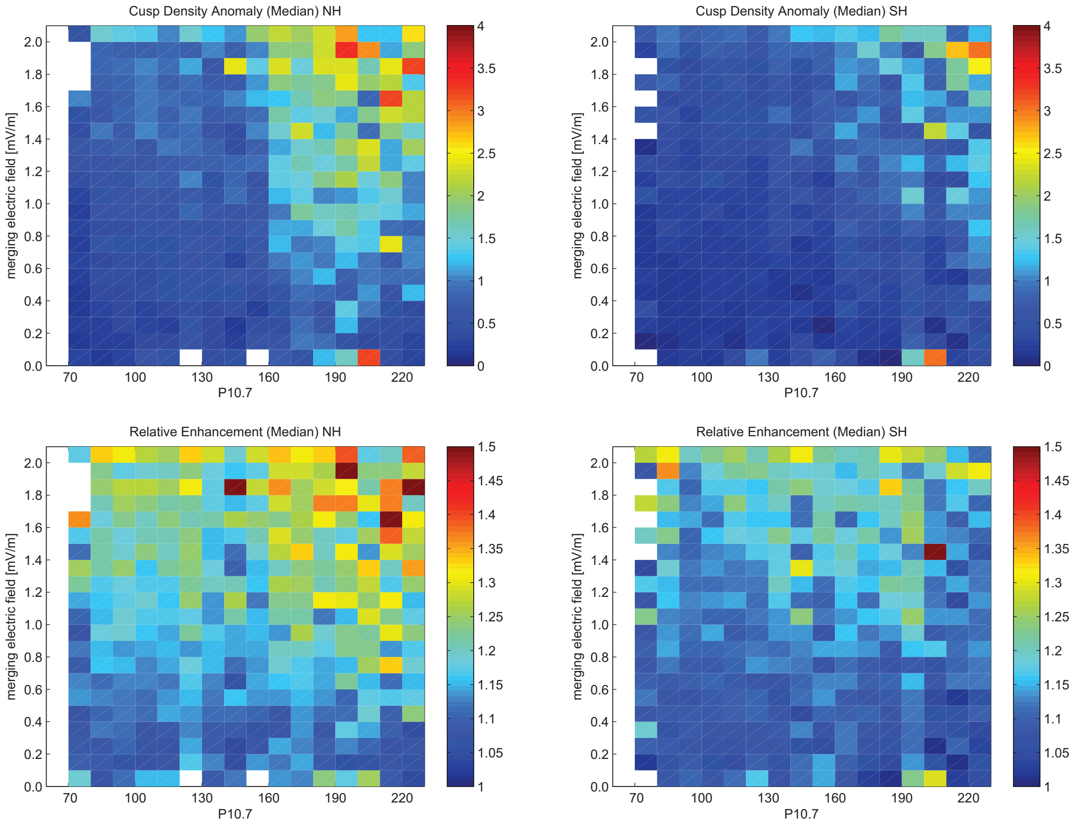

Figure 5.9: A 2D-distribution of the density anomaly (in $10^{-12} kg/m^3$, colour scale) depending on E_{merg} and P10.7 for both hemispheres (upper row). Largest density values are concentrated in the sector of high solar activity and elevated E_{merg} values. The same is displayed for the relative anomaly (lower row). Large relative enhancements occur at elevated E_{merg} conditions over a wider range of P10.7 levels.

In Section 5.2 we showed that the amplitude of the density anomaly depends on the solar flux level. Here we find a relation to the solar wind input. For that reason we performed a 2-parameter analysis. Density values, $\Delta\rho_{max}$ at orbital altitude, are sorted into a solar flux versus merging electric field matrix.

The results are presented in the top row of Fig. 5.9, where we depict the median amplitude of the density anomaly in colour, separately for the hemispheres. Here, we did not restrict the event selection to any amplitude threshold. The only criterion for the peak value is that it occurs within the latitude range 60° to 80° cgm latitude. The most striking feature is the dominance of large density anomalies in the high

P10.7/elevated E_{merg} sector. This constellation occurs at northern and southern latitudes. Obviously, it requires a combination of enhanced solar flux and solar wind input for the cusp anomalies to become large. Determined quartiles are $Q_{.25} = 0.52 \times 10^{-12}\,kg/m^3$ and $Q_{.75} = 1.30 \times 10^{-12}\,kg/m^3$ for the NH. For the SH we obtain $Q_{.25} = 0.27 \times 10^{-12}\,kg/m^3$ and $Q_{.75} = 0.80 \times 10^{-12}\,kg/m^3$. For geophysical conditions of $P10.7 < 150$ and $E_{merg} < 1\,mV/m$ hardly any events are detected. In both hemispheres, bins with $P10.7 < 150$ do not contain median densities $> 2 \times 10^{-12}\,kg/m^3$. There are also only less than 5 bins with density anomalies $> 2 \times 10^{-12}\,kg/m^3$ for $E_{merg} < 1\,mV/m$.

The same 2D-analysis as above was performed for the relative density enhancement, $d\rho_{rel}$. We intended to determine the role of the background air density for the formation of the anomaly. The obtained results are presented in the bottom row of Fig. 5.9. In all cases we used density readings from the spacecraft's orbit altitude. The picture is different from that of the absolute amplitude of the anomaly. The dependence on solar flux level is clearly reduced. Here, the relative size of the density anomaly depends mainly on E_{merg}, the solar wind input. Median ratios up to 1.5 can be detected. Also for this quantity the effect is markedly stronger in the northern hemisphere. For merging electric fields between 1 and 2 mV/m we find relative density enhancements varying around 1.3 in the northern hemisphere and around 1.2 in the southern hemisphere. For the relative density enhancements we find quartiles of $Q_{.25} = 1.13 \times 10^{-12}\,kg/m^3$ ($Q_{.25} = 1.09 \times 10^{-12}\,kg/m^3$), and $Q_{.75} = 1.24 \times 10^{-12}\,kg/m^3$ ($Q_{.75} = 1.17 \times 10^{-12}\,kg/m^3$) for the northern (southern) hemisphere, respectively. The hemispheric differences will be discussed below.

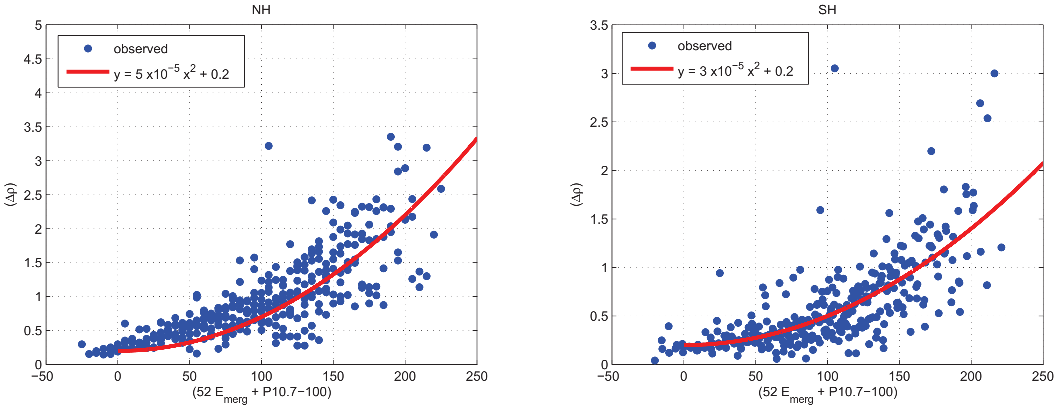

Figure 5.10: Dependence of the density anomaly on the optimal linear combination of the controlling parameters. There seems to be a quadratic relation between the anomaly strength and the parameters. The red curve represents the parabolic best fit to the observations.

It becomes clear that the strength of the anomaly is strongly dependent on the preconditioning of the upper atmosphere. Very important is the intensity of the solar flux level, P10.7, of the previous day. In Fig. 5.6 we have seen that the

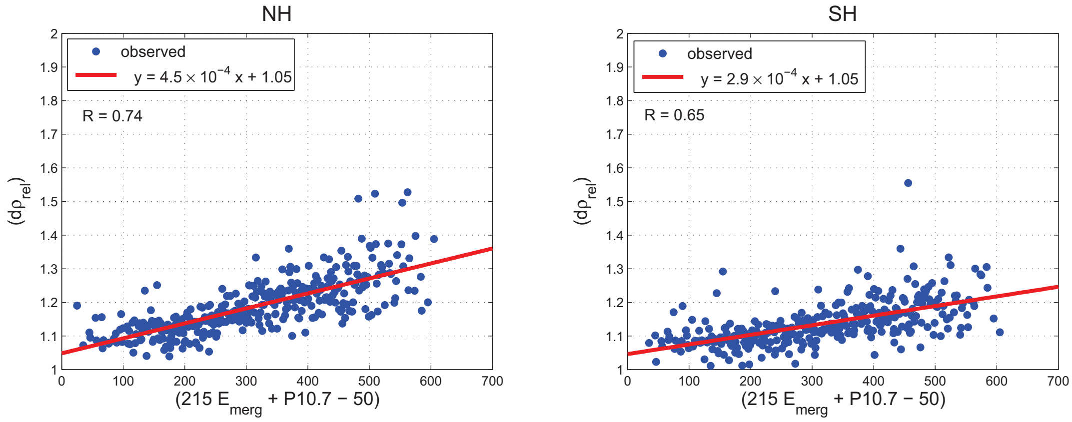

Figure 5.11: Dependence of the relative density deviations on the optimal combination of the controlling parameters. There seems to be a clear dominance of E_{merg}. The red line represents the linear best fit to the observations.

amplitude of the anomaly seems to reduce faster than the solar flux level, at least within the resolvable range of our statistical analysis. The upper row of Fig. 5.9 seems to support these suggestions.

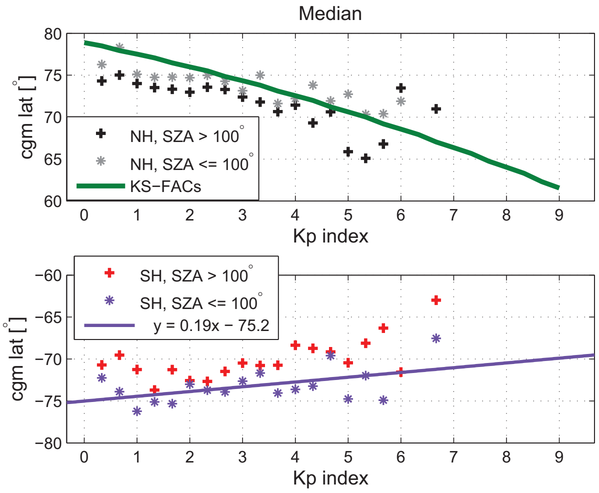

Figure 5.12: Dependence of the median latitude of density anomaly peaks on the magnetic activity, Kp index, for the northern (top panel) and southern (bottom panel) hemisphere. The latitudes of the anomaly peaks are determined separately for two solar zenith angle ranges, where plus signs are from dark and asterisks from sunlit conditions. For comparison, the average latitude dependence of Kilometre-Scale-FACs (green line) is included. A linear regression is added for the southern hemisphere.

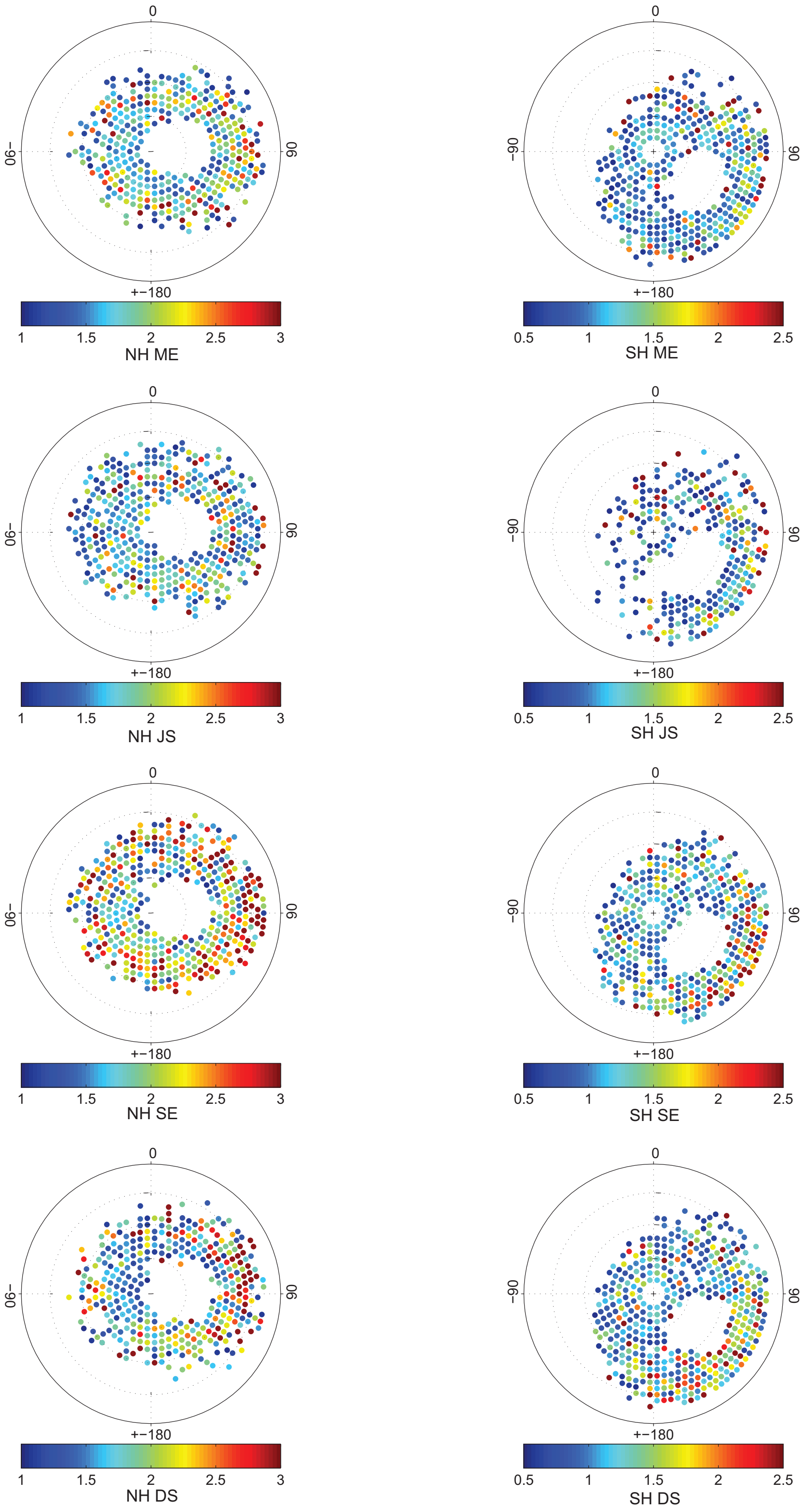

Figure 5.13: The location of the density anomaly peaks in geographic coordinates separately for both hemispheres and the four seasons. Stronger anomalies are more common at lower latitudes.

The other important controlling parameter is the solar wind input, quantified here by the merging electric field. In Fig. 5.9 prominent anomalies are only found for $E_{merg} > 1\,mV/m$. The resulting amplitude of the density bulge is obviously proportional to an additive effect of E_{merg} and P10.7. In order to better describe the functional dependence we have performed a sensitivity analysis to characterise the weights of the two parameters:

$$\Delta\rho_{high} = f\left(bE_{merg} + P10.7 + c\right), \tag{5.6}$$

where b, and c are the parameters to be determined, and for the function, f, we have chosen a parabola. Based on the data presented in the top row of Fig. 5.9 we varied the factor b in Eq. (5.6) until we obtained the narrowest distribution of data points around the parabolic curve. An optimal value is $b = 52$ giving a reasonably narrow point distribution for observations in both hemispheres, as can be seen in Fig. 5.10. The weight of the merging electric field in mV/m is thus more than 50 times higher than that of the solar flux units. It is obvious from Fig. 5.10 that the increase in anomaly amplitude is over-proportional. Furthermore, the anomalies fade away when the combined parameter drops below 100. Eq. (5.6) provides a reasonable approximation for $\Delta\rho$ when we chose a parabolic function with the parameters $b = 52$ and $c = -100$. The respective best fits for the two hemispheres are also plotted in Fig. 5.10. As factors for scaling the fitted curves we obtain $a_{NH} = 5 \times 10^{-5}$ and $a_{SH} = 3 \times 10^{-5}$ for the northern and southern hemisphere, respectively.

It has earlier been stated that the field-aligned currents on the dayside behave like driven by a voltage source (e.g. Wang et al., 2005). The observed quadratic increase of the anomaly strength with the merging electric field is consistent with a voltage source analogue. Moreover, there seems to be a threshold of energy input that has to be surpassed before a density anomaly can form at about 400 km altitude. At this moment we cannot offer a convincing explanation for the necessary preconditioning of the thermosphere required to start the air-upwelling.

The same analyis has been performed for the relative density deviation, $d\rho_{rel}$. The result is depicted in Fig. 5.11. In both hemispheres, it reveals an optimal linear combination of $d\rho_{rel} = 215\,E_{merg} + P10.7 - 50$. The dominance of E_{merg}, which has a weight that is by 215 times higher than that of P10.7, reflects our findings of Fig. 5.9. Below a parameter combination of 50 the anomalies tend to fade away.

Oppositely to $\Delta\rho$ the observed $d\rho_{rel}$ values show a linear dependence on the optimal combination. Best fits are found to be linear functions which are characterised by a slope of $a_{NH} = 4.5 \times 10^{-4}$ for the NH and $a_{SH} = 2.9 \times 10^{-4}$ for the SH and an intersection with the ordinate at 1.05. Under these conditions the highest correlations are obtained, resulting in correlation coefficients of $R = 0.74$ (NH) and $R = 0.65$ (SH).

Here again we find a higher sensitivity on the drivers of the anomaly in the northern hemisphere. The ratio of the scale factors, northern to southern hemisphere, is about 1.5 for both the absolute and the relative anomaly.

Next the parameters of minor influence are investigated. It is well known, that the cusp moves equatorward with increasing magnetic activity. Prölss (2006) reported a close relation between the amplitude of the auroral activity, AE index, and the latitude of the cusp. Unfortunately, the AE index is not available over the full observational period 2002–2005. Similarly, Rother et al. (2007) presented a functional relation between the latitude of their kilometre-scale field-aligned current (KS-FAC) events and the magnetic activity, Kp index. During times of enhanced activity the cusp is displaced equatorward.

We have binned the cgm latitude of each density anomaly, $\Delta\rho_{high}$, by Kp and determined the median latitude for each bin. In this case, the dataset was further subdivided for events in darkness ($SZA > 100°$) and in sunlight ($SZA \leq 100°$). Figure 5.12 shows the results for the northern and southern hemisphere. In general, we see that the equatorward displacement of the density anomaly with increasing Kp values follows the curve of the small-scale FACs reasonably well. The locations of the anomalies detected in sunlight are systematically more poleward. On average, we find a separation by about 2° in latitude. This value is consistent with the reported 2° equatorward shift of FAC locations around noon for events in darkness with respect to those in sunlight (Wang et al., 2005).

Unfortunately, we have no KS-FAC latitude dependence on Kp for the southern hemisphere for comparison. Since the southern hemispheric density anomaly distribution is generally less distinct we focus here on the discussion of the northern hemispheric features. Nevertheless, a linear regression yields an (admittedly small) trend which corresponds to the northern hemispheric result.

It is known, that the amount of sunlight reaching the polar ionosphere is one of the prime controlling factors for the conductivity on the dayside. Furthermore, it has been shown by Wang et al. (2005) that the intensity of field-aligned currents and electrojets is strongly dependent on SZA in the local time sector around noon. If we regard Joule heating as a cause for the air-upwelling in the thermospheric dayside high latitudes, then the conductivity should be a relevant parameter.

A dependence on SZA is expected to be evident rather clearly in the seasonal differences. Figure 5.7 shows the intensity and distribution of the anomaly separated by season. Interestingly, we obtain weakest anomalies in both hemispheres during June solstice months. It is thus difficult to explain that the observed seasonal variations are caused by changes in photo-ionisation. There seems to be another annual variation of the ionosphere-thermosphere system having strong control on the formation of the cusp-related anomalies. In order to separate between this effect and the SZA dependence we have plotted the location and amplitude of the density anomalies in geographic coordinates in Fig. 5.13. As expected, the anomalies are confined to auroral latitudes, leaving a void in the polar cap. The blank circle at the pole is the region not sampled by CHAMP. In this coordinate frame, the SZA changes almost linearly with latitude. We may thus identify SZA dependences in Fig. 5.13. Although large amplitudes (red dots) can be found at all longitudes, there is a somewhat higher concentration at longitudes where the cusp-related area reaches down to lower geographic latitudes. This relation is more evident in the southern hemisphere, where we have a larger distance between geographic and geomagnetic poles.

From this behaviour we may conclude that the amount of solar irradiation has a certain but limited influence on the amplitude of the cusp anomaly. The main seasonal differences can, however, not be explained by the SZA.

The tilt angle can be used for an alternative explanation of the FAC – density anomaly shift seen in Fig. 5.12, in which the latitudinal shift of the cusp is attributed to the dipole tilt angle, not to the influence of solar irradiation. The obtained difference of 2° between the latitudes of events in darkness or sunlight corresponds to a change in tilt angle by ±14°. This fits quite well the average shift in tilt angle between summer and winter season. We are also more in favour with the tilt angle dependence than with the influence of the sunlight. The latitude changes in the southern hemisphere are similar to those in the North but much more scattered. The observed latitude variation adds confidence to our suggestion that the neutral mass density anomalies are related to the magnetospheric cusp region.

The influence of small-scale FACs (kilometre-scale: 1–5 km) has been investigated by Rother et al. (2007) as mentioned before. They have been found to occur preferably in the cusp/cleft region. However, an Alfvén wave resonator with very efficient reflectors on both sides of it was suggested as a possible driver for the observed KS-FACs. Under these circumstances, there should not be much energy left for Joule heating. This might indicate that small-scale FACs do not play a dominant role in ionospheric heating of the atmosphere leading to density enhancements at cusp latitudes, as observed by CHAMP. Obviously, the influence of FACs is a matter of the scale size. However, due to a lack of suitable measurements (in particular particle measurements onboard CHAMP or/and at different altitudes) this has not been proved or rejected yet.

Season	NH Density $[10^{-12} kg/m^3]$	SH Density $[10^{-12} kg/m^3]$
ME	6.71 ± 0.20	6.56 ± 0.35
JS	5.98 ± 0.25	4.17 ± 0.30
SE	5.43 ± 0.20	6.07 ± 0.35
DS	5.16 ± 0.25	7.13 ± 0.25

Table 5.3: Average ambient mass density in the cusp region at a flux level $P10.7 = 150$, separated by season and hemisphere. The data are obtained from the correlation analysis presented in Fig. 5.14.

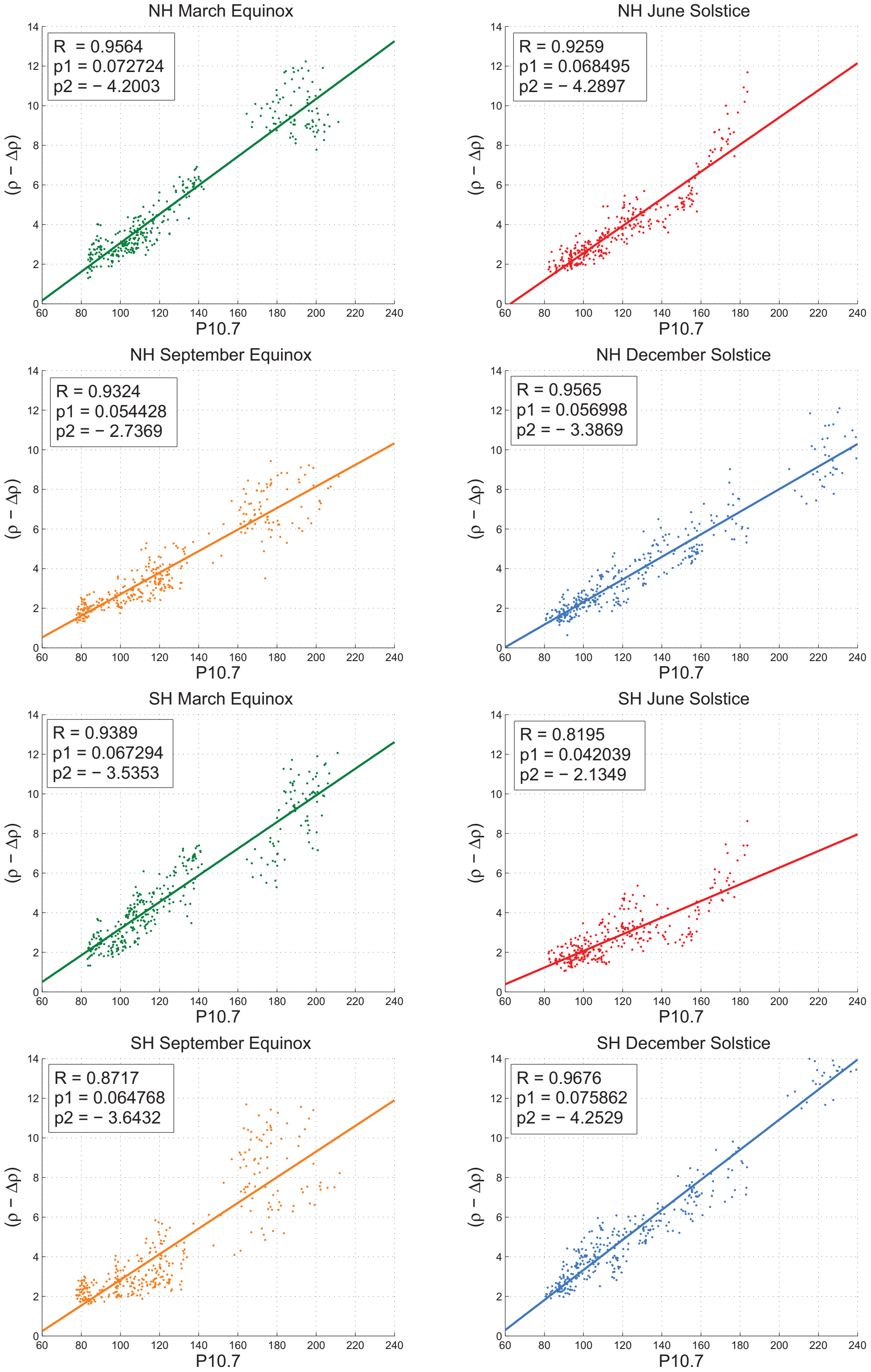

Figure 5.14: Relation between cusp ambient density and solar flux level P10.7. The larger scattering in the southern hemisphere is probably caused by the larger distance between the geographic and geomagnetic poles.

A remaining question is which atmospheric parameter is causing the global annual variation of the cusp-related density anomaly? To answer this question we first take a look at the ambient air density prevailing during the anomaly events. We can compare the background mass density in the cusp region with the solar flux index. Figure 5.14 shows the correlation of the background density, $\rho - \Delta\rho$, versus P10.7, separately for each season and hemisphere. As can be seen, there exist excellent linear relations between these two quantities with large correlation coefficients ($R \sim 0.9$). For that reason, it makes sense to fit a regression line to the data points. The slopes of the lines are an indication of the thermospheric sensitivity to the solar flux intensity. In the northern hemisphere we find values for the slopes between 0.054 and 0.073 for the different seasons. For comparison, Liu et al. (2005) reported for the dayside low latitude a slope of 0.08. In the southern hemispheric cusp the background air density is on average larger than in the North, except for June solstice, when it is markedly depressed (cf. Table 5.3). These observations are consistent with the findings of Liu et al. (2007). In Fig. 4 they present latitudinal profiles of the thermospheric density separately for each season. The difference in the December-June asymmetry between the two polar regions is quite evident in their figure. These seasonal variations of the thermospheric density match rather well the amplitude variation of the cusp-related anomaly, as shown in Fig. 5.7. An annual variation of the thermospheric density has earlier been deduced from satellite orbit analysis. For example, Boulton (1985) reported an air density in the altitude range 240-470 km that is 1.3 times larger in December than in June. Up to date there is no consensus on the mechanism causing this major annual variation.

The combination of the annual variation with the seasonal variation of the insulation produces the strong hemispheric asymmetry during solstices. In the northern hemisphere these two effects are out of phase. The global reduction in air density during June solstice is locally compensated by continuous sunshine. In the southern hemisphere both phenomena vary in phase thus causing large differences between solstice seasons (cf. Table 5.3). Unfortunately, CHAMP does not provide any information on composition. Therefore, we cannot contribute to explaining the annual variation of the thermospheric density in a direct manner. With respect to this study we may recall that an enhanced ambient air density is in favour of the formation of cusp anomalies. The much reduced thermospheric density in the southern polar region during June solstice is suggested to be the cause for the infrequent occurrence of density anomalies in that season.

5.5 Discussion of uncertainty contributions

Our results are affected by different uncertainty contributions considered in the following.

5.5.1 Error budget

As already outlined in Section 4.4.2 the accelerometer's resolution leads to an uncertainty of $6 \times 10^{-14}\, kg/m^3$ in the density. Bruinsma et al. (2004) found an error of at least 10% in x-direction (along-track) and 1 – 2% in y-direction (cross-track). The z-direction was not considered, because expected variations are very small compared to the other axes (cf. Section 4.3), and the data of that component are neither reliable nor applied in this work.

The resolution of the STAR accelerometer instrument is with $3 \times 10^{-9} m/s^2$ good enough to play a minor role. The major error in the measurements may be due to the calibration parameters, causing a systematic error of 2% and a contribution to the noise level of $> 1\%$ (Bruinsma et al., 2004).
A large uncertainty comes from the drag coefficient, C_D. It cannot be calibrated in ground-based laboratories. That is why we assume $C_D = 2.2$ as recommended by ESA. This leads to an uncertainty of the scale factor for the density value.
We have to further take into account the satellite's attitude with respect to the orbit track (and the thereby defined coordinate system). In fact, the satellite permanently oscillates around its axes. If the deviation angle exceeds 2° the satellite is automatically navigated in the opposite direction. The observed deviation angles for the horizontal components are considered in the density derivation procedure, so that the resulting uncertainty is less than 1%.

As can be seen in Eq. (4.1), the thermospheric wind components contribute to the density. Therefore, we have to take into account two more uncertainty sources: (1) the wind error itself and (2) the uncertainty in the density that is caused by the wind.
It is impossible to simulate the spacecraft's environmental conditions in space in a laboratory. That is why the accelerometer could not be calibrated before the launch, leading to a certain error in the wind estimates.
Inter-instrument comparison to FPI measurements (Aruliah et al., 2005) reveals a marked overestimation of the CHAMP-measured wind speeds. Aruliah et al. (2005) respect that the FPI measurements may underestimate the true wind speed by up to 10%. We would not expect the observed large differences between FPI measurements at F region altitude and CHAMP observations in about 400 km altitude, since the vertical wind velocity is mainly controlled by the (temperature-dependent) viscosity which does not vary much in this altitude range. Aruliah et al. (2005) speculate that the vertical wind speeds might be much bigger due to the small-scale variability. This uncertainty, however, only concerns the absolute velocities, not the wind direction. Consequently, we have to keep in mind that the values are obviously afflicted by a considerable systematic error of about 10%. Due to the quasi constant conditions during the CHAMP mission this error has no impact on the wind's relative behaviour and the wind direction. A remaining uncertainty for the derived densities is mainly due to the neglection of head and tail winds. We assume that they average out over a four-year period. Furthermore, Lühr et al. (2007) showed that the horizontal wind velocities in the vicinity of the cusp are fairly low.

5.5.2 Influences of the height normalisation

The spacecraft decays from about 425 km at the beginning of 2002 to about 360 km at the end of 2005. This corresponds roughly to one scale height and is a rather slow variation. Nonetheless, its impact might be significant. We investigated its influence, possible uncertainties due to the height normalisation, and corresponding artificial effects.

It is well known that the thermospheric mass density (and consequently the density anomaly) varies with altitude and solar activity. As revealed in Section 5.5.1 it is necessary to represent the measurement results in a way that ensures comparability but simultaneously leaves preferably original measurements.

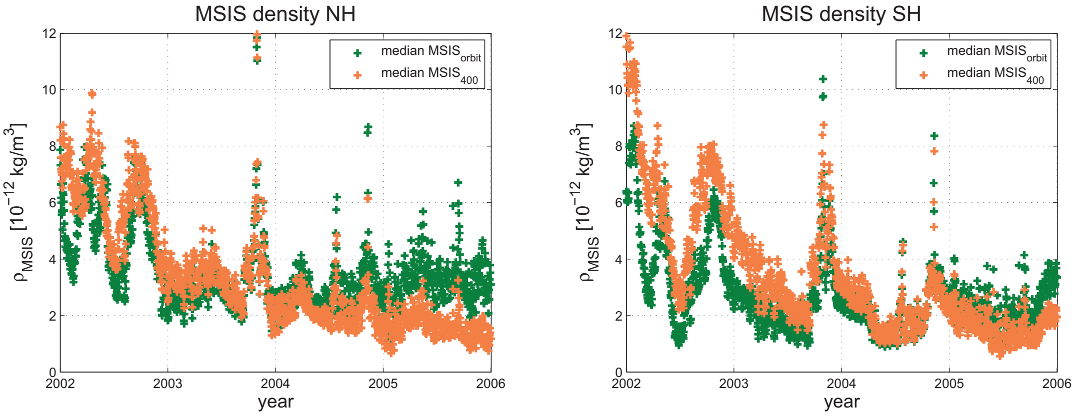

Figure 5.15: Daily median of the MSIS density, as obtained from NRLMSISE-00 for the polar regions ($\geq |55°|$ cgm latitude) during 2002–2005. The density from CHAMP orbital altitudes is displayed in green; the density at a fixed altitude of 400 km is displayed in orange.

An uncertainty is connected to the height normalisation, which is examined in detail and adapted to our intentions here. In brief, it can be said that errors caused by the normalisation are expected to be small, since the CHAMP orbit altitude varies roughly within one scale height ($H \approx 60$ km) in the applied dataset. Liu et al. (2007) quoted an uncertainty of 5%. This is regarded acceptable when comparing a multi-year period where the spacecraft decays by about 65 km. Anyway, it has to be mentioned that the height normalisation procedure depends on the quality and reliability of the applied model values. As it can be seen in the following this impact is worth mentioning but not essential, even though the model is in some cases not capable of reproducing the thermospheric total mass density, especially in polar regions.

Within our four-year period we find a superposition of both effects, decreasing solar flux level and frictional decay of the spacecraft orbit. Hence, the task is to find a representative option, which distorts the measurement results as less as possible but simultaneously complies with the requirement of comparability. While observa-

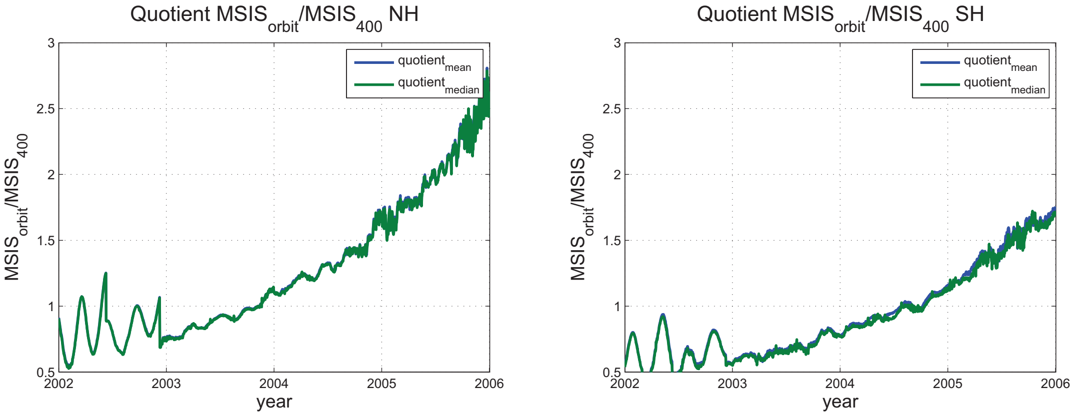

Figure 5.16: Ratio between the thermospheric mass density at orbital altitude and at 400 km altitude as derived from the MSIS model.

tions from orbital altitudes provide accurate (since directly measured) data, height-normalised values justify the one-plot accumulation of data which have been taken at the beginning and at the end of the multi-year period. The height normalisation procedure, as described in Section 4.4.1 depends on the reliability of MSIS.

Considering the distribution of MSIS densities in form of daily medians from orbital altitude data and normed altitude data, respectively (Fig. 5.15), we can see that both of them follow a similar course during the years 2003 and 2004. In 2002, the MSIS density in orbital altitude is smaller than the 400 km-altitude density. Temporary phase shifts can be seen. The difference is more pronounced in the SH. As from the end of 2004 MSIS data from orbital altitude mostly exceed the data from the reference altitude. In this case, the NH difference (≈ factor of 2) is markedly larger than the SH difference (≈ factor of 1.5). Reason for the hemispheric asymmetry is the special orbit configuration. From 2003 onward CHAMP is in a so-called ”frozen orbit” (Roh et al., 2008), offering the lowest possible air drag. This orbit is characterised by a higher altitude over the South pole than over the North pole. Figure 5.16, displaying the corresponding MSIS quotients (MSIS density in orbital altitude divided by MSIS density in 400 km altitude), contains further information. These quotients show large variations only over the course of 2002. They are a consequence of the orbital eccentricity as illustrated in Fig. 5.17. It can be understood as a response to the orbital height correction manoeuvres of the satellite and the corresponding changes. During this time period, the satellite is orbiting above the normed altitude. From the end of 2002 until the end of 2004 the ratio is characterised by a steady increase. In the meantime, it doubles from ≈0.75 (0.6) to ≈1.5 (1.2) for the NH (SH). Later, the quotient is marked by a larger increase (of about 1.1 (0.5) over the course of a year at northern (southern) hemispheric latitudes) and a significantly enhanced small-scale variability. The satellite orbits below the reference height throughout 2005.

The CHAMP track eccentricity should have a direct impact on this distribution, even though it interfers with the height manoeuvre effects in 2002. The eccentricity is small between 2003 and 2005. Therefore, the small-scale variations in 2005 are due to activity variations which transform into changes of the model scale heights.

In the SH, the ratio varies around 1 (four-year mean value: 0.9183), so that hardly any concerns against the height normalisation procedure can be raised for our purposes. A different situation occurs for the NH. The mean value reaches 1.262, in particular due to quotient values >1.5 in 2005. Whilst the height normalisation should not be a problem for 2002 – 2004 it should be kept in mind that the uncertainty due to height normalisation increases in 2005.
With an absolute value of ≈ 2.75 for the quotient this uncertainty, however, will not rank among the main contributions to the error budget.

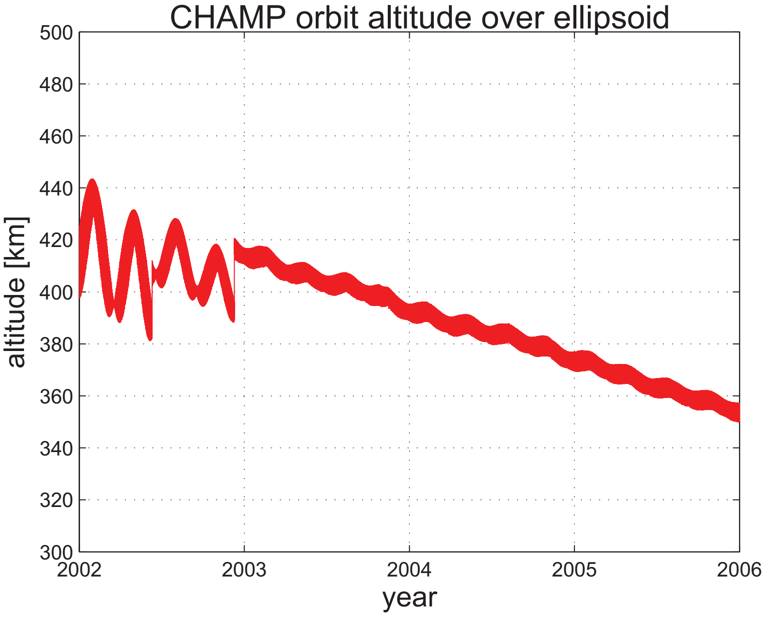

Figure 5.17: Decay of CHAMP orbit altitude during the years 2002 – 2005. A non-uniform decay in 2002 is followed by a constant decay in the other years.

To visualise the influence of the height normalisation we applied our data processing procedure to both datasets, the height-normalised one and the orbital altitude one. Figure 5.18 compares both for our northern hemispheric final result of Section 5.4.2. The $\Delta\rho$ values (upper row) and the $d\rho_{rel}$ values (lower row) are presented with (left column) and without (right column) height normalisation. Interestingly, they do not exhibit significant differences. The presented structures resemble each other very well in both cases. The number and distribution of bins with low $\Delta\rho/d\rho_{rel}$ values match quite well.

A comparison of the quartiles (Table 5.4) unexpectedly reveals a larger range of density amplitudes for the distribution of all values between $Q_{.25}$ and $Q_{.75}$ in case of height-normalised $\Delta\rho$. The quartiles of the relative anomaly remain fairly the same

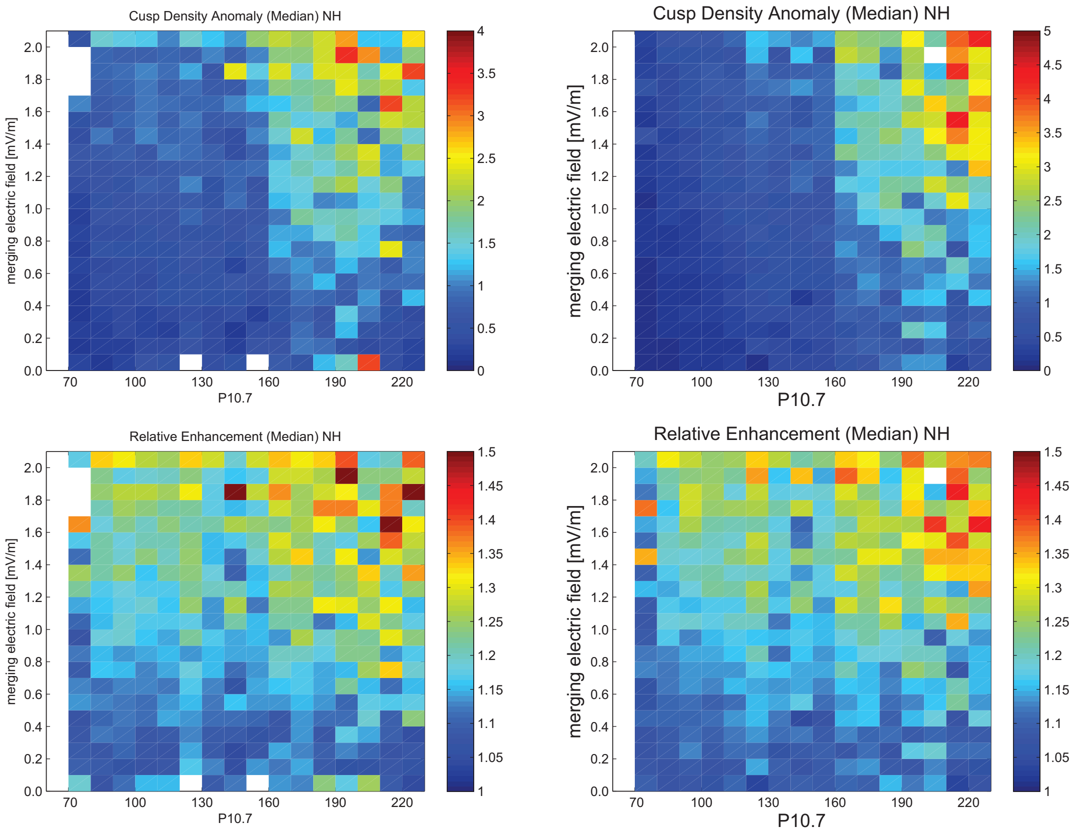

Figure 5.18: Comparison of 2D-correlation distribution. Left column: height-normalised data; right column: orbit altitude data.

for both, height-normalised and orbital altitude data.

We can see in Fig. 5.18 that there is in fact an influence from the height correction with MSIS, larger amplitudes for $\Delta\rho$ are indeed found at orbital altitudes, but maximal $d\rho_{rel}$ amplitudes can be identified in the height-adjusted dataset.

These results prompted us to chose the height-normalised dataset only for the direct comparison of the four-year period, keeping in mind the related artificial effects when interpreting them. A similar data handling in Liu et al. (2005) endorses our behaviour. However, for the investigation of local effects, like the cusp anomaly we preferred to use the data at orbital altitude, e.g. for calculating the 2D-correlation of the controlling parameters.

It has been shown that the influence of the height correction has to be handled critically and carefully. As can be also deduced from Figs. 5.16 and 5.17 the density anomaly values of the later years are obviously scaled up by a factor of 2. Without normalisation the variation of the density is basically reduced - a fact that advocates to use the data from orbital altitudes. The estimation of densities and the height normalisation was roughly applied within one scale height. Errors caused by these

	NH 400 km $[10^{-12} kg/m^3]$	NH orbit $[10^{-12} kg/m^3]$
$\Delta\rho$	$Q_{.25} = 0.47$ $Q_{.75} = 1.57$	$Q_{.25} = 0.52$ $Q_{.75} = 1.30$
$d\rho_{rel}$	$Q_{.25} = 1.12$ $Q_{.75} = 1.24$	$Q_{.25} = 1.13$ $Q_{.75} = 1.24$

Table 5.4: Comparison of quartiles for height-normalised (left) and orbital altitude (right) densities.

procedures are expected to be small (within 5% given a similar uncertainty in the MSIS-predicted scale height) in unperturbed regions. For the presentation of the anomaly dependence on the solar flux level (e.g. Figs. 5.6 and 5.7) we regard it is essential that we perform a height normalisation. Otherwise, the effects of concurrent orbit and solar flux decrease are inseparably interleaved.
For the investigation of the anomaly, however, we use original density readings without normalisation in all the analysis in Section 5.4. The comparison presented here implies that the amplitude of the density anomaly is not strongly depending on altitude. Furthermore, we diminish the influence of the MSIS model in our results.

5.6 Conclusions from the climatology

In this chapter a systematic survey of the thermospheric mass density in the high-latitude dayside thermosphere is presented. Based on four years (2002-2005) of CHAMP air drag measurements climatological properties of the density anomaly could be derived from a statistical study.
The anomaly is rather confined to the ionospheric location of the cusp. For that reason, we relate it primarily to energy input from the magnetosphere. According to model calculations of Demars and Schunk, (2007) a strong air-upwelling, the neutral fountain effect, is associated with the phenomenon. The upwelling air is suggested to diverge at a certain altitude equatorward and poleward. Therefore, we regard the cusp-related anomalies as an important source for the upper thermospheric density distribution on the dayside. This can be confirmed by the wind pattern derived from CHAMP observations in the polar regions and displayed in Fig. 4.6. It clearly shows a wind stagnation point at cusp latitudes which is surrounded by small wind velocities pointing away from the stagnation point, thus indicating a spot of upwelling with following divergence to different directions.
The amplitude of the anomaly depends on many factors. Continuous observations over a sufficiently long period are needed for delineating all the different influences. The controlling parameters we identified are:

- Solar EUV flux: The amplitude of the anomaly depends strongly on the solar flux index P10.7. It seems that for a certain solar flux level, e.g. $P10.7 < 100$, no clear anomalies form anymore.

- Solar wind input: The merging electric field is enhanced for about an hour before the detection of the anomaly. This observed time delay may be explained by two effects, the propagation of the density front from the lower thermosphere to 400 km altitude and the infrequent sampling of the cusp (once per orbit, 93 minutes). The increase in density is proportional to the square of the merging electric field.

- Background thermospheric density: An elevated air density clearly favours the formation of cusp density bulges. This effect is highly correlated with the conclusion above, but the solar flux to density ratio depends on season and hemisphere. We conclude that the ambient air density is the primary factor influencing the anomaly.

- Hemispheric differences: The sensitivity to external forcing is different for the two hemispheres. According to the results in Fig. 5.10 the anomalies in the northern hemisphere are larger by a factor of 1.6 than in the South for the same E_{merg} and P10.7 inputs. We consider this to be partly due to the larger offset between geographic and geomagnetic poles in the South.

- Solar zenith angle: Only a weak dependence of the anomalies on the solar zenith angle could be detected. This observed impact might even be biased by the correlation between the SZA and the ambient density. We may therefore conclude that the SZA-related change in ionospheric conductivity does not play an important role in the anomaly formation.

These characteristics and dependences can be regarded as important constraints for the modelling of the cusp anomaly, and they will help to identify the processes responsible for the local air-upwelling.

Chapter 6

CHAMP-EISCAT campaign

The cusp-related density anomaly developes due to denser air from lower levels that is upwelling and causing a density enhancement at higher altitudes.

However, the causes of air-upwelling are not clear yet.

The CHAMP satellite data alone cannot answer this question, since vertical processes have to be taken into account as well. That is why further methods have to be examined to incorporate vertical processes. They are introduced together with Joule heating influences.

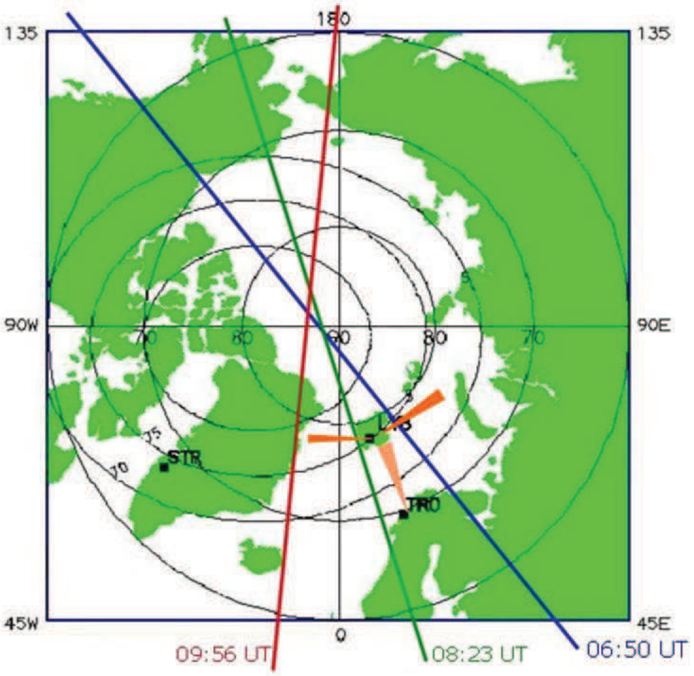

Figure 6.1: Synoptic view of the CHAMP-EISCAT campaign setting on 13 October 2006, involving the CHAMP spacecraft (three overflights), the field-aligned ESR 42m and the steerable ESR 32m antennas on Svalbard, and the Tromsø VHF facility.

As we know, CHAMP is a versatile device which can be used to investigate the thermospheric parameters at orbit altitudes. In some cases, however, it is necessary to know the conditions above and below the orbit track, especially when vertical dynamics plays a role. This is in particular true for the cusp region where upwelling air from lower levels is supposed to modify the thermospheric density distribution. Here, ground-based measurements, such as Incoherent Scatter Radar (ISR) observations are promising tools.
In the following subsections, we will dwell on our combined CHAMP-EISCAT campaign. The aim of the campaign, which resembles the SIRCUS campaign (Watermann, 2003; Schlegel et al., 2005), was to observe neutral thermospheric characteristics and ionospheric parameters simultaneously in the vicinity of the cusp.

6.1 Strategy, experiment, background

Using the radar technique is one of the most efficient ways to gain information about the state and dynamics of the atmospheric layers between the ground and the satellite. In this section, a survey about the EISCAT facilities will be followed by an outline of the experiments and the theoretical background of the campaign.

6.1.1 EISCAT facilities

The support of scientific projects with high-tech ISR facilities was made prime business of the EISCAT scientific association. In 1981, the tristatic UHF facility (Tromsø, Kiruna, Sodankylä) was commissioned, followed by the Tromsø VHF radar in 1985. The EISCAT Svalbard Radar (ESR), Longyearbyen, was inaugurated in 1996 (ESR 32m) and completed in 2000 (ESR 42m). Also in 2000, the mainland radars were renovated extensively. The ambitious EISCAT 3D-project is scheduled for the future.

Tristatic UHF System

The transmitter and one receiver of the UHF radar are located near Tromsø in northern Norway, the two other receivers are situated in Kiruna / Sweden and Sodankylä / Finland. The centre operation frequency of the transmitter amounts to 928.4 MHz. With a peak power of 2 MW the transmitter facility is powerful enough to receive utilisable backscatter signals from the ionospheric plasma. The three parabolic dishes of the tristatic system have a diameter of 32 m and are fully steerable to cover a large area above Northern Scandinavia. Its major task is to explore the auroral ionospheric dynamics since the ion drift velocity components can be estimated in three dimensions in the common volume of the three radar beams.

Monostatic VHF system

The monostatic VHF radar is also loacted near Tromsø (69° 35' 11" N, 19° 13' 38" E). It is composed of four parallel cylindric segments of $(30 \times 40)\, m^2$ in size, which are slewable in the magnetic meridian plane. Due to the enormous size, a peak power of 2 × 1.5 MW, and a transmission centre frequency of 224 MHz, it is possible to derive long-distance signals, e.g. echoes from range gates more than 1000 km away, for example, echoes from the Svalbard ionosphere at low elevation - like we examined in our experiment.

ESR

The two facilities on the Spitsbergen archipelago (78° 09' 11" N, 16° 01' 44" E) are sometimes called the EISCAT masterpiece (Tony van Eyken, personal communication, 2006). With a transmission centre frequency of 500 MHz and a peak power of 1 MW the two parabolic dishes (diameters 32 m and 42 m, respectively) resemble the power of the mainland UHF facilities. The ESR 32m antenna is fully steerable. The ESR 42m measures along the magnetic field line which runs across the radar station.

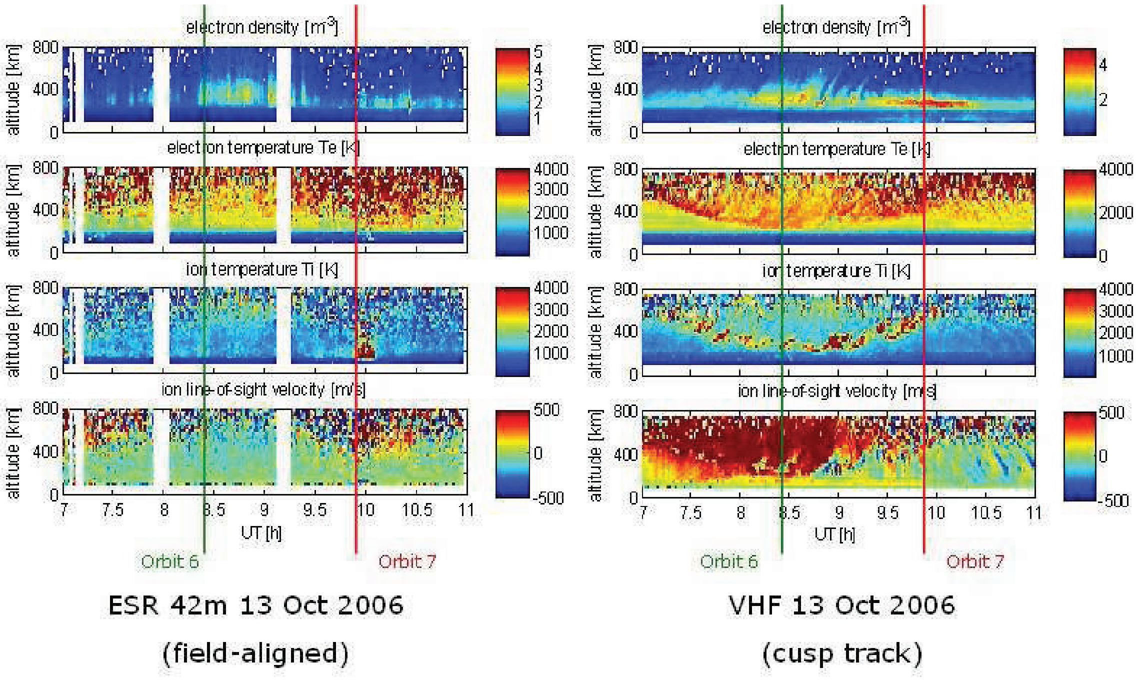

ESR 42m 13 Oct 2006
(field-aligned)

VHF 13 Oct 2006
(cusp track)

Figure 6.2: Ionospheric parameters (electron density, electron temperature, ion temperature and ion line-of-sight velocity (positive means away from the radar)) on 13 October 2006, observed by the ESR 42m antenna (left) and the Tromsø VHF radar (right). The enhanced electron density is regarded as a cusp feature. The vertical lines indicate CHAMP overpasses.

6.1.2 ISR techniques (overview)

The ISR principle ranks among the most important and powerful ground-based ionospheric measurement techniques.

Indeed, the operating expenses are immense (powerful transmitter, large-size receiver antennas) but it countervails the outstanding advantage to measure several ionospheric parameters (first of all electron density, electron temperature, ion temperature, and ion drift velocity), simultaneously. The technique was introduced by Gordon and first executed by Bowles in 1958 (Gordon, 1958; Bowles, 1958). It is based on the principle of Thomson scattering: the transmitted radar beam is scattered by the free electrons of the ionospheric plasma. The backscattered waves add incoherently.

It is necessary to transmit strongly bundled high frequency pulses at a high transmitting power and operate large-area receiver antennas to recover a weak backscatter signal, that is sufficiently strong to support utilisable analyses. Thereof it is possible to derive electron parameters. Enhancing the scale length by choosing a longer radar wave length, which is much larger than the Debye-length, plasma oscillations are observed instead of free (single) electrons since the electrons are coupled to the plasma oscillation wave field in this range. On the one hand, such oscillations are caused by electrons in the range of the electron plasma frequency and electron gyrofrequency, but these signals can also be modified by iono-acoustic waves on the other hand. Therefore, we can also derive the ion characteristics from the radar data.

The typical IS spectrum displays two maxima in the vicinity of the Doppler-shifted frequency, which just corresponds to the ion's thermal velocity. The plasma drift velocity instead causes a Doppler shift of the whole spectrum by a certain frequency. The ion temperature determines the width of the spectrum, and the amplitude of its maxima is defined by the electron temperature (Kelley, 1989). Electron density and ion drift velocity can be determined from the spectrum with the help of a nonlinear regression analysis. The ion mass is known if we act on the assumption that a well-known ion population dominates in a given altitude range. For instance, O^+ ($m_i = 16\,amu$) is dominating at 250-500 km altitude (Prölss, 2001).

For cleaning the data, careful data processing is necessary before calculating ionospheric characteristics, i.e. the noise has to be removed from the spectrum. This can be realised by subtraction of the particular spectrum which is observed by the receiver without transmitting activity. Apart from that, the spectrum has to be corrected for the transmission pulse characteristics as well as for the receiver frequency properties. Disturbing echoes from airplanes, satellites, moon and Sun are also eliminated. This processing is automatically done by the EISCAT analysis software in near-realtime. The ionospheric parameters are presented (e. g. in Fig. 6.2) in a form that is based on the EISCAT analysis software GUISDAP (Grand Unified Incoherent Scatter Data Analysis Program; Lehtinen and Huuskonen, 1996).

6.1.3 Campaign schedule

Distributed over nine experiment days, the following measurements were run during 1–13 October 2006.
Our aim was the simultaneous observation of thermospheric (CHAMP) and ionospheric (EISCAT) parameters in the dayside cusp environmental atmosphere.

CHAMP crossed the radar stations at least once per operation time in less than 11° longitudinal distance providing neutral air mass density values.

Date	Time (UT)	Facilities	Closest CHAMP pass		Comments
01/10/2006	0700 - 1100 0700 - 1100	ESR Tromsø UHF	0910 UT	10.750°E	West of ESR UHF due to probl. with VHF
02/10/2006	-	-			no observation
03/10/2006	0700 - 1100	ESR, VHF	0832 UT	17.592°E	East of ESR
04/10/2006	0830 - 1100 0850 - 0900 0700 - 1100	ESR42m ESR32m VHF	0858 UT	09.514°E	West of ESR
05/10/2006	-	-			no observation
06/10/2006	0700 - 0900 0700 - 1100	ESR VHF	0820 UT	16.370°E	over ESR
07/10/2006	0700 - 1100	ESR, VHF	0847 UT	08.299°E	West of ESR
08/10/2006	-	-			no observation
09/10/2006	0700 - 1100	ESR, VHF	0808 UT	15.168°E	West of ESR
10/10/2006	0700 - 1100	ESR, VHF	0835 UT	07.104°E	West of ESR
11/10/2006	-	-			no observation
12/10/2006	0700 - 1100	ESR, VHF	0757 UT	13.988°E	West of ESR
13/10/2006	0700 - 1100	ESR, VHF	0823 UT	05.931°E	West of ESR

Table 6.1: CHAMP EISCAT campaign: characteristics of the campaign days 1-13 October 2006.

The ESR 42m antenna measured the ionospheric parameters along the magnetic field line while the ESR 32m and the VHF radar were used to track the cusp, which was expected to cross the radar volume from East to West during the operational hours. That is why the ESR 32m antenna was first directed eastward with an elevation of 60°. After one hour its direction was switched towards West and the elevation was lowered to 30°. In the meantime, the VHF facility was pointing northward at low elevation (30°) to chart the ionospheric volume south of Svalbard and to support the Svalbard radar observing cusp features.
Whilst CHAMP provided a complete dataset we had to cope with some data gaps in the ISR data: For instance, the VHF antenna was inoperable on the first experiment day. Alternatively, the Tromsø UHF antenna was operated, whose radar beam was of course not reaching as far northward as the VHF radar beam. On 4 October 2006 and 6 October 2006 our measurements coincided with a SPEAR/EISCAT campaign of the University of Leicester (Yeoman et al., 2008). Therefore, the radars were not recording during the whole scheduled operation time.

Apart from that, the ESR measurements were interrupted temporarily due to required reboots, and, more often, due to airport interlocks. On the Svalbard airport,

campaign day	F10.7	P10.7	Dst	Ap	Kp
01/10/2006	78.6	77.8	-32.2	22.9	3+
03/10/2006	76.7	77.9	- 9.2	6.0	2−
04/10/2006	76.7	77.4	- 8.8	3.6	1−
06/10/2006	76.3	77.8	- 0.9	2.1	0+
07/10/2006	76.4	77.4	3.6	10.3	2−
09/10/2006	74.8	77.0	- 4.8	4.4	1_0
10/10/2006	75.0	76.9	- 0.7	2.3	0+
12/10/2006	73.3	76.2	- 1.8	5.0	1+
13/10/2006	**72.9**	**76.1**	**-25.1**	**29.4**	**4−**

Table 6.2: CHAMP EISCAT campaign: Solar and geomagnetic activity levels during the campaign hours. The last day was preferably used for the analysis.

Longyearbyen, the communication between an airplane crew and the tower is realised via radio wave frequencies. Therefore, the operation of the nearby EISCAT facilities is intermitted for security reasons during take-off/landing manoeuvres. These unavoidable interruptions of usually few minutes are short enough not to spoil the general aim of the experiment.
As can be seen from Table 6.2 only our last campaign day shows moderate geomagnetic activity. The other days (except for the first day) can be classified as very quiet.

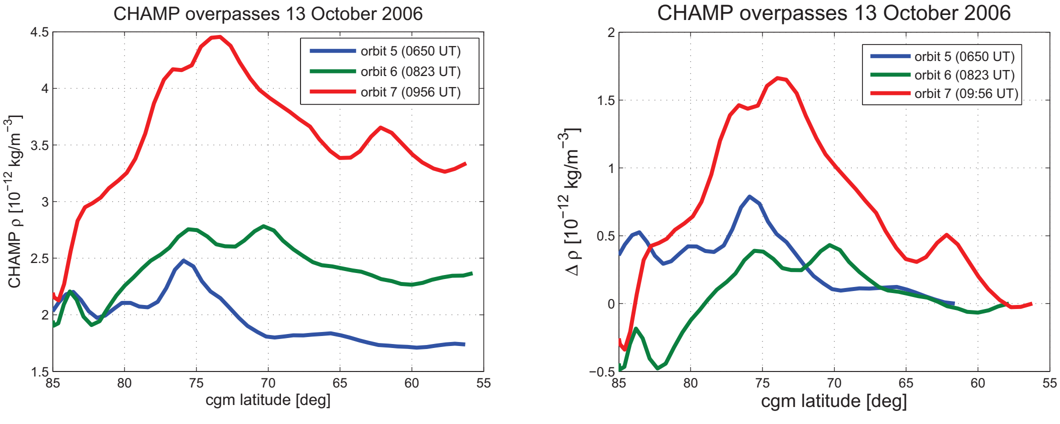

Figure 6.3: CHAMP-observed density (left) and density anomaly $\Delta\rho$ (right) along three passes over the EISCAT facilities on 13 October 2006. The enhancement in the vicinity of the cusp is most prominent during the latest overpass.

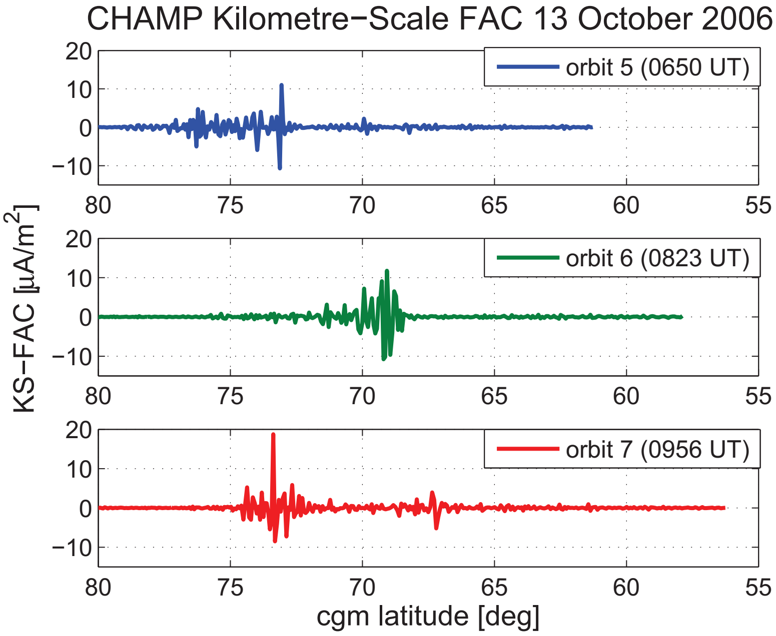

Figure 6.4: Kilometre-scale FACs as observed with CHAMP during the three overflights of 13 October 2006.

6.2 CHAMP observations

The CHAMP-observed density and the thereof derived density anomaly are displayed in Fig. 6.3 to represent the neutral component of our campaign results. It shows the density distribution along the CHAMP track during the three dayside passes over the EISCAT facilities on 13 October 2006.

During the earliest overflight (0650 UT) both quantities do not reveal any significant enhancement at cusp latitudes. In the second overflight (0823 UT) the density at cusp latitudes differs only marginally from the other parts. The third overflight (0956 UT) displays a generally enhanced density/density anomaly compared to the two previous overflights.
We can detect a marked density maximum/density anomaly maximum at 73.3°. Hence, thermospheric density anomaly features can indeed be identified on this campaign day, even though they are less pronounced than we would expect for high solar and magnetic activity conditions. Nonetheless, this campaign day is regarded as a suitable day (out of our repertoire of CHAMP-EISCAT-cusp conjunction measurements) to investigate the amount of Joule heating.

In addition, the CHAMP-observed (kilometre-scale) KS-FACs (Rother et al., 2007) are displayed for the three overpasses in Fig. 6.4. Their behaviour is comparable to that of the density anomaly: The peak amplitudes are restricted to 67°–76° cgm latitude, i.e. to the vicinity of the cusp (where largest density anomalies occur). The FAC amplitudes reach up to $\approx |11|$ μA/m^2 during the first and second overflight, but 18 μA/m^2 during the latest overflight. Maximal values occur > 70 ° cgm latitude during the earliest overflight and most equatorward during the second overflight. They move back towards the pole for the latest overflight.

6.3 Derivation of Hall, Pedersen, and Birkeland conductivity

Based on the local form of Ohm's law, $\vec{\jmath} = \sigma \cdot \vec{E}$, with $\vec{\jmath}$ being the current density, $\vec{E}$ the electric field and σ being the conductivity tensor for vertical field lines at the NH:

$$\begin{pmatrix} \sigma_P & \sigma_H & 0 \\ -\sigma_H & \sigma_P & 0 \\ 0 & 0 & \sigma_{||} \end{pmatrix}$$

and based on the energy balance equation for charged particles, (Eq. (D.2)), Hall (σ_H) and Pedersen (σ_P) conductivities can be estimated to

$$\sigma_H = \frac{en}{B} \left\{ \frac{\omega_{eB}^2}{\left(\omega_{eB}^2 + \nu_{e,n}^2\right)} - \frac{\omega_{iB}^2}{\left(\omega_{iB}^2 + \nu_{i,n}^2\right)} \right\}, \tag{6.1}$$

$$\sigma_P = \frac{en}{B} \left\{ \frac{\nu_{e,n}\omega_{eB}}{\left(\omega_{eB}^2 + \nu_{e,n}^2\right)} + \frac{\nu_{i,n}\omega_{iB}}{\left(\omega_{iB}^2 + \nu_{i,n}^2\right)} \right\}, \tag{6.2}$$

and the Birkeland (parallel) conductivity, $\sigma_{||}$,

$$\sigma_{||} = \frac{en}{E_{||}} \left(\frac{eE_{||}}{m_i \nu_{i,n}} + \frac{eE_{||}}{m_e \nu_{e,n}} \right) = e^2 n \left(\frac{1}{m_i \nu_{i,n}} + \frac{1}{m_e \nu_{e,n}} \right). \tag{6.3}$$

Here, e is the elementary charge, n is the particle density, B is the total intensity of the magnetic field, and $E_{||}$ is the parallel component of the electric field. A detailed derivation of the conductivities is given in Appendix D, following the interpretation of Prölss (2001).

To calculate the gyro-frequencies, ω_{eB} and ω_{iB}, we take into account an electron mass of $m_e = 9.109390 \times 10^{-31}\,kg$, and an ion mass of $m_i = 30.7\,amu$:

$$\omega_{eB} = \frac{|-e|\,B}{m_e}; \tag{6.4}$$

$$\omega_{iB} \quad = \quad \frac{eB}{m_i} \tag{6.5}$$

For the collision frequencies, $\nu_{e,n}$ and $\nu_{i,n}$, Schunk and Nagy (1978) and Schunk and Walker (1973) determined:

$$\begin{aligned} \nu_{e,n} \;= &\quad 2.33 \cdot 10^{-11}\, n_{N_2} \Big(1 - 1.21 \cdot 10^{-4}\, T_e\Big) \cdot T_e \\ + &\quad 1.82 \cdot 10^{-10}\, n_{O_2} \Big(1 + 3.6 \cdot 10^{-2} \sqrt{T_e}\Big) \cdot \sqrt{T_e} \\ + &\quad 8.9 \cdot 10^{-11}\, n_O \Big(1 + 5.7 \cdot 10^{-4}\, T_e\Big) \cdot \sqrt{T_e}, \end{aligned} \tag{6.6}$$

$$\nu_{i,n} \;=\; 4.34 \cdot 10^{-10}\, n_{N_2} + 4.28 \cdot 10^{-10}\, n_{O_2} + 2.44 \cdot 10^{-10}\, n_O, \tag{6.7}$$

with T_e being the electron temperature, and n_{N2}, n_{O2}, n_O being the number densities of the different species.

6.3.1 Derivation of Hall and Pedersen conductivities with the help of EISCAT

The derivation of Hall and Pedersen conductivities follows the interpretation of Schlegel et al. (1988). From the EISCAT measurements we obtained the following listing of parameters for every facility and observation:

- the altitude $[h] = km$,
- the universal time $[UT] = min$,
- the electron density $[n_e] = log10m^{-3}$,
- the electron temperature $[T_e] = K$, and the ion temperature $[T_i] = K$,
- the line-of-sight velocity $[v_{los}] = m/s$ (where positive means away from the radar).

As a first step we smoothed T_e by applying a 6th degree polynomial. This was necessary to receive utilisable results since the small-scale variation of T_e can be very extensive for some observations.

From the MSIS model data we derived the densities of the neutral gas species. MSIS provides the number density of:

- molecular oxygen $[n_{O_2}] = cm^{-3}$,
- molecular nitrogen $[n_{N_2}] = cm^{-3}$,
- atomic oxygen $[n_O] = cm^{-3}$,

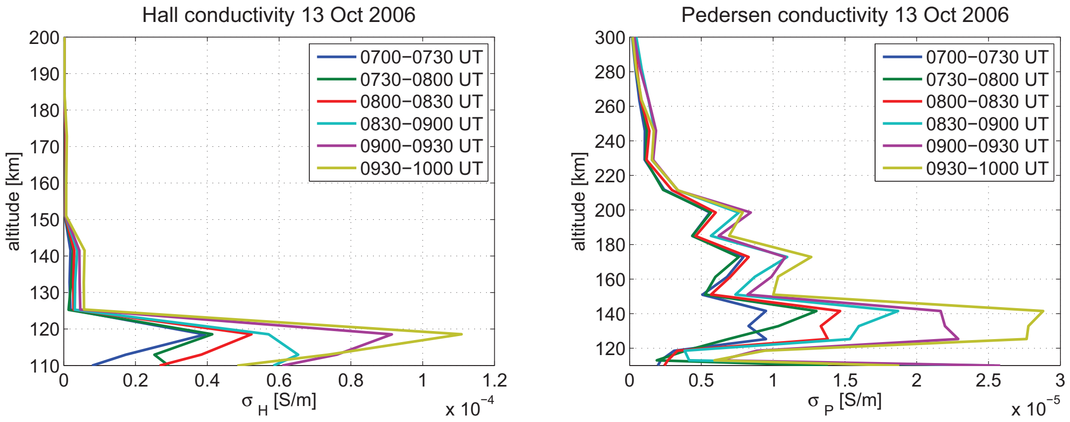

Figure 6.5: Altitude profiles of Hall conductivity (left panel) and Pedersen conductivity (right panel) for different times of the observation period on 13 October 2006.

for altitude steps of 20 km in the range 0–800 km and for time steps of 15 min in the range 0645–1100 UT. These values can be downloaded via http://nssdc.gsfc.nasa.gov/space/model/models/msis.html.

Since we also need information about the ambient magnetic field, we used the IGRF homepage (http://www.geomag.bgs.ac.uk/gifs/igrf_form.shtml) to derive the

- declination,
- inclination
- horizontal intensity $[B_h] = nT$,
- vertical intensity $[B_v] = nT$,
- North component $[B_N] = nT$,
- East component $[B_E] = nT$,
- total intensity $[B_{tot}] = T$,

for the particular campaign day and the locations of the operating EISCAT facility.

With these data we compiled height profiles of σ_P and σ_H for every 15 minute time interval, using Eq. (D.4), Eq. (D.5) with the ω_{eB}, ω_{iB} estimates (Eq. (6.4), Eq. (6.5)) and the collision frequency estimates of Schunk and Nagy (1978), and Schunk and Walker (1973), Eq. (6.6), Eq. (6.7).

Figure 6.5 presents these height profiles for the observations of the campaign day 13 (13 October 2006). They peak at about 120 km (σ_H) and 140 km (σ_P). These values have to be height-integrated. Therefore, we obtained median values of them and summed the medians between 0 and 450 km of altitude. Then, we multiplied the results with the height step increment of 20 km. As results we obtain the

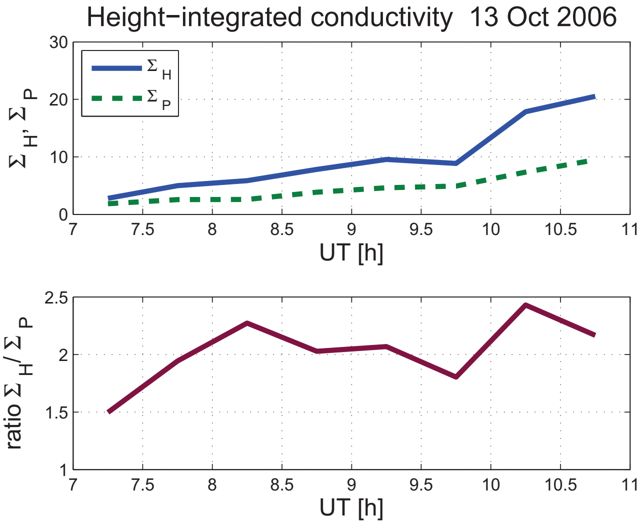

Figure 6.6: Height-integrated conductivities (conductances) in S and their ratio during 13 October 2006 observation hours.

height-integrated conductivities Σ_H, Σ_P, and the ratio Σ_H/Σ_P, which are displayed in Fig. 6.6. Both are increasing with time, but as revealed by the ratio, the Hall conductance increase is stronger than that of the Pedersen conductance.
EISCAT observations come along with an average uncertainty of 7.96% for the electron density, and 16.20% for the electron temperature. Since we have to take care of these uncertainties in the derivation of the $e\,n/B$ term and the neutral–electron collision frequency we have to expect a comparable error for the conductivities.

6.3.2 Calculation of Joule heating parameters with CHAMP-observed currents and EISCAT data

Frictional heating of neutral gas (Joule heating) occurs when charged particles, driven by an electric field or other forces, collide with neutral gas particles. In the ionosphere, this process is most effective for an electric field perpendicular to the neutral gas flow. Due to the collisions, directional motion is converted to random motion and heating. This nondirectional motion in turn causes further collisions and therefore more heat. The corresponding heating rates of the neutral gas and the ion gas are approximately of the same amount since the masses of both species do not differ much. As outlined in Section 2.1, the heating rate can be described by the vector sum of the externally applied electric (convective) field from the magnetosphere and the neutral wind dynamo.
According to Eq. (2.1) Joule heating can be expressed as:

$$\begin{aligned} q(h) \;=\; \sigma_P E^2 \quad &= \quad \frac{1}{\sigma_{||}^2} j_{||}^2 + \sigma_P \left(\frac{J_H}{\Sigma_H} + \frac{J_p}{\Sigma_P} \right)^2 \\ &= \quad \sigma_P \left(E_{DC} + E_{AC} \right)^2 , \end{aligned} \tag{6.8}$$

or

$$Q \;=\; \Sigma_P \left(E_{DC} + E_{AC}\right)^2 , \tag{6.9}$$

with $\sigma_{||}$ being the parallel conductivity, σ_P being the Pedersen conductivity, $E_{||}$ and $E_{\perp}$ being the parallel and perpendicular components of the electric field, E_{DC} being the slowly varying (large-scale) component of the electric field, E_{AC} being the fast varying (small-scale) component of the electric field, J_H and J_P being the Hall and Pedersen sheet current densities, and finally, Σ_H and Σ_P being the (height-integrated) Hall and Pedersen conductances. Since the parallel conductivity, $\sigma_{||}$, becomes quite large in the altitude range of interest, the $\sigma_{||}$ term vanishes.
Equation (6.8) yields the height-dependent Joule heating rate, $q(h)$, in W/m^3. To derive the integrated Joule heating rate per area, Q, Eq. (6.9) is applied.

The influence of the perpendicular electric field is separated into a large-scale part (E_{DC}) and a small-scale part (E_{AC}). Then, the idea is to derive E_{DC} from CHAMP Hall current observations and E_{AC} from magnetic field fluctuations using the Alfvén relations.

6.3.3 Estimation of the E_{DC} component

The large-scale component, E_{DC}, is supposed to correspond to the slowly varying contribution. Our approach is to derive it from CHAMP magnetometer readings.

The magnetometers onboard CHAMP record contributions from ionospheric Hall, Pedersen and field-aligned currents. Ritter et al. (2004 a,b) reported on a method to separate these influences and extract Hall currents and FACs from the measurements: From the total magnetic field recordings, which are not influenced by FACs, horizontal ionospheric currents can be estimated. The vector magnetic field data are used to derive FACs. Pedersen currents are diverted into FACs at high latitudes. Therefore, they produce mainly transverse magnetic fields, so that the measured contributions to the total magnetic field originate primarily from the source-free Hall currents. The reliability of ionospheric current estimates from CHAMP magnetic field measurements has been checked and validated against ground-based observations (Ritter et al., 2004 a,b).

The FACs have been calculated separately for every orbit applying the Ampère-Maxwell-Law: $\vec{\nabla} \times \vec{B} \;=\; \mu_0 \vec{\jmath}$, assuming the FACs to be qualitatively perpendicular to the satellite path. This procedure yields the Hall current density profiles along the CHAMP orbit.

We calculated E_{DC} (along the orbit track) from the Hall current estimates. Both, the currents and the E_{DC} results are displayed in Fig. 6.7, again for the campaign day 13. Both of them peak at around 75° mlat, but the amplitudes are larger on

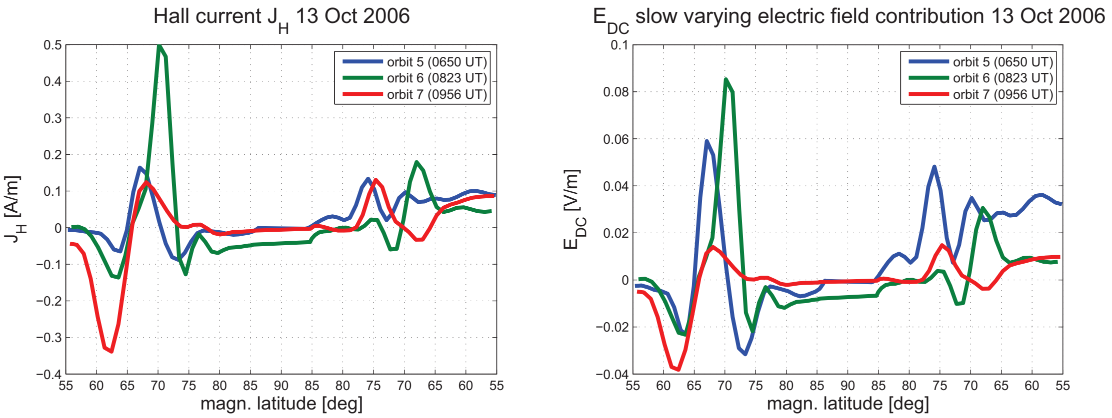

Figure 6.7: Hall currents (left panel) and thereof derived E_{DC} components of the perpendicular electric field during three CHAMP overflights on 13 October 2006. We are only interested in the dayside (right) part of the panel, which is displayed in Fig. 6.11 again.

the nightside (left part of the spectrum). The second overflight was closest to the radar station.

6.3.4 Estimation of the E_{AC} component

Ishii et al. (1992) used DE-2 satellite data to determine the ratio between the perpendicular electric field and the magnetic field variations at high latitudes when the spacecraft crossed the FAC sheets. The variations were interpreted as static spatial variations.

For large scales ($>$ 150 km, resp. 20 seconds) the ratio between the magnetic variation ΔB and the orthogonal electric field component was found to reflect the height-integrated Pedersen conductivity, Σ_P. For short-period fluctuations ($<$ 10 seconds) the ratio $E/\Delta B$ approached the inverse of the Alfvén velocity, v_A. The place where a plasma tube constricts itself and its magnetic field is characterised by an increase of B and of the magnetic pressure p_m. This pressure undertakes the role which is played by the gas-kinetic pressure in a sound wave. Along the B field lines the Alfvén waves disperse with the so called Alfvén velocity, v_A:

$$v_A = \sqrt{\frac{p_m}{n_{e_i}}} = \sqrt{\frac{B^2}{\mu_0 \rho_{e_i}}}, \tag{6.10}$$

where μ_0 is the permeability constant ($\mu_0 = 1.25664 \times 10^{-6}\, sVm^{-1}A^{-1}$) and ρ_{e_i} is the density of charged particles: $\rho_{e_i} = \bar{m}_i n_e = m_{O^+} n_{O^+} + m_{H^+} n_{H^+}$ in the thermosphere. From the IRI model we know that the second term is negligible for

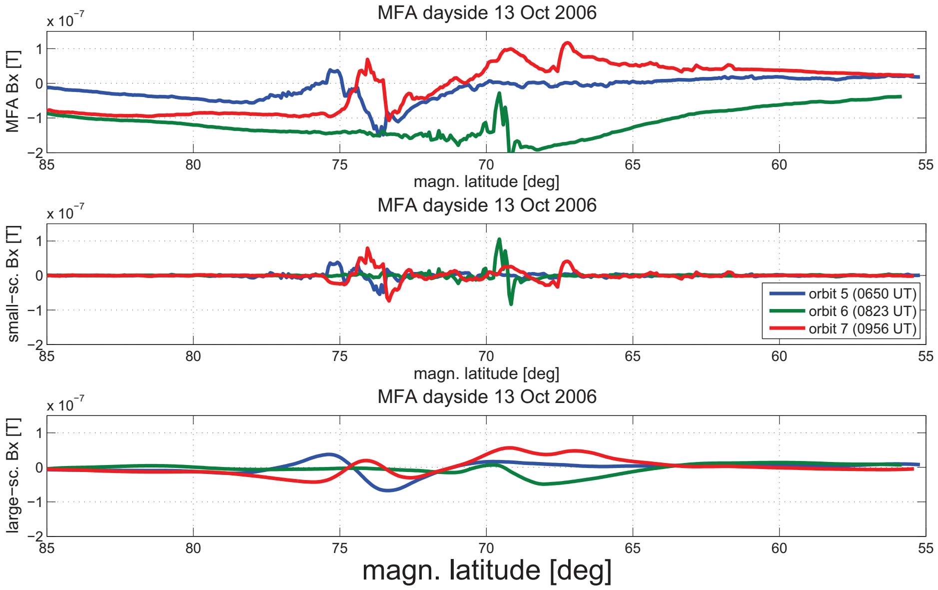

Figure 6.8: Top panel: MFA B_x components as derived from POMME 3 model on 13 October 2006. Central panel: small-scale MFA B_x components. Bottom panel: large-scale MFA B_x components. Only the dayside situation is displayed. Largest variability occurs during the latest overflight.

altitudes < 600 km. Therefore, we only take into account the number density, n_{O^+}, and the ion mass, m_{O^+}, of atomic oxygen ions. The latter amounts to $\approx 16\,amu$. The n_{O^+} value was taken from IRI.

Ishii et al. (1992) revealed that this behaviour is particular distinct on the dayside. This region coincides with our observations of density enhancements. The result motivated us to derive an estimate for the small-scale electric field, E_{AC}, from the fluctuations of the transverse magnetic field:

$$E_{AC} = \Delta B v_A = \frac{\sqrt{\Delta B_x^2 + \Delta B_y^2}\,|B|}{\sqrt{\mu_0 \rho_{O+}}}, \tag{6.11}$$

For this purpose we need to know the perpendicular components, B_x and B_y, in the Mean Field Aligned (MFA) system. They are provided by the magnetic field measurements of CHAMP rotated into the local magnetic field direction, as predicted by the model POMME 3 (Maus et al, 2005) and highpass-filtered at 20 seconds, since we are interested in the small-scale variations.

The corresponding electric field, E_{AC}, is derived using Eq. (6.11), and a 40 second running mean is applied on ${E_{AC}}^2$ for smoothing the curves. For an overview, the obtained electric field is shown in Fig. 6.10.

For completeness, Fig. 6.8 presents the behaviour of the MFA B_x component versus

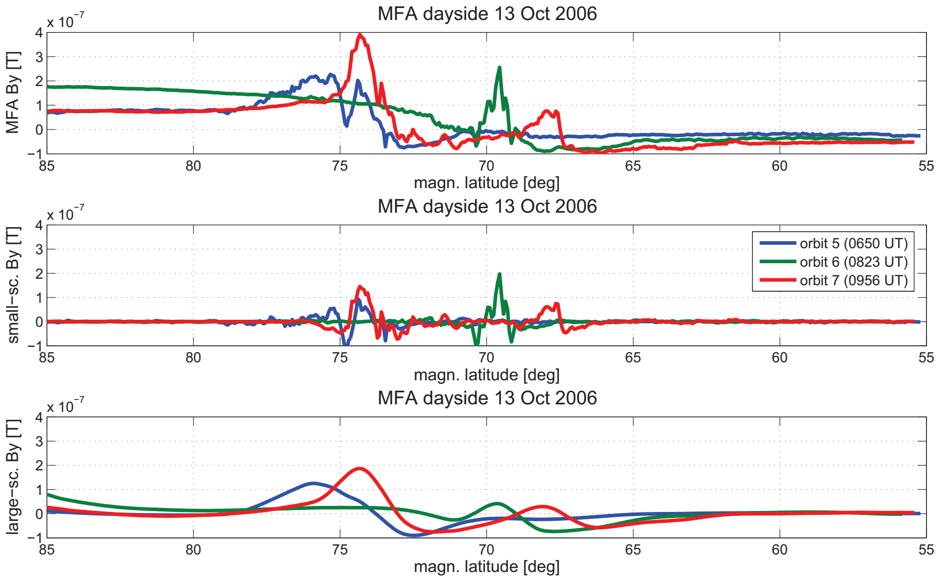

Figure 6.9: Same format as Fig. 6.8, but for the MFA B_y component. Top panel: MFA B_y components as derived from POMME 3 model on 13 October 2006. Central panel: small-scale MFA B_y components. Bottom panel: large-scale MFA B_y components.

cgm latitudes of the dayside northern polar region. The uppermost panel displays the total of B_x data, the middle one the highpass-filtered small-scale component, and the large-scale component can be seen in the lowermost panel. Certain activity occurs between 67° and 76° cgm latitude, starting at highest latitudes with the earliest overflight and then moving towards lower latitudes with time. This activity comes from the small-scale component. The large-scale component, however, shows only smooth variations.

A similar behaviour can be observed in Fig. 6.9 where the same situation is displayed for the MFA B_y component. Like for B_x the highest activity is due to the small-scale component, appearing most poleward during the earliest overflight and most equatorward during the second overflight.
The E_{AC} distribution in the dayside polar region is presented in Fig. 6.10. Each overflight shows a peak of E_{AC} equatorward of the magnetospheric cusp. Interestingly, this peak is most poleward (74.9° cgm latitude) during the earliest overflight (orbit 5), then appears more equatorward at 69.9° cgm latitude about 90 minutes later, and then moves back towards the pole, reaching its maximum (45 mV/m) during the latest overflight (orbit 7; 73.5° cgm latitude). This matches the behaviour of the KS-FACs. Orbit 7 might reveal a double-hump structure, but the number of data points is too poor to regard this as an unambiguous feature. As a consequence of the rather low number of datapoints the variance is quite large. However, the mean error of the average amounts to 0.6 mV/m (orbit 5), 0.8 mV/m (orbit 6), 0.5 mV/m (orbit 7).

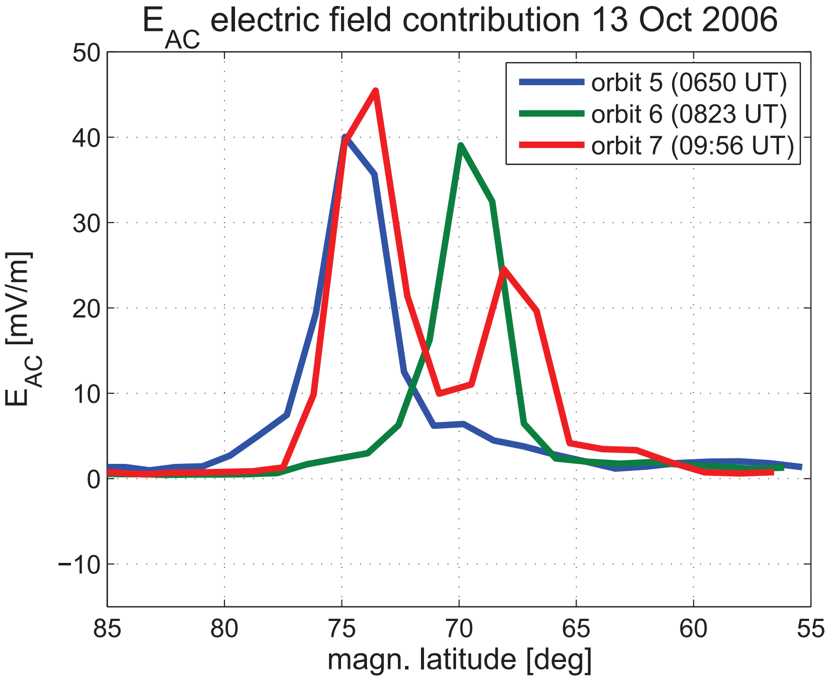

Figure 6.10: E_{AC} contribution, as estimated from the Alfvén approach on 13 October 2006.

Compared to the E_{DC} component (cf. Fig. 6.11), E_{AC} reveals both a resembling behaviour (activity of comparable amplitude during the first and second overflight in the vicinity of the cusp; peaks at about the same latitude most poleward in the earliest and most equatorward in the second overpass) and clear differences: The amplitude is smaller by a factor of ~ 3 for the E_{DC} component of the latest overflight. Oppositely to E_{AC} the amplitude is hardly declining when approaching lower latitudes. The E_{DC} contribution is larger equatorward than poleward of the cusp region. It can also have a negative value dependent on the direction of the Hall current. We have to deal with a mean error of 2.5 mV/m (orbit 5 and 6) and 1.4 mV/m (orbit 7).

6.4 Joule heating rates

Taking into account the results of E_{DC} and E_{AC}, estimates of Joule heating rates have been derived for the example day. They are presented in Fig. 6.12.

Since we apply the same dataset, the shape of the Joule heating rate curves is the same in both panels.
The left panel displays the Joule heating rate per volume, as derived from Eq. (6.8). This quantity is height-dependent. For the presentation, we only used σ_P at 140 km, since highest conductivities are obtained from this altitude (cf. Fig. 6.5).
While the heating rates reach up to about 5.7×10^{-8} W/m^3 (5.0×10^{-8} W/m^3) during the first (second) overflight they become almost twice as large during the latest overflight. We have to accept large mean errors of 2.0×10^{-8} W/m^3 (orbit 5),

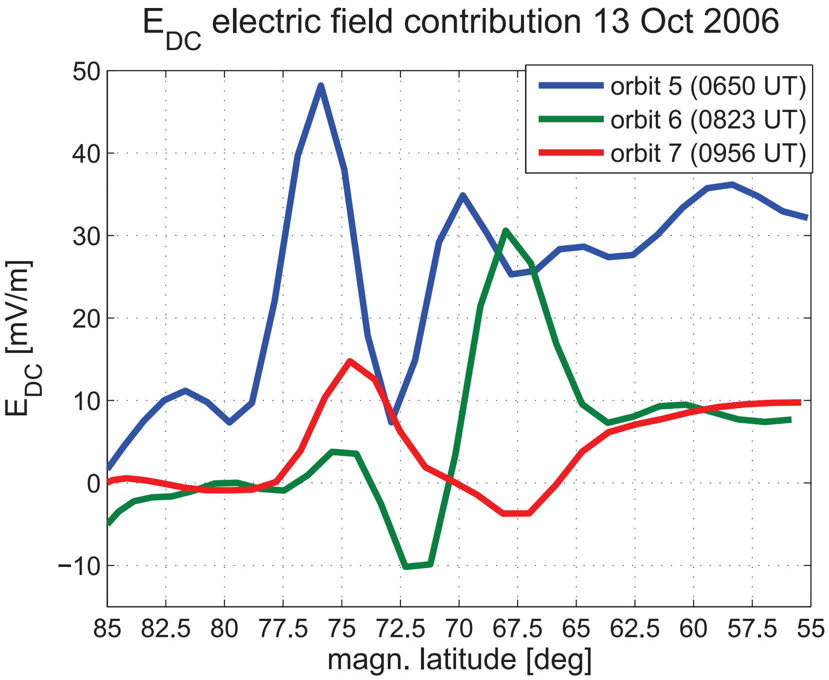

Figure 6.11: E_{DC} contribution, as estimated from Hall currents on 13 October 2006.

3.5×10^{-8} W/m^3 (orbit 6), 1.8×10^{-9} W/m^3 (orbit 7), indicating that our results should be treated as qualitative rather than as quantitative ones.

The right panel presents the height-integrated Joule heating rates per area. They are obtained using Eq. (6.9). The applied conductances amount to $\Sigma_P = 1.9$ S (orbit 5), $\Sigma_P = 2.6$ S (orbit6), $\Sigma_P = 4.9$ S (orbit 7). The heating rates are largest during the latest overflight which has been expected closest to the cusp.
In the third overpass, the Joule heating rate reaches up to 0.016 W/m^2. Maximal values of the two other overflights do not exceed 0.011 W/m^2. The results are large compared to that of Schlegel et al. (2005). These authors report on heating rates of up to 0.0034 W/m^2 during quiet conditions, but they point out that the effective electric field was low during their measurements (35 mV/m in maximum) and they did not consider small-scale electric fields. Again, we have to take into account large uncertainties. The mean errors amount to 2×10^{-4} W/m^2 (orbit 5), 4×10^{-4} W/m^2 (orbit 6), and 2×10^{-4} W/m^2 (orbit 7).

It is worth to mention that the largest contribution unexpectedly comes from the small-scale component. Aruliah et al. (2005) found that Joule heating is increased by 320% under their experiment conditions in February 2003 when using highly variable 1 min data instead of averaged 15 min data. Their explanation is the ion's stochastic motion which increases the ion-neutral friction.
Since the small-scale variability is neglected in most of the models (e.g. GCM's) smoothed electric fields are used leading to an underestimation of vertical winds. In fact, a larger vertical wind would mean a larger vertical transport, an additional upwelling of dense air and therefore a larger contribution to the high-altitude density. However, this is not only true for the cusp-related region.

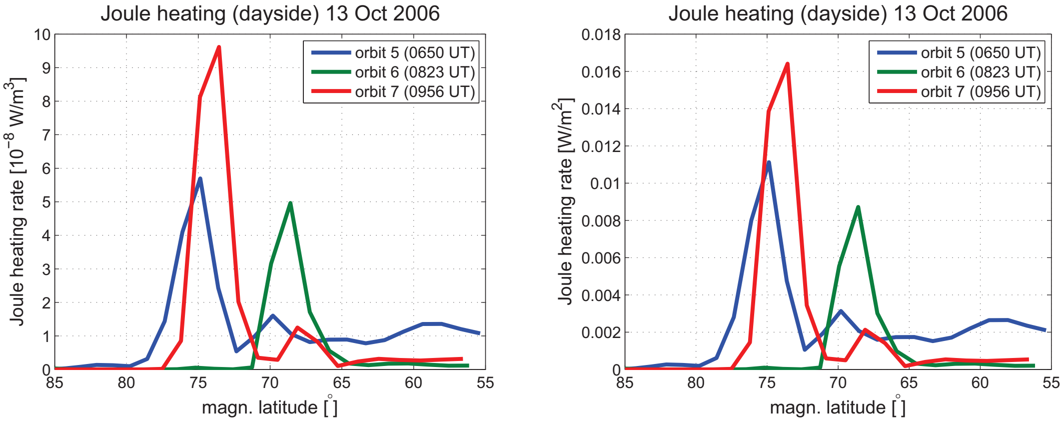

Figure 6.12: Joule heating as derived from the CHAMP-EISCAT campaign on 13 October 2006. The left panel refers to the height-dependent heating rate, $q(h)$, at 140 km. Highest Pedersen conductivities are obtained for this altitude. The right panel displays the Joule heating rate per m^2, applying a Pedersen conductance of 1.9 S (orbit 5), 2.6 S (orbit 6), 4.9 S (orbit 7).

The behaviour of the heating rates resembles that of the neutral density (Fig. 6.3). Both of them show inferior amplitudes during the first and second overflight, but markedly enhanced values for the latest overflight. This behaviour is different from the perpendicular electric field components. Here, the values of the third overpass are not outstanding against the two earlier overpasses (cf. Figs 6.10 and 6.11). Hence, the increase of Joule heating comes from the increase in conductivity/conductance (cf. Figs. 6.5, 6.6).
Even though our results are based on several assumptions, the comparable behaviour of the total mass density/density anomaly and the Joule heating rates at 140 km altitude supports our suggestion that Joule heating at this level provides an important contribution to the formation of the cusp-related density anomaly.

6.5 Conclusions from the CHAMP-EISCAT campaign

The combined CHAMP-EISCAT campaign was scheduled and run in October 2006 in order to observe characteristic features of the ionosphere and thermosphere in the cusp region simultaneously. The thermospheric component, namely the mass density and the density anomaly revealed typical cusp features (cf. Fig. 6.3). From the radar observations we found the Hall conductivity to peak at about 120 km altitude and the Pedersen conductivity at about 140 km altitude in the vicinity of the cusp. The latter exceeds the expected altitude of the σ_P maximum (i.e. E layer) by at least 30 km. This indicates a higher heated layer in the cusp.

For the calculation of Joule heating rates we considered both, large-scale and small-scale components of the effective electric field. Consequently, the heating rates are larger (by a factor of 5) than those derived from a similar campaign in February 2002 and documented in Schlegel et al. (2005). The heating rates are largest during the CHAMP overpass which was assumed to be closest to the cusp. Obviously, there are two components enhancing the Joule heating rates: (1) a heated layer above the E region and (2) an increase in the effective electric field strength. We speculate that this is in particular true for the small-scale electric field component (E_{AC}), since E_{AC} was found to provide a larger contribution than the large-scale component E_{DC} during the overpass closest to the cusp.

Chapter 7

Causes of the cusp-related density anomaly

In the previous chapter, Joule heating has been found to be one of the sources of the neutral fountain. Here, further influences are examined. The aim is to provide a well-grounded sketch of engaged mechanisms which might cause the cusp-related density anomaly.

7.1 Particle precipitation

An important source of ionospheric conductivity in the dark auroral region is particle precipitation.

As demonstrated in the previous sections Joule heating is controlled by the perpendicular electric field and the Pedersen conductivity. The variability of the electric field does not depend on particle precipitation, but the Pedersen conductivity is controlled by the number density of charged particles and the collision frequencies (cf. Eq. (D.5)). Both quantities depend on the ionisation rate and energy deposition rate and are consequently influenced by particle precipitation events. Thus, Joule heating and particle precipitation have to be considered as coupled mechanisms.

The ionospheric response to precipitating particles varies markedly with altitude, in brief: the higher the electron energy the lower the altitude of penetration and peak ionisation.

Theory at high altitudes

For high altitudes, Newell and Meng (1991) report on incoming electrons with a typical energy of ≈ 100 eV, causing an ionisation maximum at about 300 km altitude.

When considering precipitation along a flux tube that is convecting from the dayside across the polar cap towards the nightside we can certainly assume an electron density that decreases continuously along the convection path. When the flux tube traverses the cusp, however, the electron density increases due to particle precipitation. The largest increase occurs in the F2 peak region, in fact caused by injected

electrons. However, the height, hmF2, is not changed by this process. Another moderate increase can be observed at about 200 km altitude, where the higher energetic electrons get stuck.
Due to the lack of loss processes at high altitudes, the electron density remains increased for more than an hour. This has two effects: (1) electron precipitation can be regarded as the main source of F region ionisation and (2) to some extent it can spread over the entire polar cap when convecting with the general antisunward flux (Millward et al., 1999).

Theory at lower altitudes

For lower altitudes, Newell and Meng (1991) report on incoming ions with an energy of $\approx$ 1 keV which penetrate to about 170 km altitude (or even deeper) into the atmosphere. These regions are hardly reached by incoming electrons, i.e. effects at lower altitudes are mostly caused by ions. Therefore, ion precipitation is responsible for the F1 layer which can occur at $\approx$ 150 km in the cusp.

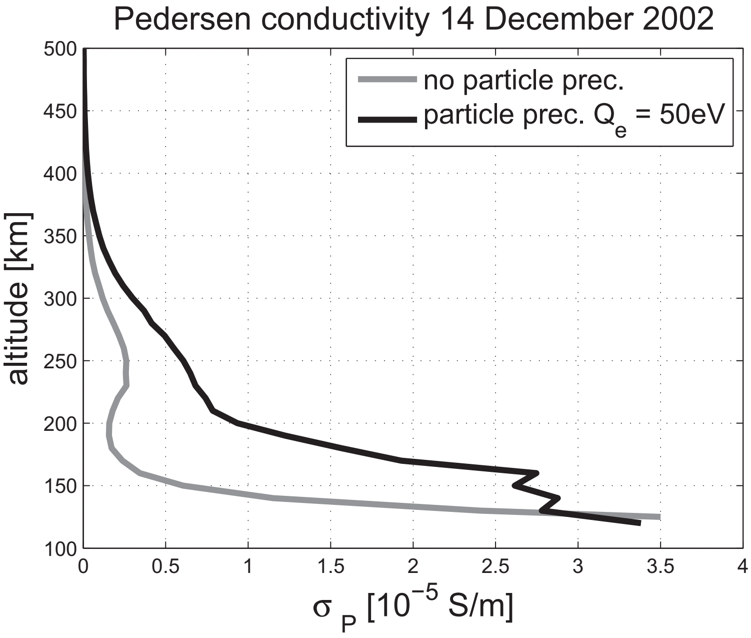

Figure 7.1: Height profile of the Pedersen conductivities according to the electron concentration as derived from model runs of Millward et al. (1999) for 14 December 2002, 0930 UT. This day is characterised by elevated solar activity ($F10.7 = 167$) and moderate geomagnetic activity ($Kp = 2.7$). Considered are the cases of absence of precipitating particles (grey) and presence of precipitation (black).

The increase of electron density at lower altitudes is short-lived and restricted to cusp latitudes, since effective recombination sets in if the flux tube convects out of the cusp towards the pole.

Rosenbauer et al. (1975) quoted ion energy dispersion effects which occur when solar

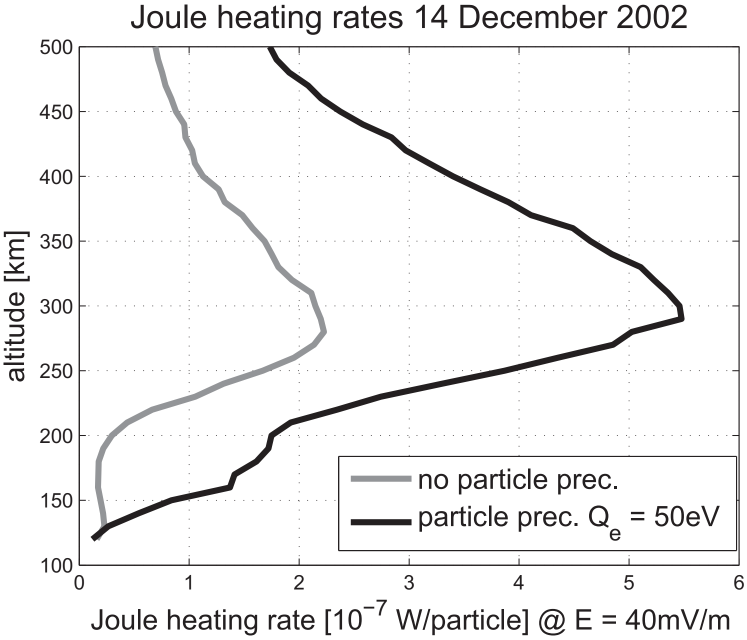

Figure 7.2: Height profile of Joule heating rates according to the electron concentration as derived from model runs of Millward et al. (1999) for 14 December 2002, 0930 UT. Larger Joule heating occurs under particle precipitation conditions.

wind ions enter the magnetosphere on newly merged field lines. As the ionospheric footprint of the fluxtube moves poleward the fast (high energetic) ions arrive first more equatorward than the slower (less-energetic) ions whose impact occurs more poleward.

Newell and Meng (1991) specified a velocity distribution of 1 keV at the equatorward edge and 300 eV at the poleward edge of the cusp for the ions. Therefore, variations in the ion spectrum are more effective in lower latitudes.

Millward et al. (1999) have framed the following consequences of particle precipitation, out of which the second item will be most important for our studies:

- Optical signature: the cusp can be adequately identified by the strong emission at 630 nm. However, this cannot be converted directly to a latitude without considering precipitation effects.
- Conductivity: ion precipitation in the cusp can lead to an elevated conductivity at lower altitudes, especially at the equatorward edge of the cusp.
- Dispersion: the electron density enhancement due to soft electron precipitation (i.e. mainly at higher altitudes) is long-living (> 1 hour), i.e. it convects over the pole away towards the night side. Consequently, the influence of particle precipitation is not only restricted to cusp latitudes.

Unfortunately, CHAMP does not provide adequate measurements to estimate the influence of precipitating particles in a direct manner. Therefore, the idea is to give here an order of magnitude estimate that is based on model predictions.

With the help of the CTIP model Millward et al., (1999) have modelled the effect of particle precipitation on the electron density distribution using typical cusp conditions (Maxwellian energy distribution of 50 eV electrons and 500 eV ions). From their obtained electron density profiles (their Figs. 8 and 9) we calculated the Pedersen conductivity adopting the geophysical conditions quoted there ($Kp = 2.7$, $F10.7 = 167$). These values match very well the conditions of 14 December 2002 ($Kp = 2.7$, $F10.7 = 167$). That is why this day was decided to be taken as an example. In Fig.7.1 height profiles of Pedersen conductivity have been plotted for particle precipitation switched on (black) and off (grey). The Pedersen conductivity was calculated according to Eq. (D.5).

Both curves in Fig. 7.1 do not differ much below 130 km and above 400 km of altitude. Both decrease with increasing height, with a strong decrease below ≈200 km (particle precipitation) and ≈150 km (no particle precipitation), but with a much weaker decrease at higher altitudes. Most interesting: It is quite evident that the conductivity is significantly enhanced, in particluar in the F1 region, above 150 km. This means that the altitude of effective Joule heating is lifted up. Consequently, the heating rate per particle increases significantly and a larger temperature is achieved in the heated region.

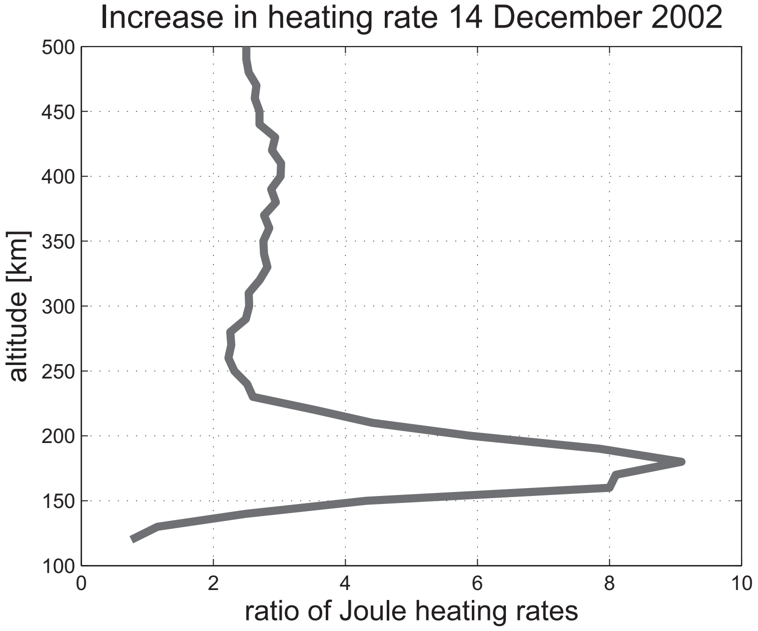

Figure 7.3: Ratio of the Joule heating rates with and without particle precipitation as derived from Fig. 7.2.

This can be checked in a further step. Joule heating rates per particle are obtained from these data. The required particle number densities are provided by MSIS. The heating rates are displayed in Fig. 7.2, again seperately for precipitation (black)

and no precipitation (grey). The heating rates are calculated according to Eq. (6.8) where a typical electric field of 40 mV/m was assumed, similar to the results of Figs. 6.10 and 6.11.
As expected, the Joule heating rate increases when particle precipitation occurs. At the peak in heating rate, it is about twice as large as without particle precipitation, and the altitude of the maximum has increased by about 15 km. This estimate suggests that the mechanisms remain the same, regardless of precipitation events, but the heated particle population seems to be quite different. For illustration we have plotted in Fig. 7.3 the ratio of the increase in heating rate per particle caused by precipitation. This curve peaks at 180 km altitude. At this height range the number densities of the prime species are: $n_{N2} = 6.39 \times 10^{15} m^{-3}$, $n_{O2} = 0.49 \times 10^{15} m^{-3}$, $n_O = 8.53 \times 10^{15} m^{-3}$, according to MSIS for the prevailing conditions. In contrast, the molecular species are dominant at 100 km altitude ($n_{N2} = 8.86 \times 10^{18} m^{-3}$, $n_{O2} = 2.10 \times 10^{18} m^{-3}$, $n_O = 0.46 \times 10^{18} m^{-3}$), but the atomic O becomes much more relevant at CHAMP orbital altitude. For 400 km, MSIS results yield: $n_{N2} = 3.95 \times 10^{12} m^{-3}$, $n_{O2} = 0.11 \times 10^{12} m^{-3}$, $n_O = 1.25 \times 10^{16} m^{-3}$ for comparison. This clearly shows that a lot of additional heat is transferred to the molecular particles.

Particle precipitation in the cusp is generally associated with reconnection at the magnetopause. The merging electric field, E_{merg}, has been identified as a measure for the reconnection rate. For this reason E_{merg} may have a two-fold significance for the cusp-related density anomaly: (1) it reflects the electric field driving the ionospheric currents and (2) indicates the rate at which particle precipitation events occur and thus enhance the conductivity. Dedicated observations are required to further quantify the role of particle precipitation for the cusp-related density anomaly qualitatively.

7.2 Harmonic excitation by the solar wind

In the previous sections we have pointed out the different controlling parameters of the density anomaly. As a next step we intend to examine from which parameters the influence is coming. A period suitable for that approach is the year 2005. It has been reported by Lei et al. (2008) that the solar wind exhibits a periodic velocity variation at a dominant period of 9 days over large parts of the year. As can be seen in Fig. 7.4 (adaption of their Fig. 1), the harmonic oscillations in solar wind speed show some effects both in the thermospheric density (top panel) and in the magnetic activity (bottom panel). Conversely, there is not much indication of a 9-day variation in the solar flux level (second panel). We use this clear difference in the temporal behaviour of the two thermospheric drivers to investigate further the causes for the cusp anomalies.

The interval most suitable for our studies is the first 270 days of 2005. After that period the characteristics of the variations change. Our approach for evaluating the different time series is to apply a Fourier transform and compare the spectral features of the analysed signals. As practised before, only high-latitudinal observa-

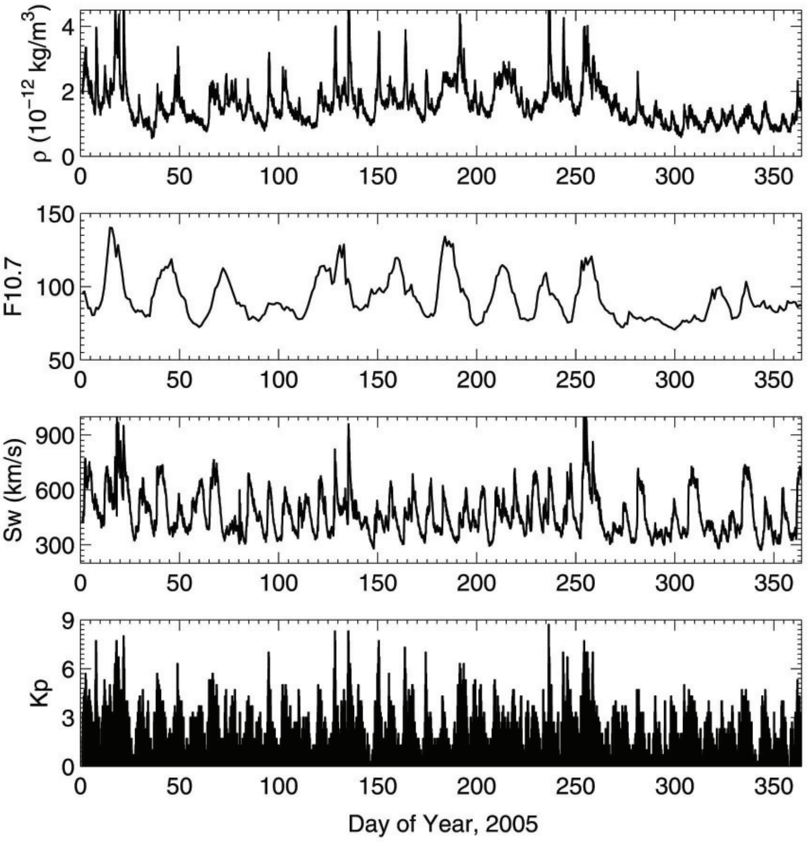

Figure 7.4: The behaviour of the thermospheric mass density (top panel), the solar flux index F10.7 (second panel), the solar wind velocity (third panel), and the magnetic activity index Kp (bottom panel) over the course of 2005. Adapted from Lei et al. (2008).

tions ($|55°| - |89°|$ cgm latitude) are considered. The sampling frequency is once per orbit, where orbit means the segment of the high-latitude overpass over the above mentioned latitudinal range.
We consider in our investigation both the possible drivers and the affected quantities like thermospheric density or cusp-related anomaly. From the results presented in the previous chapters we know that the solar flux and the merging electric field are relevant drivers for the studied anomaly. In addition to that Lathuillière et al. (2008) showed that the magnetic activity indices are suitable proxies for the response of the global thermospheric density to magnetospheric input. For completeness, we therefore included the ap index into our harmonic analysis.

In a first run the spectra of the three drivers are computed from the first 270 days of 2005. Fig. 7.5 shows the amplitude spectra for the various periods in days for the northern hemisphere.

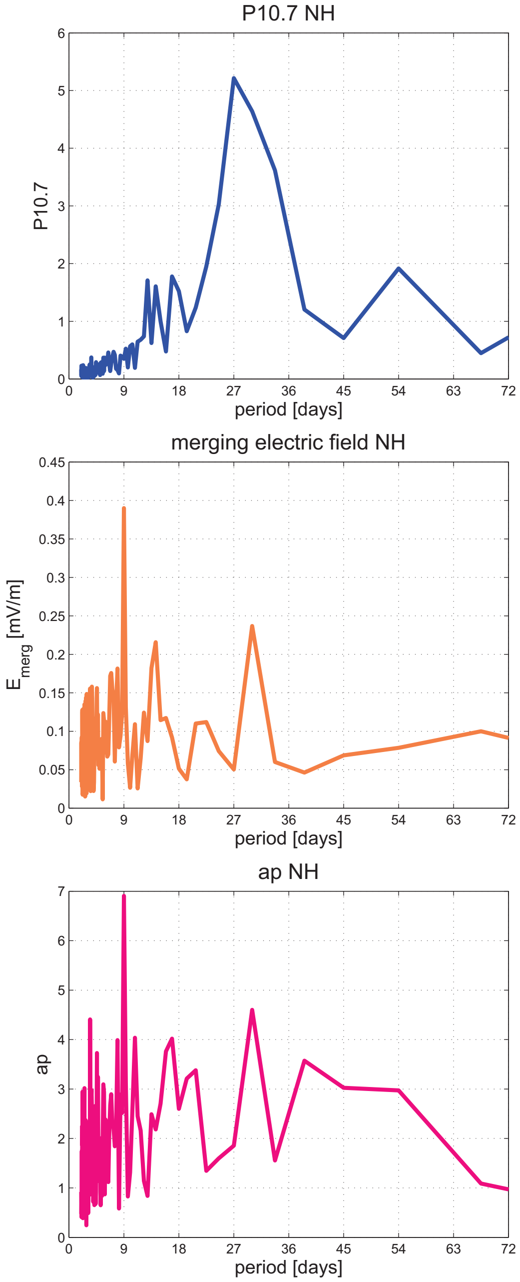

Figure 7.5: Periodogram of the controlling parameters P10.7 (top panel), and E_{merg} (second panel), and for ap (bottom panel) for the NH. The data are based on the first 270 days of 2005. Daily P10.7 values and 3-hourly ap values are applied. The merging electric field was estimated using the average of the 50-min interval before a density anomaly event.

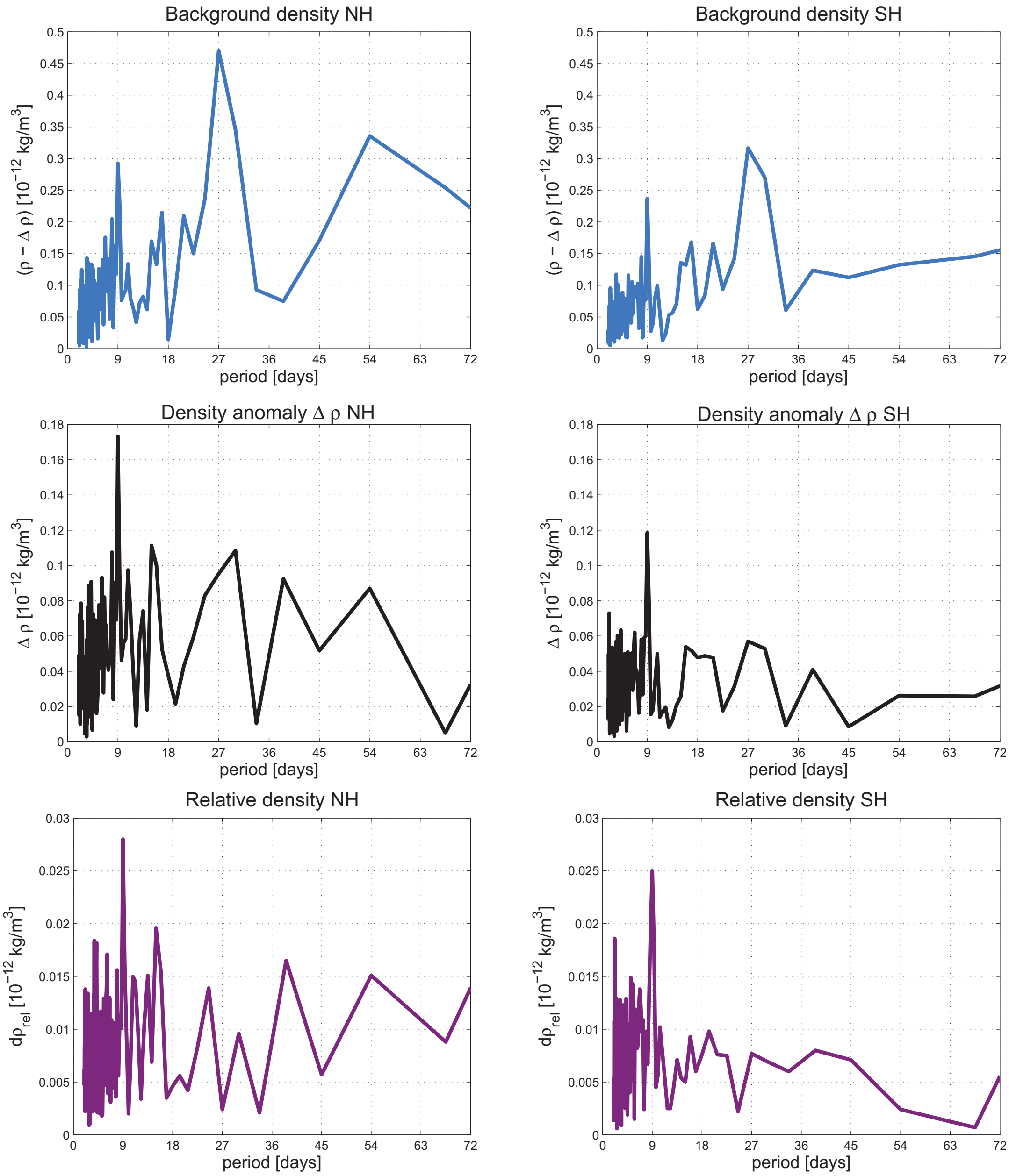

Figure 7.6: Periodogram of the CHAMP-observed background density, $\rho - \Delta\rho$ (top row), the density anomaly, $\Delta\rho$ (second row), and the relative density, $d\rho_{rel}$ (bottom row) for the northern (left) and southern (right) hemispheres. It is based on measurements of the first 270 days of 2005.

The solar flux in the top panel of Fig. 7.5 exhibits a dominant peak at 27 days and a secondary one at double the period (54 days). Smaller and less significant peaks appear between 13 to 18 days but no signal for periods shorter than 13 days. Opposed to that we find a very narrow and prominent spectral peak at 9 days in the merging electric field, E_{merg}, (second panel of Fig. 7.5). Secondary peaks show up at 13.5 and 30 days. From this comparison we can see that the two dominant drivers have a distinctly different spectral content. The spectrum of the magnetic activity, ap, resembles by and large the shape of the E_{merg} spectrum, confirming that geomagnetic activity is primarily controlled by the solar wind input.

As a next step it is interesting to see, how the density in the cusp region is responding to the driver signal. For each orbit we have taken the density values at the time of the anomaly peak. The values considered are the background density, the peak density (anomaly) and the relative anomaly, all of them as defined in Section 5.2. Readings from the northern and southern hemisphere are considered separately. The periodogram determination requires an equidistant dataset. Consequently, orbit segments, where no $\Delta\rho$ could be identified were filled alternatively with the mean value of all $\Delta\rho$ (0.72×10^{-12} kg/m^3). Thus, a dataset of 4197 values for each hemisphere, i.e. one value per orbit is provided.

In Fig. 7.6 the obtained spectra are presented.

The background mass density at cusp latitudes (cf. Fig. 7.6, top row) exhibits a spectrum that shows influences of both the solar flux and the merging electric field. The most prominent peak appears at 27 days. Somewhat smaller is the 9-day peak. Consistent with previous results, the signals at both periods are weaker in the southern than in the northern hemisphere.

When looking at the spectrum of the density anomaly (second row of Fig. 7.6) we see the clear dominance of the 9-day peak. The impact of the solar flux compared to the merging electric field is much reduced, as judged from the spectral distribution. Here the signal at 27 days is only half as large as that of the 9-day period. Hemispheric differences are again as expected.

Finally, the spectrum of the relative anomaly, presented in the bottom row of Fig. 7.6, further emphasises the dependence of the anomaly on the merging electric field. The ratio between the 9 and 27-day amplitudes further increases in both hemispheres. This is consistent with our result from the multi-parameter analysis in Section 5.5.2.

This spectral analysis clearly revealed that cusp-related density anomalies are caused by the interaction of the solar wind with the magnetosphere. The harmonic variation of the solar wind velocity during the first 9 months of 2005 are a unique and fortunate opportunity for our research. The 9-day periodicity is rather monochrom without significant phase jumps over the whole period. This can be deduced from the very narrow 9-day peak of the E_{merg} signal. We can even go a step further and look into the phases of the prime spectral features. For the 9-day period we find a surprisingly good match between the phases of the merging electric field and the

anomaly parameters for both hemispheres. The difference and scatter is limited to a few degrees. As expected, the E_{merg} phase governs to some extent the density signal. In case of the 27-day period we find a close phase relation between the background density and the solar flux, P10.7. Unexpectedly, the density variation leads the P10.7 signal by about one day. This is regarded as an indication that our introduced 1-day shift of the P10.7 data (cf. Section 5.4.1) is not needed. The phase of the 27-day signal in the density anomaly shows already much more scatter, and for the relative anomaly the coherence to P10.7 is totally lost.
The period of 9 days is one-third of the 27-day solar rotation. Temmer et al. (2007) and Vršnak et al. (2007) found that the Sun‘s surface was equipped with three coronal holes during the earlier part of 2005, which were separated by about 120° in longitude at low solar latitude. Fast solar wind streams are expected to come out of each of the holes giving rise to the 9-day periodicity of the wind velocity variation. Obviously, this configuration must have been stable for at least 10 solar rotations.

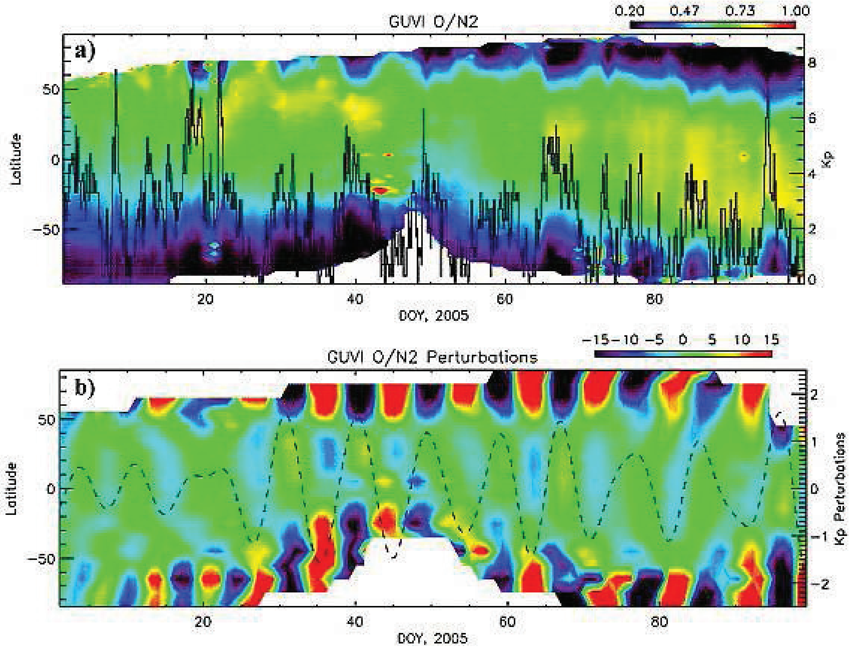

Figure 7.7: GUVI $\Sigma O/N_2$ observations for the first 100 days of 2005. (a) Colour-coded 10° binned raw GUVI $\Sigma O/N_2$ ratio as a function of latitude and time, and Kp (black line). (b) Residuals in 10° bands after bandpass filtering and the removal of an 11-day running mean, expressed as a percentage of the running mean values. Broken line shows Kp after similar bandpass filtering. Adopted from Crowley et al. (2008).

By comparing the spectra of the drivers with our three density parameters certain conclusions can be drawn. The background density, ρ, varies with the change in solar flux (27-day period) as expected, but responds also to the changes in solar wind input (9-day period). This is consistent with the observations of Lei et al. (2008) who report on a global response of the thermosphere to the 9-day variation with an amplitude of about 10% of the background density. We obtain a spectral amplitude at 9 days of 0.3×10^{-12} kg/m^3 (0.25×10^{-12} kg/m^3) in the northern (southern) hemisphere. This has to be compared with the mean density of 4.2×10^{-12} kg/m^3 (2.6×10^{-12} kg/m^3) in the two hemispheres. From that we deduce a modulation of the background thermospheric density at day time auroral latitudes of 7% to 10% by the 9-day excitation.

On top of these background variations we find the anomalous density enhancement in the cusp region. The amplitudes of the 9-day signal here are, however, only half as large as in the background density. The density anomaly is hardly affected by the solar flux level but strongly modulated by the varying solar wind input to the magnetosphere. This strong controlling of the cusp-related density anomaly by the merging electric field and the independence of solar flux is even more evident when looking at the spectra of the relative anomaly. There is no significant signal at the 27-day period left in the spectrum. During this solar minimum year the density anomalies are reduced to effects of less than 3% on average.

What could be the cause for the density anomaly in the cusp region? A vital explanation could be a local change of the thermospheric composition. The Global Ultraviolet Imager (GUVI) on the TIMED satellite provides the opportunity to measure the column density ratio, $\Sigma O/N_2$. It was introduced by Strickland et al. (1995) as the column density of O above the altitude where the N_2 column density equals 10^{17} cm^{-2} ($\approx$ 135 km). From its 630 km orbital altitude GUVI looks down through the thermosphere. Strickland et al. (2001) derived an empirical relation for $\Sigma O/N_2$ from the emission ratio of OI (135.6 nm) to the N_2 Lyman-Birge-Hopfield band. Thus the composition can be determined with a spectroscopic imager.

GUVI has provided for the year 2005 global views of the column density ratio, $\Sigma O/N_2$, for the dayside. Figure 7.7 was adapted from Crowley et al. (2008) to display the results. The GUVI $\Sigma O/N_2$ ratio is plotted as a function of latitude and time for the first 100 days of 2005. The Kp variation is superposed as a black line. There is a clear 9-day periodic variation observed in the ratio at auroral latitudes. The composition varies by some 10% about the mean value. At mid and low latitudes no comparable harmonic variation is observed.

The difference in compositional variations between the cusp region and lower latitudes can be the key to explain our density anomalies. A simple thermal expansion due to heating will not cause a columnar change in the $\Sigma O/N_2$ ratio since the species are equally affected by the increase in scale height. However, if Joule or partical heating in the lower thermosphere is driving vertical winds, molecular-rich air is transported upward accross pressure levels. This will change the $\Sigma O/N_2$ ratio and efficiently enhance the mass density at a fixed height. The combination of CHAMP and TIMED observations shows that the primary heating and following uplift of heavy air is confined to the vicinity of the cusp region. Subsequently, the atmospheric pressure equalises and enhances the mass density globally. Typical propagation times of disturbances from the auroral region to the equator are four hours. This is much shorter than the nine days of input variation.

The suggested scenario for the anomaly implies that the molecules are preferably heated with respect to atomic oxygen. Their temperature and scale height should grow over-proportionally causing a composition change in the upper thermosphere. This effect is expected to be spatially and temporally confined to the appropriately heated region (cusp) and the temperature relaxation time, respectively.

7.3 Assessment of heating mechanisms

In this thesis we have tried to identify the dominant mechanisms that cause the formation of the localised thermospheric mass density enhancement commonly observed in the vicinity of the cusp. Classical explanations like the dissipation of energy provided by electric currents were not sufficient. They neither could account for the local confinement to the phenomenon nor were they consistent with the observed seasonal variability of the density anomaly.
Real progress in elucidating the responsible heating processes has only been achieved by combining observations of the phenomenon from different aspects and by utilising additional model predictions. We envisage the following line of interpretation:

- The energy for causing the density anomalies is provided by the solar wind. The merging electric field has been identified as a suitable parameter for characterising the solar wind input. The solar EUV flux has no direct influence on the anomalies but high fluxes improve the conditions in the thermosphere for the development of mass density anomalies.

- The combination of EISCAT and CHAMP measurements revealed that it is important to consider both the contribution from large-scale and small-scale current structures for estimating the Joule heating rate. When omiting the small-scale part, the estimated rate decreases by a factor of 5 in our case.

- EISCAT observations show that on the event day a layer of enhanced Pedersen conductivity forms around 140 km altitude. Changes in the amount of energy per volume deposited in this layer correspond well to the variation of the mass density at CHAMP altitude.

- Numerical experiments performed with the CTIP ionospheric model show that soft electron precipitation in the cusp region enhances the conductivity particularly in the height range between 150 and 200 km. We regard cusp particle precipitation as the cause for the conductivity layer at around 140 km altitude. The difference in altitude between the modelled and observed layer is most probable due to the difference in solar activity. For the model run, solar maximum conditions were adopted while the EISCAT observations took place during solar minimum.

- GUVI observations on TIMED indicate that molecularly rich air is upwelling into the upper atmosphere in the dayside auroral region at times when the cusp-related anomalies are detected. This coincidence closes the ring of arguments.

In summary, we may state that the soft electron precipitation creates a conducting layer at an elevated altitude confined primarily to the cusp region. The merging electric field possibly provides the power that heats preferably neutral molecules. The differential expansion of the heavier particles changes the composition locally in the upper thermosphere and thus causes the mass density anomaly.

Chapter 8

Resumé

This thesis is best recapitulated by answering the motivating questions raised in Section 3.2.

8.1 Answers to motivating questions

1. Is the density anomaly in the cusp region a continuous phenomenon?

   It could be demonstrated that the cusp-related density anomaly occurs in all years and seasons of the investigated interval (2002–2005). It shows a dedicated variability on different scales. However, it is a continuous phenomenon (cf. Figs. 5.6 and 5.7).

2. What magnitude and scale size does the density anomaly reveal?

   Based on Table 5.2 maximal anomaly amplitudes of $(0.14 - 1.43) \times 10^{-12}\ kg/m^3$ are obtained. Here, large standard deviations indicate a very large scattering. Additionally, the amplitude strictly depends on various parameters (cf. item 4 below). Correspondingly to the predetermined resolution the anomaly is located on average at 73° cgm latitude (NH), -70° cgm latitude (SH), whereas it is characterised by large variations with year and season in the SH but only a weak variability in the NH. The anomaly has a latitudinal range of 12.3°–16.8°, considering the FWHM. Regarding the time scale, the phenomenon lasts roughly 4.5 hours, comprising a central MLT between 1105 MLT ± 15min and 1333 MLT ± 15 min.

3. Is the cusp-related density observed in both hemispheres? If so, does it show systematic differences?

   For the first time, the cusp-related density anomaly was statistically investigated simultaneously in both hemispheres, and it was indeed determined to be a phenomenon of both hemispheres. Its behaviour is comparable in both hemispheres, considering occurence and location, variability with the years, or response to P10.7/E_{merg}. However, the southern hemispheric anomaly amplitudes are weaker (by about 30%). Another distinctive difference is the winter anomaly, developing around southern hemispheric June solstice. Apart from that, the SH anomaly is affected by a larger variability.

4. Does the anomaly show dependences on certain parameters/atmospheric conditions?

   The density anomaly shows a multi-parameter dependence. Hence, it is quite intricate to relate the particular attributes to the responsible controlling parameters. The most important influencing factors are the solar EUV radiation (P10.7), the energy input by the solar wind (E_{merg}), and the background density. Moreover, influences of the IMF components, the seasons, the tilt angle, FACs, the geomagnetic activity, and particle precipitation events have been investigated.

5. Why is the density anomaly not reproduced (sufficiently) in most of high-latitude/upper atmosphere models?

   The density anomaly is a highly sensitive phenomenon of limited dimensions in time and space. Indeed, it was necessary to apply the reduction procedure, as described in Section 5.2 to visualise it in the first place. Apart from that, the controlling parameters, which would serve as essential model input, are to some extent highly variable and of confined dimensions (e.g. cusp position, response to onset/subsidence of Joule heating, particle precipitation events). Moreover, the driving processes have not been fully understood yet, and the number of satellites, which provide continuous readings on a sufficiently long time period, is still restricted.

   On the one hand it leads to a very time-consuming procedure, requiring large calculating capacity to simulate the cusp in global models like MSIS. On the other hand the model resolution might be insufficient for visualising cusp phenomena. Nonetheless, it is indispensable to investigate and understand these phenomena and its features in order to contribute to the improvement of atmospheric models and continuative consequences (e.g. effects on the correction of satellite track calculations).

6. What causes, releases, excites the cusp-related density anomaly? Which causes can come into question? What are the roles of Joule heating, composition changes, particle precipitation? Are there other processes/mechanisms that have to be taken into account?

   The cusp-related density anomaly is caused by upwelling of dense air from lower levels (neutral fountain effect).
   The vertical motion is generated by Joule heating at E layer and F layer altitudes and particle precipitation in the cusp.
   Both mechanisms do not suffice to explain the whole density enhancement. Thus, composition changes are supposed to be the main cause: Generation of neutral winds (for instance in consequence of the above mentioned processes) induces an upward transport of heavier material from deeper atmospheric layers which contributes to the increase of mass density.

In essence, the cusp density anomaly is composed of the interaction of the not cusp-specific solar activity level and the background density as well as cusp-specific heating mechanisms due to Joule heating and particle precipitation. They can cause composition changes and vertical transport and depend on the magnetic activity.

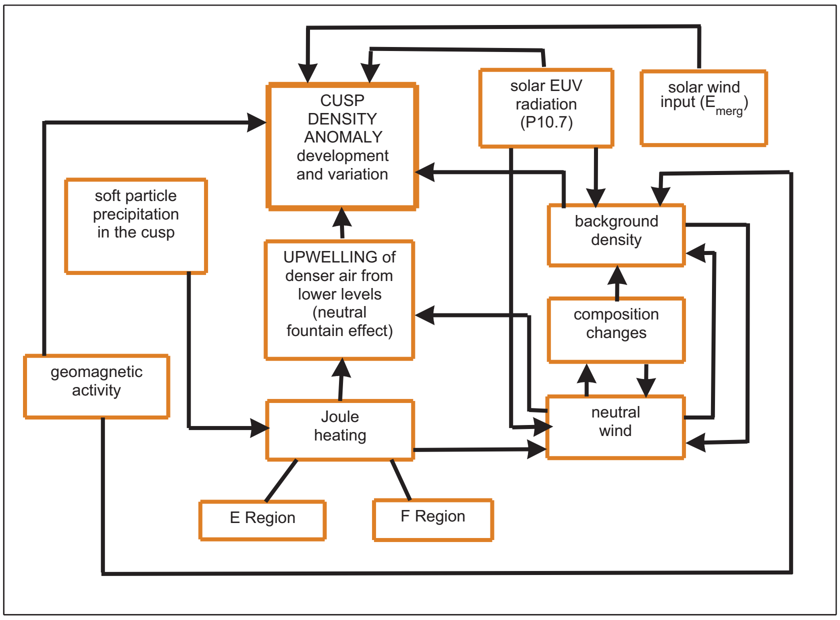

Figure 8.1: Influences on the development and variation of the cusp density anomaly.

8.2 Summary and conclusions

This work is based on the analysis of CHAMP accelerometer data for the dayside high-latitude thermosphere. For the first time, a statistical analysis was performed simultaneously for both hemispheres over a multi-year period.
The thermospheric total mass density, as derived from the spacecraft's deceleration, exhibits a characteristic enhancement in the vicinity of the cusp: the so-called cusp density anomaly.
This phenomenon occurs at both hemispheres but is generally less pronounced in the South. It is a continuous feature in the upper atmosphere.

The dependence on various influencing parameters has been shown: The anomaly undergoes seasonal variations and it changes its intensity according to the solar activity (correlation with P10.7), energy input of the solar wind (merging electric field), and variation of the background density. The latter seems to have the largest impact. The influence of the geomagnetic activity is impressively recognised by facing the cusp density anomaly in geographic and geomagnetic coordinates: it can

only be visualised in a geomagnetic coordinate system.
In a second step it was asked for possible causes. It is quite evident that the cusp density anomaly is caused by the neutral fountain effect at cusp latitudes. However, the question is: What causes the air-upwelling? This question could not be answered unambiguously.
Although different contributions to this process have been identified and analysed, it was not possible to explicitely determine the percentage of each contribution.
A periodicity analysis revealed that the cusp-related density anomaly is caused by the interaction of the solar wind with the magnetosphere. The solar wind input provides the energy which is necessary to form a neutral fountain. With help of a combined CHAMP-EISCAT campaign Joule heating rates have been calculated and identified as a contributor to generate the density enhancement. As estimated by Demars and Schunk (2007), typical E region Joule heating is not enough to cause the density anomaly observed by the satellite. Further heating at F1 region altitudes has been considered reasonable. Indeed, the campaign results revealed a conductivity layer at about 140 km. As obtained from CTIP-SHL model results this uplift of the heated layer might be due to soft particle precipitation in the cusp. However, the uplift cannot be realised without vertical winds. It has been supposed to be generated by adiabatic expansion of the heated air volume and convective vertical motion carrying heavy material and thus affecting the composition of the air and forcing a mass density enhancement at higher altitudes.
The mentioned processes are summarised in Fig. 8.1.

8.3 Open questions and suggestions for further work

Finally, a collection of remaining or thesis-induced questions and suggestions for further work are presented.

At first, we can ask for the density anomaly's embedding in the larger-scale context. It has been examined whether the cusp density anomaly contributes to the mid-latitude density anomaly addressed in Liu et al. (2007). For that purpose, crest-to-trough ratios of the mid-latitude density anomaly have been estimated and compared to the cusp density anomaly. No correlation was revealed. Lei et al. (2008) showed that the excitation of the cusp-related neutral fountain caused a global variability of the thermospheric mass density in 2005. However, it is still needed to investigate how other (thermospheric) regions and characteristic quantities might be affected.

Of course, a remaining question addresses the importance of composition changes for the cusp density anomaly. Unfortunately, the composition cannot be measured onboard CHAMP. Thus, a comparison of our results with other satellite-based measurements would be advisable, for instance the analysis of GUVI data, recorded onboard the TIMED satellite. A direct comparison of the $\Sigma O/N_2$ column density with the cusp density anomaly might provide insight to composition changes and their impact on the cusp density anomaly.

Concerning the specific heating mechanisms, further research is required to identify the roles for e.g. soft particle precipitation, small-scale transverse electric fields or kinetic Alfvén waves for lifting up the molecular constituents.

Another considerable question is raised by the analysis of Joule heating rates: How much contribution to the heating rates comes from the large-scale and small-scale components? The small-scale component dominates in our results. This would require investigations that are capable to prove/reject the speculation of Aruliah et al. (2005), arguing that averaging over a longer time period might neglect the ion's stochastic motion and therefore reveal a significantly lower heating rate.

Apart from that, the influence of FACs has not been clearly estimated up to now. CHAMP data might provide a formidable data base for further studies. A related research activity has currently been started (Ritter et al., 2008).

To improve the relevance of our results, a larger and more exact dataset would be an advantage. For that purpose, it would be an option to preprocess and harness further CHAMP recordings, in particular those obtained in 2000 and 2001 (during high solar activity periods). Additionally, the quality of the CHAMP-derived density and wind estimates is improvable.

Operations like the upcoming Swarm mission, orbiting more than one satellite, will provide the possibility to consider the phenomena with higher resolution, better coverage and higher sampling frequency.

The merging electric field derivation might be significantly improved by applying Weimer model results (according to Weimer (1995), Weimer (2001)) to estimate the transit time between the measurement taken at the L1 point and the upper atmosphere/ionosphere. This might possibly lead to a dedicated result for the time delay between a merging electric field event and the cusp density anomaly.

Apart from that, it would be advisable to start with the incorporation of our results in corresponding model simulations.

It is finally worth to mention that it would be promising to operate a combined CHAMP-EISCAT campaign in times of larger solar and geomagnetic activity. This was impossible in the time-frame of this project, but it would have probably provided more than one sufficient experiment day and less ambiguous results. The behaviour and development of the cusp-related density anomaly over the course of several years were investigated in this thesis. Studying the influence of the main controlling parameters and the suggested generation mechanism emphasised that it is important to consider the neutral thermosphere and the magnetosphere/ionosphere as highly coupled systems. The cusp-related density anomaly was found to be relevant for incorporation in atmospheric models. With these results the thesis contributes to the aim of the CAWSES (Climate and Weather of the Sun-Earth System) project to significantly enhance the understanding of the space environment and its impact on life and society.

Appendix A

Portrayal of density and wind determination

We employ CHAMP accelerometer Level 2 data with a sampling rate of 10 seconds which are already free of spurious spikes. Initially, the percentage of solar radiation pressure was removed from the acceleration components, a_x and a_y.

These pre-processed data were used to derive the density and wind estimates as described in the following:

We apply a coordinate system defined by the flight direction x, the nadir z and the y-axis completing the triad. The accelerometer readings are provided with specific geographic coordinates, orbit altitude above the reference ellipsoid and time in GPS seconds. These coordinates are converted to Modern Julian Days (MJD), local time and corrected geomagnetic (cgm) latitude, longitude and magnetic local time (MLT).
Subsequently, we take into account the deviation angles β (pitch; rotation around the y-axis) and γ (yaw; rotation around the z-axis). Their definition is illustrated in Fig. A.1. We neglect the deviation in x-direction (roll), since it has no resolvable effect on the considered components, a_x and a_y.
The a_x correction is conducted by multiplication with $(1 - sin\beta)$:

$a'_x \; = \; a_x"(1 - sin\beta)$.

The a_y correction is affected by a time-dependent bias. Lühr (personal communication, 2005) provided the following correction function for the year 2003:

$$\begin{aligned} bd \;&=\; 0.356 \;-\; 0.0009412\,MJD \;+\; (6.554 \cdot 10^{-7})\,MJD^2 \\ &\quad -(1.653 \cdot 10^{-10})\,MJD^3 \;+\; s, \end{aligned} \tag{A.1}$$

which was extended to our four-year investigation period by varying the summand s as follows: $s = 0.01$ for $731 \leq MJD \leq 925$; $s = 0$ for $925 \leq MJD \leq 1543$; $s = 0.051$ for $1543 \leq MJD \leq 1676$; $s = 0.04$ for $MJD > 1676$. We now write for the corrected component:

$$a'_y = \frac{a_y{''} + bd}{c}, \tag{A.2}$$

with $c = 1.6$. This scale factor is required due to the flight characteristics of the spacecraft and the anisotropy of the C_D coefficient. C_D is considered to be 2.2 (as recommended by ESA) no matter which part of the satellite's surface is affected. The additional scale factor, c, is introduced to compensate the differences in C_D for the different surfaces (along-track or cross-track). This has been studied in detail in the diploma thesis of Binder (2005) who found the scale factor of $c = 1.6$ to be appropriate. Interestingly, Binder (2005) revealed, that it is not necessary to apply any scale factor if the satellite had rotated by 90°.

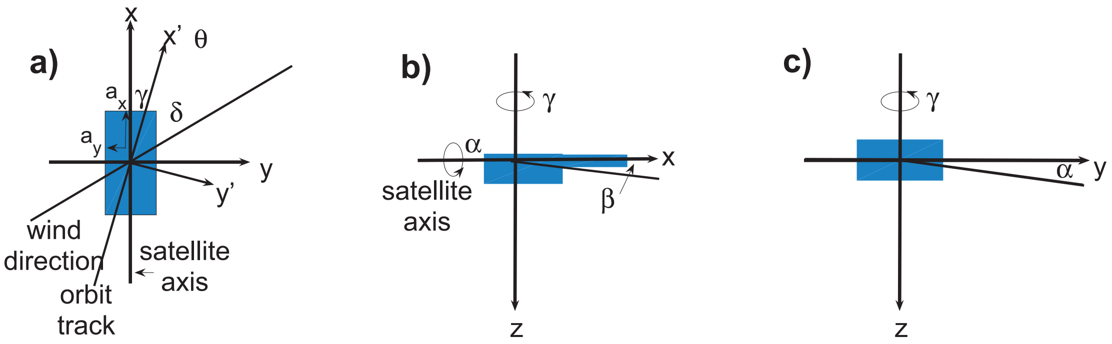

Figure A.1: Schematic view on CHAMP from different directions: a) top view: θ: angle between satellite axis and wind direction, δ: angle between orbit track and wind direction, γ: yaw angle (angle between satellite axis and orbit track; rotation around the z-axis). b) side view: β: pitch angle (rotation around y-axis). c) back view: α: roll angle (rotation around the x-axis, which has no impact on the applied accelerometer readings).

In a next step the corrected acceleration components were rotated into a satellite-based coordinate system, applying the yaw angle γ,

$$a_x = a'_x cos(\gamma) - a'_y sin(\gamma), \tag{A.3}$$

$$a_y = a'_y cos(\gamma) - a'_x sin(\gamma), \tag{A.4}$$

to take into account the differences between the observed component in along-track direction and the axis parallel to the satellite axis.

The two components, a_x and a_y, can now be used to derive the transverse wind:

$$v_y = (7600 m/s + v_{c0} \cdot cos(i)) \frac{a_y}{|a_x|} \tag{A.5}$$

It consists of the velocity in flight direction (approximated by the orbit velocity of 7600 m/s), and the velocity in cross-track direction, comprising the corotational wind component v_{c0} (see below), the spacecraft's inclination $i = 87.25°$, and the acceleration component ratio $a_y / |a_x|$.

Since the onboard coordinate system corotates with the Earth we have to remove the corotational component from the cross-track wind to be able to consider the findings in an Earth-fixed frame.

The corotational wind velocity, $v_{c\phi}$, can be expressed:

$$v_{c\phi} = \Omega_E (R_E + h) cos(\phi), \tag{A.6}$$

with the Earth's angular velocity $\Omega_E = 2\pi/86400s$, the Earth's radius R_E, and the altitude h. Thus, v_{c0} provides the corotational velocity above the equator.

Great care has to be taken concerning the sign of the wind estimates.
Since we are interested in a global zonal wind picture, the sign of the wind estimates from the ascending branch of the orbit has been reversed. The ascending branch has been chosen by definition to get a consistent dataset. In fact, the onboard coordinate system defines an eastward zonal wind to be positive when CHAMP is on the ascending branch, but simultaneously, it defines a westward zonal wind to be positive when CHAMP is on the descending branch. This discrepancy has been cleared out by reversing the sign.

We can now derive the thermospheric mass density as given in Eq. (4.1), applying the well-known quantities m (satellite mass, $m \approx 520$ kg at the beginning of our observation period, 503 kg at the end of 2005), C_D (drag coefficient; the ESA recommends $C_D = 2.2$), the front surface of the satellite $A_x = 0.74\, m^2$ and its side surface $A_y = 3.12\, m^2$, and the angle α which is calculated with the help of the measured (corrected and rotated) acceleration components a_x and a_y: $tan\alpha = |a_y| \,/\, |a_x|$:

$$\rho = \frac{2m\sqrt{a_x^2 + a_y^2}}{C_D(7600(m/s)^2 + v_y^2)A_{eff}}, \tag{A.7}$$

where

$$A_{eff} = A_x cos(\alpha) + A_y sin(|\alpha|). \tag{A.8}$$

Appendix B

Least-squares error minimisation (LSEM) procedure

The *calculus of variations* was developed ≈ 1800 by Joseph-Louis Lagrange to be able to calculate extremal problems of mathematical functions in mathematics and theoretical physics. Variations play an important role in the field of geodesy and differential geometry, but also concerning the problem of minimal surfaces, which occurs even when regarding simple soap bubbles.

Codrescu et al. (2000) solved such an extremal problem to estimate this particular vector out of an accumulation of vectors in a bin, for which the associated error function (cost function) becomes minimal. For every bin this particular mean direction, norm, and standard deviation are determined which produce the least possible difference (in a least square sense) of the measured vector. This method was transferred and applied to our problem of wind vector estimation. It is described in detail in the following.

Given is a bin which contains n measurements, a wind velocity vector u_{cross_i} for each measurement i, and an angle α_i for each measurement defining the observation direction. With the wind velocity of the mean wind v and its observation angle γ an error function $FE(v, \gamma)$ can be calculated:

$$\begin{aligned} FE(v,\gamma) &= \sum_{i=1}^{n} \left(u_{cross_i} - v\, sin\,(\gamma - \alpha_i)\right)^2 \\ &= \sum_{i=1}^{n} u_{cross_i}^2 - 2\,v \sum_{i=1}^{n} u_{cross_i} sin\,(\gamma - \alpha_i) \\ &\quad + v^2 \sum_{i=1}^{n} sin^2\,(\gamma - \alpha_i) \end{aligned} \tag{B.1}$$

With the help of the *calculus of variations* v and γ can be estimated: We have to find this particular v and γ for which the error function becomes minimal. Setting the first derivative to zero, $FE\,(v, \gamma) \,=\, 0$, we can derive an expression for v:

$$\begin{aligned}
\frac{\partial FE}{\partial v}_{\gamma=const.} \quad & \overset{!}{\widehat{=}} \quad 0 \Leftrightarrow \\
0 \quad & \overset{!}{\widehat{=}} \quad -2\sum_{i=1}^{n} u_{cross_i} sin\left(\gamma-\alpha_i\right) + \frac{1}{2} v \sum_{i=1}^{n} sin^2\left(\gamma-\alpha_i\right) \Rightarrow && \text{(B.2)} \\
v \quad & = \quad \frac{\sum_{i=1}^{n} u_{cross_i} sin\left(\gamma-\alpha_i\right)}{\sum_{i=1}^{n} sin^2\left(\gamma-\alpha_i\right)}. && \text{(B.3)}
\end{aligned}$$

Replacing v in Eq. (B.1) by this expression yields:

$$\begin{aligned}
FE(v,\gamma) \quad & = \quad \sum_{i=1}^{n} u_{cross_i}^2 + \frac{\left(\sum_{i=1}^{n} u_{cross_i}\, sin(\gamma-\alpha_i)\right)^2 \left(\sum_{i=1}^{n} sin^2(\gamma-\alpha_i)\right)}{\left(\sum_{i=1}^{n} sin^2(\gamma-\alpha_i)\right)} \\
& - \quad \frac{2\left(\sum_{i=1}^{n} u_{cross_i} sin(\gamma-\alpha_i)\right)\left(\sum_{i=1}^{n} u_{cross_i} sin(\gamma-\alpha_i)\right)}{\left(\sum_{i=1}^{n} sin^2(\gamma-\alpha_i)\right)} \\
FE(v,\gamma) \quad & = \quad \sum_{i=1}^{n} u_{cross_i}^2 - \frac{\left(\sum_{i=1}^{n} u_{cross_i} sin(\gamma-\alpha_i)\right)}{\left(\sum_{i=1}^{n} sin^2(\gamma-\alpha_i)\right)} && \text{(B.4)}
\end{aligned}$$

The minimum of $FE\left(v,\gamma\right)$ equals the maximum of the fraction term in Eq. (B.4), which can be found by varying the independent parameter, γ. Calling the angle γ for which the fractional term becomes maximal γ_m, the standard deviation can be written:

$$\sigma = \frac{1}{n-1}\left[\sum_{i-1}^{n}\left(u_{cross_i} - v\, sin\left(\gamma_m-\alpha_i\right)\right)^2\right]^{1/2}. \tag{B.5}$$

Appendix C

Overview on applied models

This study includes the consultation of various models, once to compare measurements and observations with model results, once to replace unavailable measurements by model simulations, or once to be able to evaluate the behaviour of different parameters for a given time/area.

In the following a brief characterisation of the applied models is presented.

C.1 NRLMSISE-00

Naval Research Laboratory Mass Spectrometer and Incoherent Scatter Radar - Empirical atmospheric model

Empirical models simulating the mesospheric and thermospheric conditions are indispensable to comprise upper atmospheric features, in particular for detailed data analysis processes, for a successful operation of scientific missions (like the CHAMP mission) or for the selection of onboard measurements.
Hedin et al. (1987); Hedin et al. (1991) developed the MSIS series. These models are used to calculate composition, total mass density and temperature distribution. The first version, MSIS-86, provides simulations above 90 km altitude. The subsequent versions, MSIS-90 and NRLMSISE-00, model the atmospheric conditions even above ground level. They consist of the parameterised analytical approximations of the physical theory on the vertical atmospheric structure as a function of space, time, solar activity (represented by F10.7) and geomagnetic activity (Ap).

The model calculations are based on ISR data, mass spectrometer measurements, solar UV occultation data, observations from ballistic experiments and detonation tests, drag measurements from accelerometer readings, temperatures and O_2 densities.
With regard to statistic variabilities, the input data are interpolated/extrapolated providing composition and temperature distribution of the atmosphere in dependence on time, geophysical conditions and the not-specified location.
The model responses to the geomagnetic activity level and is thus able to estimate

storm-time conditions. However, it cannot resolve local structures and short-time variations as they would be necessary to detect particular storm systems.
Main driver is the solar EUV flux as represented by F10.7. While MSIS-90 shows a very strong dependence on F10.7 this effect was attenuated in NRLMSISE-00, since it can cause artificial effects which are not justified by reality.
The basic structure of the model can be described by the Bates-Walker equations (Picone et al., 2002).

C.1.1 IGRF

International Geomagnetic Reference Field

Careful considerations for the mathematical expression of the actual EMF and its variations have been made already in the late 1930s (Chapman and Bartels, 1940). Today, the IAGA recommends the use of IGRF for such purposes. It is released and edited by the IAGA working group V-MOD (Maus et al., 2005).
The IGRF is a mathematical model which returns the EMF and its secular variations in dependence on time and place. Here, the online version of the 10^{th} generation IGRF model (IGRF-10, revised 2005), available at http://ccmc.gsfc.nasa.gov/modelweb/igrf.html was applied. Its modulation is 0.1 nT at application of data up to the 13^{th} degree polynomial (1^{th} degree $\propto$ dipole) for the main field of the years 2002-2004, and it is up to the 8^{th} degree for the year 2005.

C.1.2 IRI

International Reference Ionosphere

The Commitee on Space Research (COSPAR) and the International Union of Radio Science (URSI) service the ionosphere model IRI (Bilitza and Reinisch, 2008).
It simulates the ionospheric parameters electron density, electron temperature, ion temperature, ion drift, ionospheric total electron content (TEC), F1 and spread F probability, and the portion of atomic oxygen ions O^+, atomic hydrogen ions H^+, helium ions He^+, molecular nitric oxide ions NO^+, and molecular oxygen ions O_2^+, dependent on time and place for altitudes of 50–2000 km.
Mainly, it is established by data from ionosondes, ISR, topside sounders, satellites and rockets. Up to now, ion drift model results, magnetic storm effects, and special features of the polar and auroral ionosphere are not incorporated. For our purpose the IRI-2001 online version at
http://ccmc.gsfc.nasa.gov/modelweb/models/iri.html was sufficiant.

C.1.3 POMME 3

POtsdam Magnetic Model of the Earth

POMME 3 models the EMF between the Earth's surface and some 1000 km of altitude. It is based on CHAMP observations. Ørsted and SAC-C satellite data are used for control and verification. The returned magnetic field data depend on time, place, altitude, Dst/Est/Ist activity indices, IMF B_x and B_y components (which are required as input parameters for ex post calculations; Maus et al., 2006). The model is valid for a certain time period which embraces several years and is specified in the corresponding version. Its uncertainty amounts to values between 4 nT in the centre period and 100 nT for forecasts.

C.1.4 CTIP

Coupled Thermosphere-Ionosphere-Plasmasphere Model

The CTIP model family was originally developed by M. Codrescu and T. J. Fuller-Rowell (Millward et al., 1996) and consists of a global thermosphere model, a high-latitude ionosphere model and a low and mid-latitude ionosphere-plasmasphere model.

Dependent on the Hemispheric Power Index (activity level), F10.7, ACE Level 2 solar wind data (solar wind density, solar wind velocity, IMF magnitude, clock angle), dipole tilt angle, and dipole orientation neutral parameters (neutral wind vector, neutral gas temperature, number densities of O, O_2, and N_2, mean molecular mass) and ionospheric parameters (ion density, and ion temperatures of H^+, O^+, N_2^+, O_2^+, N^+), and the NmF2 number density at F2 peak altitude are modelled.
Here, the three sub-models are coupled via conservations of energy, momentum and mass. The corresponding equations are solved for pressure levels of the rotating Earth. For the neutral components, a resolution of 2° in latitude, 18° in longitude is obtained. The ionospheric parameters are returned for regions poleward of 23°. The plasma parameter resolution corresponds to the assumed flux tube. Miscellaneous influencing parameters like Coriolis effects, pressure gradient force, ion drag force, heating/cooling via advection, diffusion, UV, EUV, IR radiation, ionospheric Joule heating, neutral composition and transport processes, gravitation, collision processes, $\vec{E} \times \vec{B}$ drifts or flux tube orientation are considered.
In this study CTIP was not used explicitely but via a thereof developed model for the cusp (Millward et al., 1999), see SHL (Section C.1.5).

C.1.5 SHL

Sheffield High-Latitude model

Among other applications the SHL model, developed at the University of Sheffield, can be used to simulate the ionosphere at high latitudes under the impact of charged particle precipitation.

As reported by Millward et al. (1999) the model considers the behaviour of a single flux tube traversing the cusp under the influence of the magnetospheric convection electric field.
According to Newell and Meng (1995) precipitating electrons and ions in the model are assumed to have a Maxwellian energy spectrum with a maximum differential energy flux of 6×10^8 (1×10^8) $eV\, cm^{-2} s^{-1} sr^{-1} eV^{-1}$ at an energy of 100 eV (1 keV) for electrons (ions). The ion spectrum was provided with an energy cutoff at 900 eV to prevent it from unrealistic results. A pure Maxwellian flux spectrum would

result in too large electron densities, especially between 200-300 km altitude. Below 150 km, however, there is no difference between the model runs with and without ion energy cutoffs, since only high-energetic ions can reach this region.

Under these conditions the continuity and momentum equations for O^+, H^+, He^+, NO^+, O_2^+, and N_2^+ as well as the energy balance equations for O^+, H^+, He^+ and electrons are solved for altitudes between 100–10000 km. Applied thermospheric air density and temperature values are taken from MSIS; the zonal wind components are adopted from CTIP model calculations in the SHL model.

For the results cited in Section 7.1 the SHL model was run for winter solstice conditions and F10.7 = 167, an electron energy of $500eV$ and an ion energy of $1keV$.

Appendix D

Derivation of conductivities

In this Section it is presented how to derive Hall, Pedersen and Birkeland conductivities.

D.1 List of parameters

$I:$ Amperage $[I] = A$
$\vec{I}:$ Current $[\vec{I}] = A$
$U:$ Voltage $[U] = V$
$R:$ Resistance $[R] = \mathrm{V/A} =$
$L:$ Conductance $[L] = [1/R] = A/V$
$P:$ Power $[P] = W$
$\vec{\jmath}:$ Current density $[\vec{\jmath}] = [\vec{I}/A] = A/m^2$
$A:$ Area $[A] = m^2$
$\sigma:$ Conductivity $[\sigma] = S/m$
$\vec{E}:$ Electric field $[\vec{E}] = V/m$
$i:$ Index ion
$e:$ Index electron
$n:$ Index neutral
$s:$ Index species
$q:$ Charge $[q] = As = C$
$n:$ Particle density $[n] = 1/m^3$
$\vec{u}:$ Drift velocity $[\vec{u}] = m/s$
$e:$ Elementary charge $[e] = 1.6021773 \cdot 10^{-19} C$
$\vec{B}:$ Magnetic field $[\vec{B}] = Vs/m^2 = N/Am = T$
$\nu:$ Collision frequency $[\nu] = 1/s$

ω : Gyro-frequency $[\omega] = 1/s$
m : Mass $[m] = kg$
$\vec{F}_e$: Electric force $[\vec{F}_e] = kg \cdot m/s^2 = N$
$\vec{F}_B$: Magnetic force $[\vec{F}_B] = kg \cdot m/s^2 = N$
$\vec{F}_{Fr}$: Frictional force $[\vec{F}_{Fr}] = kg \cdot m/s^2 = N$
$\vec{J}_H$: Hall current $[\vec{J}_H] = A$
$\vec{J}_P$: Pedersen current $[\vec{J}_P] = A$
σ_H : Hall conductivity $[\sigma_H] = S/m$
σ_P : Pedersen conductivity $[\sigma_P] = S/m$
$\sigma_{||}$: Birkeland (parallel) conductivity $[\sigma_{||}] = S/m$

D.2 Theroretical derivation of the conductivity

Following the interpretation of Prölss (2001) the general derivation of the conductivity is based on Ohm's law: $I = U/R = LU$, which can be written in its local form:

$$j_K = \sigma_K E_\perp \Leftrightarrow \sigma_K = j_K/E_\perp,$$

with $_K$ being an index that can be replaced by a specification of the conductivity later on. The local form shows that the conductivity is controlled by the density and mobility of the available charged particles.

Besides, the power can be written: $P = \vec{\jmath} \cdot \vec{E}, \ \ P = U \cdot I$.

The current density, i.e. the current per area is defined $\vec{\jmath} = \vec{I}/A$, but it can also be understood as a flow of charged particles, i.e. as the transport of charges per time unit and area. Therefore, it is always a positive value unless it is zero. Meanwhile, the current, $\vec{I}$, can be expressed as the (netto) transport of charged particles per time unit and reference area that is caused by the motion of the charged particles themselves: $\vec{I} = qn\vec{u}A$. Then, the current density can be written (for a species s): $\vec{\jmath}_s = q_s n_s \vec{u}_s$, i.e. for electrons $\vec{\jmath}_e = q_e n_e \vec{u}_e$, and for ions $\vec{\jmath}_i = q_i n_i \vec{u}_i$. Writing $q_e = -e$ and $q_i = +e$, and assuming $n_i \cong n_e$ yields: $\vec{\jmath}_e = -e n_e \vec{u}_e$; $\vec{\jmath}_i = e n_e \vec{u}_i$. Consequently, the k-th mode of the current density is:

$$\begin{aligned} \vec{\jmath}^K &= \left| \sum_s q_s n_s \vec{u}_s^K \right| = \left| q_i n_e \vec{u}_i^K + q_e n_e \vec{u}_e^K \right| = e n_e \left| \vec{u}_i^K - \vec{u_e}^K \right|; \\ \Rightarrow \sigma_K &= \frac{|\vec{\jmath}_K|}{E_\perp} = \frac{e n_e \left| \vec{u}_i^K - \vec{u}_e^K \right|}{E_\perp} \qquad \text{(norm)} \end{aligned} \tag{D.1}$$

How to estimate the drift velocity?

The drift velocity, $\vec{u}$, can be derived from the force balance relations for a gas of charged particles. With the two assumptions:

1. there act only electric, magnetic and frictional forces,
2. there are no collisions between the charged particles, but only between the neutral gas and the charged particles,

we can write for the energy balance equation:

$$0 \;=\; \underbrace{n_s q_s \vec{E}}_{\vec{F}_E} + \underbrace{n_s q_s \vec{u}_s \times \vec{B}}_{\vec{F}_B} + \underbrace{n_s m_s \nu_{s,n}(\vec{u}_n - \vec{u}_s)}_{\vec{F}_{Fr}}.$$

Theoretically, a motionless neutral gas ($\vec{u}_n = 0$) yields:

$$0 \;=\; n_s q_s \vec{E} + n_s q_s \vec{u}_s \times \vec{B} - n_s m_s \nu_{s,n} \vec{u}_s \;=\; q_s \left(\vec{E} + \vec{u}_s \times \vec{B}\right) - m_s \nu_{s,n} \vec{u}_s.$$

If we apply a coordinate system where $\vec{B} = B\vec{e_z}$ and $\vec{E} = E\vec{e_y}$, we can write

$$\vec{u}_s \times \vec{B} \;=\; u_{ys} B \vec{e_x} - u_{xs} B \vec{e_y}.$$

This yields:

$$\begin{aligned} 0 \;&=\; q_s \left(\vec{E} + u_{ys} B \vec{e_x} - u_{xs} B \vec{e_y}\right) - m_s \nu_{s,n} \vec{u}_s \\ &=\; q_s E \vec{e_y} + q_s u_{ys} B \vec{e_x} - q_s u_{xs} B \vec{e_y} - m_s \nu_{s,n} u_{xs} \vec{e_x} - m_s \nu_{s,n} \vec{e_y} \end{aligned}$$

Separating for the x-component and for the y-component results in:

$$\begin{array}{rrcl} I: & 0 &=& q_s u_{ys} B - m_s \nu_{s,n} u_{xs} \\ II: & 0 &=& q_s E - q_s u_{xs} B - m_s \nu_{s,n} u_{ys} \\ I: & u_{ys} &=& \dfrac{m_s \nu_{s,n} u_{xs}}{q_s B} \qquad \rightarrow \; II \\ II: & 0 &=& q_s E_\perp - q_s u_{xs} B - \dfrac{m_s^2 \nu_{s,n} u_{xs}}{q_s B} \\ II: & 0 &=& q_s E_\perp - u_{xs} \dfrac{q_s^2 B^2 + m_s^2 \nu_{s,n}}{q_s B} \end{array}$$

Replacing $\omega_{sB} = |q_s|\, B \,/\, m_s$ yields:

$$\begin{aligned} u_{xs} \;&=\; \frac{q_s^2 E_\perp B}{q_s^2 B^2 + m_s^2 \nu_{s,n}} \overset{\omega_{sB}}{\overbrace{=}} \frac{q_s^2 E_\perp B}{\left(\dfrac{q_s^2 B^2 m_s^2}{m_s^2} + m_s^2 \nu_{s,n}\right)} \\ u_{xs} \;&=\; \frac{q_s^2 E_\perp B}{m_s^2 \left(\omega_{sB}^2 + \nu_{s,n}\right)} \\ u_{xs} \;&=\; \frac{\omega_{sB}^2 E_\perp}{\left(\omega_{sB}^2 + \nu_{s,n}^2\right) B} \end{aligned} \tag{D.2}$$

And for the other component:

$$\begin{aligned}
I: &\qquad 0 = q_s u_{ys} B - m_s \nu_{s,n} u_{xs} \\
II: &\qquad 0 = q_s E - q_s u_{xs} B - m_s \nu_{s,n} u_{ys} \\
I: &\qquad u_{xs} = \frac{q_s B}{m_s \nu_{s,n}} u_{ys} \qquad \rightarrow II \\
II: &\qquad 0 = q_s E_\perp - \frac{q_s^2 B^2}{m_s \nu_{s,n}} u_{ys} - m_s \nu_{s,n} u_{ys} \\
&\qquad 0 = q_s E_\perp - u_{ys} \frac{q_s^2 B^2 + m_s^2 \nu_{s,n}}{m_s \nu_{s,n}}
\end{aligned}$$

$$\begin{aligned}
u_{ys} &= \frac{q_s E_\perp m_s \nu_{s,n}}{\left(q_s^2 B^2 + m_s \nu_{s,n}\right)} \\
u_{ys} &= \frac{q_s E_\perp \nu_{s,n}}{m_s \left(\frac{q_s^2 B^2}{m_s^2} + \nu_{s,n}\right)} \\
u_{ys} &= \frac{q_s E_\perp \nu_{s,n} \left|q_s\right| B}{\left|q_s\right| B m_s \left(\omega_{sB}^2 + \nu_{s,n}^2\right)} \\
u_{ys} &= \frac{q_s}{\left|q_s\right|} \frac{E_\perp}{B} \frac{\nu_{s,n} \omega_{sB}}{\left(\omega_{sB}^2 + \nu_{s,n}^2\right)} \qquad \text{(D.3)}
\end{aligned}$$

To express the Hall conductivity we have to consider that $\vec{J}_H \perp \vec{B}$ and $\vec{J}_H \perp \vec{E}$, i.e. $\vec{J}_H$ is parallel to the x-direction: $\vec{J}_H \,||\, \vec{e_x}$. Therefore, it is: $u_K^s = u_H^s = u_x^s$. Then it applies with Eq. (D.1), Eq. (D.2), and Eq. (D.3):

$$\sigma_H = en \left| \frac{\omega_{iB}^2}{\left(\omega_{iB}^2 + \nu_{i,n}^2\right) B} - \frac{\omega_{eB}^2}{\left(\omega_{eB}^2 + \nu_{e,n}^2\right) B} \right| = \frac{en}{B} \left| \underbrace{\frac{\omega_{iB}^2}{\left(\omega_{iB}^2 + \nu_{i,n}\right)}}_{a} - \underbrace{\frac{\omega_{eB}^2}{\left(\omega_{eB}^2 + \nu_{e,n}^2\right)}}_{b} \right|$$

We can assume: $m_i >> m_e \hookrightarrow \omega_{iB} << \omega_{eB} \hookrightarrow a << b$. Therefore, σ_H can be expressed:

$$\sigma_H = \frac{en}{B} \left\{ \frac{\omega_{eB}^2}{\left(\omega_{eB}^2 + \nu_{e,n}^2\right)} - \frac{\omega_{iB}^2}{\left(\omega_{iB}^2 + \nu_{i,n}^2\right)} \right\} \qquad \text{(D.4)}$$

We know that the Pedersen conductivity requires $\vec{J}_P \perp \vec{B}$ and $\vec{J}_P \,||\, \vec{E}$, i.e. $\vec{J}_P$ is parallel to the y-direction: $\vec{J}_P \,||\, \vec{e_y}$: $\hookrightarrow u_K^s = u_P^s = u_y^s$:

$$\sigma_P \;=\; en\left|\frac{q_i \nu_{i,n}\omega_{iB}}{|q_i|\,B\left(\omega_{iB}^2+\nu_{i,n}^2\right)} - \frac{q_e}{|q_e|\,B}\frac{\nu_{e,n}\omega_{eB}}{\left(\omega_{eB}^2+\nu_{e,n}^2\right)}\right|$$

Setting $q_i = e$; $q_e = -e$, and $m_i >> m_e \hookrightarrow \omega_{iB} << \omega_{eB}$ results in:

$$\begin{aligned}\sigma_P &= \frac{en}{B}\left\{\frac{\nu_{i,n}\omega_{iB}}{\left(\omega_{iB}^2+\nu_{i,n}^2\right)} - \frac{-e}{|e|}\frac{\nu_{e,n}\omega_{eB}}{\left(\omega_{eB}^2+\nu_{e,n}^2\right)}\right\}\\ \sigma_P &= \frac{en}{B}\left\{\frac{\nu_{e,n}\omega_{eB}}{\left(\omega_{eB}^2+\nu_{e,n}^2\right)} + \frac{\nu_{i,n}\omega_{iB}}{\left(\omega_{iB}^2+\nu_{i,n}^2\right)}\right\} \qquad \text{(D.5)}\end{aligned}$$

For the Birkeland conductivity (parallel conductivity) the electric field is parallel to the magnetic field: $\vec{E}\,||\,\vec{B}$. We can start again from Ohm's law with $k = B$:

$$j_B \;=\; \sigma_B E_{||} \;\rightarrow\; \sigma_B \;=\; en\left|\vec{u}_{||}^{i} - \vec{u}_{||}^{e}\right|/E_{||}$$

Again, we can use the force balance relations for charged particles. However, for Birkeland currents, the magnetic force has no effect, since it acts perpendicular to the x-y-plane whilst we are only interested in the parallel (i.e. in the x-y-plane) component. As before, we assume not to have collisions between charged particles themselves, but only between charged particles and neutrals. Hence, the energy balance equation yields:

$$\underbrace{n_s q_s \vec{E}_{||}}_{\vec{F_E}} + \underbrace{n_s m_s \nu_{s,n}\left(\vec{u}_n^{||} - \vec{u}_s^{||}\right)}_{\vec{F_{Fr}}} \;=\; 0 \qquad \text{(D.6)}$$

For a motionless neutral gas ($\vec{u}_n^{||} = 0$) we derive:

$$n_s q_s \vec{E}_{||} - n_s m_s \nu_{s,n}\vec{u}_s^{||} \;=\; 0 \;\Rightarrow\; u_s^{||} \;=\; \frac{q_s}{m_s \nu_{s,n}}E_{||} \qquad \text{(D.7)}$$

Using this term in the expression $\sigma_{||} \;=\; en\left|\vec{u}_{||}^{i} - \vec{u}_{||}^{e}\right|/E_{||}$ yields:

$$\sigma_{||} \;=\; \frac{en}{E_{||}}\left(\frac{eE_{||}}{m_i\nu_{i,n}} + \frac{eE_{||}}{m_e\nu_{e,n}}\right) \;=\; e^2 n\left(\frac{1}{m_i\nu_{i,n}} + \frac{1}{m_e\nu_{e,n}}\right). \qquad \text{(D.8)}$$

The same expressions for σ_P and σ_H have been received by Schlegel (1988), setting $n = n_e$. This corresponds to our assumption that $n_i \cong n_e = n$, but simplifies the situation since we can derive n_e directly from the EISCAT measurements.

Bibliography

[1] Appleton, E. V. and L. J. Ingram: Magnetic storms and upper atmospheric ionisation, Nature, 136, 548–549, 1935.

[2] Aruliah, A. L., E. M. Griffin, A. D. Aylward, E. A. K. Ford, M. J. Kosch, C. J. Davis, V. S. C. Howells, S. E. Pryse, H. R. Middleton and J. Jussila: First direct evidence of meso-scale variability on ion neutral dynamics using co-located tristatic FPIs and EISCAT radar in Northern Scandinavia, Ann. Geophys., 23, 147–162, 2005.

[3] Bilitza, D. and B. Reinisch: International reference ionosphere 2007: Improvements and new parameters, J. Adv. Space Res., doi:10.1016/J.ASR.2007.048, 2008.

[4] Binder, U.: Auswirkung der Satellitenbahn und -lage auf die Thermosphärenmessungen, Diplomarbeit im Fach Meteorologie, Freie Universität Berlin/GFZ Potsdam, 2005.

[5] Boulton, W. J.: The determination and analysis of the orbit of Nimbus 1 rocket, 1964-52b: The semi-annual variation in air density from June 1968 to August 1974, Planet. Space Sci., 33, 1417–1431, 1985.

[6] Bowles, K. L.: Observations of vertical incidence scatter from the ionosphere at 41 Mc/sec, Phys. Rev. Lett., 1, 454–455, 1958.

[7] Bruce, R. W.: Upper atmospheric density determination from LOGACS, in The Low-G Accelerometer Calibration System, Vol. II, Rept. No. TR-0074(4260-10), Vol. II, The Aerospace Corp., El Segundo, CA, 1-1 – 1-43, 1973.

[8] Bruinsma, S. D., D. Tamagnan and R. Biancale: Atmospheric densities derived from CHAMP/STAR accelerometer observations, Planet. Space Sci., 52, 297–312, 2004.

[9] Buchert, S. C., T. Tsuda, R. Fujii and S. Nozawa: The Pedersen current carried by electrons: a non-linear response of the ionosphere to magnetospheric forcing, Ann. Geophys., 26, 2837–2844, 2008.

[10] Chapman, S. and J. Bartels: Geomagnetism, 2 Vols., Clarendon Press, Oxford, 1940.

[11] Chapman, S. and V. C. A. Ferraro: A new theory of magnetic storms, 1, The initial phase (continued), J. Geophys. Res., 36, 171–, 1931b.

[12] Chapman, S. and V. C. A. Ferraro: A new theory of magnetic storms, 1, The initial phase, J. Geophys. Res., 36, 77–97, 1931a.

[13] Chisham, G., M. Pinnock, I. J. Coleman, M. R. Hairshon and A. D. M. Walker: An unusual geometry in the ionospheric signature of the cusp: Implications for magnetopause merging sites, Ann. Geophys, 20, 29–40, 2002.

[14] Codrescu, M. V., T. J. Fuller-Rowell, J. C. Foster, J. M. Holt and S. J. Cariglia: Electric field variability associated with the Millstone Hill electric field model, J. Geophys. Res., 105, 5265–5273, 2000.

[15] Crowley, G., A. Reynolds, J. P. Thayer, J. Lei, L. J. Paxton, A. B. Christensen, Y. Zhang, R. R. Meier and D. J. Strickland: Periodic modulations in thermospheric composition by solar wind high speed streams, Geophys. Res. Lett., 35 (I.21106), doi:10.1029/2008GL035745, 2008.

[16] Demars, H. G., and Schunk, R. W.: Thermospheric response to ion heating in the dayside cusp, J. of Atm. and Sol.-Terr. Phys., 69, 649–660, 2007.

[17] Flury, W.: Space debris, ESA Publications, 4 (4), 1994.

[18] Frank, L. A.: Plasma in the Earth's polar magnetosphere, J. Geophys. Res., 76, 5202–5219, 1971.

[19] Förste, C. and S. Choi: CHAMP accelerometer preprocessing at GeoForschungsZentrum Potsdam, in Reigber, C., H. Lühr, P. Schwintzer and J. Wickert (Eds.): Earth observation with CHAMP - Results from three years in orbit, 169–174, 2005.

[20] Förster, M., S. Rentz, W. Köhler, H. Liu and E. E. Haaland: IMF dependence of high-latitude thermospheric wind pattern derived from CHAMP cross-track measurements, Ann. Geophys., 26, 1581–1595, 2008.

[21] Fuller-Rowell, T. J.: The "thermospheric spoon": A mechanism for the semiannual density variation, J. Geophys. Res., 103, 3951–3956, doi:10.1029/97JA03335, 1998.

[22] Gordon, D.: Incoherent scattering of radio waves by free electrons with application to space exploration by radar, Proc. IRE, 46, 1824–1829, 1958.

[23] Guo, J., W. Wan, J. M. Forbes, E. Sutton, R. S. Nerem, T. N. Woods, S. Bruinsma and L. Liu: Effects of solar variability on thermosphere density from CHAMP accelerometer data, J. Geophys. Res., Vol. 112 (A10308), doi:10.1029/2007JA12409, 2007.

[24] Hedin, A. E.: Extension of the MSIS thermosphere model into the middle and lower atmosphere, J. Geophys. Res., 96, 1159–1172, 1991.

[25] Hedin, A. E.: MSIS-86 thermospheric model, J. Geophys. Res., 92, 4649–4662, 1987.

[26] Heikkilä, W. J. and J. D. Winningham: Penetration of magnetosheath plasma to lower altitudes through the dayside magnetospheric cusps, J. Geophys. Res., 76, 883–891, 1971.

[27] Ishii, M., M. Suigiura, T. Iyemori and J. A. Slavin: Correlation between magnetic and electric field perturbations in the field-aligned current regions deduced from DE-2 observations, J. Geophys. Res., 97 (A9), 13877-13887, 1992.

[28] Jacchia, L. G.: Static diffusion models of the upper atmosphere, Smithsonian Astrophysical Observatory, Special Report No. 170, Cambridge, MA, 1964.

[29] Jacchia, L. G.: A working model for the upper atmosphere, Nature, 192, 1147–1148, 1961.

[30] Jacchia, L. G.: Solar effects on the acceleration of artificial satellites, Smithsonian Astrophysical Observatory, Special Report No. 29, Cambridge, MA, 1959.

[31] Jacchia, L. G. and J. Slowey: Atmospheric heating in the auroral zones: a priliminary analysis of the atmospheric drag of the Injune 3 satellite, J. Geophys. Res., 69 (5), 905–910, 1964.

[32] Jacchia, L. G. and J. Slowey: Atmospheric heating in auroral zones, Smithsonian Astrophysical Observatory, Special Report No. 136, Cambridge, MA, 1963.

[33] Jacobs, R. L.: Atmospheric density derived from the drag of eleven low altitude satellites, J. Geophys. Res., 72 (5), 1571–1581, 1967.

[34] Jee, G., A. G. Burns, W. Wang, S. C. Solomon, R. W. Schunk, L. Scherliess, D. C. Thompson, J. J. Sojka and L. Zhu: Driving the TING model with GAIM electron densities: Ionospheric effects of the thermosphere, J. Geophys. Res., 113 (A03305), doi:10.1029/2007JA012580, 2008.

[35] Kan, J. R. and L. C. Lee: Energy coupling function and solar wind magnetosphere dynamo, Geophys. Res. Lett., 6, 577–580, 1979.

[36] Kelley, M. C.: The Earth's ionosphere, San Diego Academic Press, 1989.

[37] Killeen, T. L., P. B. Hays, G. R. Carignan, R. A. Heelis, R. A. Hanson, N. W. Spencer and L. H. Brace: Ion-neutral coupling in the high-latitude F region: Evaluation of ion heating terms from Dynamics Explorer 2, J. Geophys. Res., 89, 7495–7508, 1984.

[38] Killeen, T. L. and R. G. Roble: Thermospheric dynamics: Contributions from the first 5 years of Dynamics Explorer program, Rev. Geophys., 26, 329–367, 1988.

[39] Killeen, T. L., Y.-I. Won, R. J. Niciejewski and A. G. Burns: Upper thermosphere winds and temperatures in the geomagnetic polar cap: solar cycle, geomagnetic activity, and interplanetary magnetic field dependencies, J. Geophys. Res., 100, 21327–21342, 1995.

[40] Kremser, G. and R. Lundin: Average spatial distributions of energetic particles in the midlatitude cusp/cleft region observed by Viking, J. Geophys. Res., 95, 5753–5766, 1990.

[41] Lathuillère, C., M. Menvielle, A. Marchaudon and S. Bruinsma: A statistical study of the observed and modeled global thermosphere response to magnetic activity at middle and low latitudes, J. Geophys. Res., 113 (A07311), doi:10.1029/2007JA012991, 2008.

[42] Lathuillère, C. and A. Brekke: Ion compositions in the auroral ionosphere as observed by EISCAT, Ann. Geophys., 3, 557–567, 1985.

[43] Lehtinen M. and A. Huuskonen: General incoherent scatter analysis und GUISDAP, J. Atmos. Terr. Phys., 58, 435–452, 1996.

[44] Lei, J., J. P. Thayer, J. M. Forbes, E. Sutton and R. S. Nerem: Rotating solar coronal holes and periodic modulation of the upper atmosphere, Geophys. Res. Lett., 35 (L10109), 2008.

[45] Liu, H. and H. Lühr: Strong disturbance of the upper thermospheric density due to magnetic storms: CHAMP observations, J. Geophys. Res., 110 (A09S29), doi: 10.1029/JA010908, 2005.

[46] Liu, H., H. Lühr and S. Watanabe: Climatology of the equatorial thermospheric mass density anomaly, J. Geophys. Res., 112 (A05305), doi: 10.1029/2006JA012199, 2007.

[47] Liu, H., H. Lühr, S. Watanabe, V. Henize and P. Visser: Zonal wind in the equatorial upper thermosphere: Decomposing the solar flux geomagnetic activity, and seasonal dependences, J. Geophys. Res., 111 (A07307), doi:10.1029/2005JA011415, 2006.

[48] Liu H., H. Lühr, V. Henize and W. Köhler: Global distribution of the thermospheric total mass density derived from CHAMP, J. Geophys. Res., 110 (A04301), doi:10.1029/2004JA010741, 2005.

[49] Liu, L., W. Wan, B. Ning, O. M. Pirog and V. I. Kurkin: Solar activity variation of the ionospheric peak electron density, J. Geophys. Res., 111 (A08304), doi:10.1029/2006JA011598, 2006.

[50] Lühr, H., S. Rentz, P. Ritter, H. Liu, K. Häusler: Average thermospheric wind patterns over the polar regions, as observed by CHAMP, Ann. Geophys., 25, 1093–1101, 2007.

[51] Lühr, H. and S. Maus: Direct observation of the F region dynamo currents and the spatial structure of the EEJ by CHAMP, Geophys. Res. Lett., 33 (L24102), doi:10.1029/2006GL028374, 2006.

[52] Lühr, H., M. Rother, W. Köhler, P. Ritter and L. Grunwaldt: Thermospheric up-welling in the cusp region: Evidence from CHAMP observations, Geophys. Res. Lett., 31 (L06805), doi:10.1029/2003GL019314, 2004.

[53] Maruyama, N., S. Watanabe and T. J. Fuller-Rowell: Dynamic and energetic coupling in the equatorial ionosphere and thermosphere, J. Geophys. Res., 108 (A11), doi:10.1029/2002JA009599, 1396–1404, 2003.

[54] Maus, S., M. Rother, W. Mai, S. Choi, H. Lühr: Third generation of the Potsdam magnetic model of the earth (POMME), Geophysics Geosystems, 7 (Q07008), doi:10.1029/2006/GC001269, 2006.

[55] Maus, S., S. Macmillan, T. Chernov, S. Choi, D. Dater, V. Glovkov, V. Lesur, F. Lowes, H. Lühr, W. Mai, S. McLean, N. Olsen, M. Rother, T. Sabaka, A. Thomson, T. Zvereva (International Association of Geomagnetism, and Division V Working Group VMOD: Geomagnetic Field Modeling) Aeronomy (IAGA): The 10th generation international geomagnetic reference field, Geophys. J. Int., 161, 561–565, 2005.

[56] McCormac, F. G. and R. W. Smith: The influence of the Interplanetary Magnetic Field Y component on the ion and neutral motions in the polar thermosphere, Geophys. Res. Lett., 11, 935–938, 1984.

[57] Millward, G. H., R. J. Moffett, H. F. Balmforth and A. S. Rodger: Modeling the ionospheric effects of ion and electron precipitation in the cusp, J. Geophys. Res., 104 (A11), 24603–24612, 1999.

[58] Millward, G. H., R. J. Moffett, S. Quegan and T. J. Fuller-Rowell: A coupled thermosphere-ionosphere-plasmasphere model (CTIP), In R. W. Schunk, Editor, Handbook of Ionospheric Models, 1996.

[59] Mitra, S. K.: The upper atmosphere, The Royal Asiatic Society of Bengal, Calcutta, 91–92, 131–143 and 417–418, 1947.

[60] Moe, K., M. M. Moe, V. L. Carter and M. B. Ruggera Jr.: The correlation of thermospheric densities with charged particle precipitation through the magnetospheric cleft, J. Geophys. Res., 82 (22), 3304–3306, 1977.

[61] Moe, K. and M. M. Moe: A dynamic model of the neutral thermosphere, Rep. MDLG5891, Mc Donnell Douglas Astronaut. Co., Huntington Beach, Calif., Sept. 1975.

[62] Müller, S., H. Lühr and S. Rentz: Solar and magnetospheric forcing of the low latitude thermospheric mass density as observed by CHAMP, submitted to Ann. Geophys., 2008.

[63] Newell, P. T., W. J. Burke, C. I. Meng, E. R. Sanchez and M. E. Greenspan: Identification and observation of the plasma mantle at low altitude, J. Geophys. Res., 96 (A1), 35–45, 1991.

[64] Newell, P. T. and C. I. Meng: Cusp low-energy ion cutoffs: A survey and implications for merging, J. Geophys. Res., 100, 21943–21951, 1995.

[65] Newell P. T. and C. I. Meng: Mapping the dayside ionosphere to the magnetosphere according to particle precipitation characteristics, Geophys. Res. Lett., 19 (6), 609–612, 1992.

[66] Newell, P. T. and C. I. Meng: Ion acceleration at the equatorward edge of the cusp: low altitude observations of patchy merging, Geophys. Res. Lett., 18 (10), 1829–1832, 1991.

[67] Newell, P. T. and C. I. Meng: The cusp and the cleft/boundary layer: low-altitude identification and statistical local time variation, J. Geophys. Res., 93 (A12), 14549–14556, 1988.

[68] Neubert, T. and F. Christiansen: Small-scale, field-aligned currents at the topside ionosphere, Geophys. Res. Lett., 30 (19), doi:10.1029/2003GL017808, 2010-2013, 2003.

[69] Nicolet, M.: Properties and constitution of the Earth's upper atmosphere, in Ratcliffe, J.A. (Ed.), Physics of the Upper Atmosphere, Academic Press, NY and London, 17–71, 1960.

[70] Olson, W. P.: Corpuscular radiation as an upper atmospheric energy source, in Space Research XII, b, Akademie-Verlag, Berlin, 1007–1013, 1972.

[71] Pätzold, H.-K.: Model for the variability of the terrestrial atmosphere after satellite acceleration, U. of Cologne (1962); reprinted in Flight Performance Handbook for Orbital Operations, Wolverton, R.W. (Ed.), John Wiley, NY and London, 2-430 – 2-356, 1963.

[72] Picone, J. M., A. E. Hedin, D. P. Drob and A. C. Aikin: NRLMSISE-00 empirical model of the atmosphere: Statistical comparisons and scientific issues, J. Geophys. Res., 107 (A12), 1468, doi:10.1029/2002JA009430, 2002.

[73] Prölss, G. W.: Electron temperature enhancement beneath the magnetospheric cusp, J. Geophys. Res., 111, A07304, doi:10.1029/2006JA011618, 2006.

[74] Prölss, G. W.: Physik des erdnahen Weltraums - Eine Einführung, Springer-Verlag, Berlin, Heidelberg, New York, 2001.

[75] Reigber, C., H. Lühr, P. Schwintzer and J. Wickert: Earth observation with CHAMP - Results from three years in orbit, Springer-Verlag, Berlin, Heidelberg, New York, 2005.

[76] Reigber, C., H. Lühr and P. Schwintzer: First CHAMP mission results for gravity, magnetic and atmospheric studies, Springer-Verlag, Berlin, Heidelberg, New York, 2003.

[77] Reigber, C., H. Lühr and P. Schwintzer: CHAMP mission status, Adv. Space Res., 30, 129–134, 2002.

[78] Rentz, S.: Die globale Dichteverteilung in der Thermosphäre, Diplomarbeit in Meteorologie, Freie Universität Berlin/GFZ Potsdam, 2005.

[79] Richards, P. G., J. A. Fennelly and D. G. Torr: EUVAC: A solar EUV flux model for aeronomic calculations, J. Geophys. Res., 99, 8981–8992, 1994.

[80] Richmond, A. D.: Ionospheric electrodynamics using magnetic Apex coordinates, J. Geomagn. Geoelectr., 47, 191–212, 1995.

[81] Rishbeth, H., K. J. F. Sedgemore-Schulthess and T. Ulich: Semiannual and annual variations in the height of the ionospheric F2-peak, Ann. Geophys., 18, 285–299, 2000.

[82] Ritter, P., H. Lühr and S. Rentz: The heating efficiency of medium- and large-scale field-aligned currents at auroral latitudes, COSPAR-2008 D36 P083, 2008.

[83] Ritter, P., H. Lühr, S. Maus and A. Viljanen: High latitude ionospheric currents during very quiet times: their characteristics and predictabilities, Ann. Geophys., 22, 2001–2014, 2004b.

[84] Ritter, P., H. Lühr, A. Viljanen, O. Amm, A. Pulkkinen and I. Sillanpää: Ionospheric currents estimated simultaneously from CHAMP satellite and IMAGE ground-based magnetic field measurements: A statistical study at auroral latitudes, Ann. Geophys., 22, 417–430, 2004a.

[85] Roble, R. G., B. A. Emery, R. E. Dickinson, E. C. Ridley, T. L. Killeen, P. B. Hays, G. R. Carignan and N. W. Spencer: Thermospheric circulation, temperature and compositional structure of the Southern Hemisphere polar cap during October-November, 1981, J. Geophys. Res., 89, 9057–9068, 1984.

[86] Roh, K.-M., H. Lühr, M. Rothacher and S.-Y. Park: Investigating suitable orbits for the Swarm constellation mission - The frozen orbit, J. Aerospace Sci. and Technology, doi:10.1016/j.ast.2008.03.001, 2008 (in press).

[87] Rosenbauer, H., H. Grünwaldt, M. D. Montgomery, G. Paschmann and N. Schkopke: HEOS 2 plasma observations in the distant polar magnetosphere: The plasma mantle, J. Geophys. Res., 80 (19), 2723–2737, 1975.

[88] Rother, M., K. Schlegel and H. Lühr: CHAMP observation of intense kilometre-scale field-aligned currents, evidence for an ionospheric Alfvén resonator, Ann. Geophys., 25, 1603–1615, 2007.

[89] Russell, C. T.: The polar cusp, Adv. Space Res., 25(7/8), 1413–1424, 2000.

[90] Russell, C. T., C. R. Chappell, M. D. Montgomery, M. Neugebauer and F. L. Scarf: OGO-5 observations of the polar cusp on Nov 1, 1968, J. Geophys. Res., 76 (28), 6743, 1971.

[91] Schlegel, K., H. Lühr, J. P. St.-Maurice, G. Crowley and C. Hackert: Thermospheric density structures over the polar regions observed with CHAMP, Ann. Geophys., 23, 1659–1672, 2005.

[92] Schlegel, K: Auroral E-region conductivities during solar minimum derived from EISCAT data, Ann. Geophys., 6, 129–138, 1988.

[93] Schunk, R. W. and A. F. Nagy: Electron temperature in the F region of the ionosphere, theory, observations, Rev. Geophys. Space Phys., 16 (4), 355–399, 1978.

[94] Schunk, R. W. and J. C. G. Walker: Theoretical ion densities in the lower ionosphere, Planet. Space Sci., 21, 1875–1896, 1973.

[95] Smith, R. W.: Vertical winds: A tutorial, J. Atmos. Terr. Phys., 60, 1425–1434, 1998.

[96] Strickland, D. J., R. E. Daniell and J. D. Craven: Negative ionospheric storm coincident with DE-1 observed thermospheric disturbance on October 14, 1981, J. Geophys. Res., 106, 21049–21062, 2001.

[97] Strickland, D. J., J. S. Evans and L. J. Paxton: Satellite remote sensing of thermospheric O/N2 and solar EUV, 1, Theory, J. Geophys. Res., 100, 12217–12226, 1995.

[98] Stubbe, P.: The ionosphere as a plasma laboratory, in Modern Ionospheric Science, Kohl, H., R. Rüster and K. Schlegel (Eds.), European Geophysical Society, Katlenburg-Lindau, FRG, 274–321, 1996.

[99] Sutton, E. K., J. M. Forbes and R. S. Nerem: Global thermospheric neutral density and wind response to the severe 2003 geomagnetic storms from CHAMP accelerometer data, J. Geophys. Res., Vol. 110 (A09S40), doi:10.1029/2004JA010985, 2005.

[100] Temmer, M., B. Vršnak and A. M. Veronig: Periodic appearance of coronal holes and the related variation of solar wind parameters, Sol. Phys., 241, 371–383, 2007.

[101] Thayer, J. P., T. L. Killeen, F. G. McCormac, C. R. Tschan, J.-J. Ponthieu and N. W. Spencer: Thermospheric neutral wind signatures dependent on the East-West component of the interplanetary magnetic field for northern and southern hemispheres, as measured from Dynamics Explorer-2, Ann. Geophys., 5, 363–368, 1987.

[102] Vennerstrøm, S., T. Moretto, N. Olsen, E. Friis-Christensen, A. M. Stampe and J. F. Watermann: Field-aligned currents in the dayside cusp and polar cap region during northward IMF, J. Geophys. Res., 107 (A8), doi:10.1029/2001JA009162, 2002.

[103] Vogt, J.: Alfvén wave coupling in the auroral current circuit, Surv. Geophys., 23, 335–377, 2002.

[104] Vršnak, B., M. Temmer and A. M. Veronig: Coronal holes and solar wind high-speed streams: I. Forecasting the solar wind parameters, Sol. Phys., 240, 315–330, 2007.

[105] Wang, H., H. Lühr and S. Y. Ma: Solar zenith angle and merging electric field control of field-aligned currents: a statistical study of the southern hemisphere, J. Geophys. Res., 110, doi:10.1029/2004JA010530, 2005.

[106] Watermann, J.: SIRCUS Workshop Report, OIST-4 Proceedings, 4th OERSTED International Science Team Conference, DMI Scientific Report, 03–09, 327–334, 2003.

[107] Weimer, D. R.: An improved model of ionospheric electric potentials including substorm perturbations and application to the Geospace Environment Modeling November 24, 1996, event, J. Geophys. Res., 106 (A1), 407–416, 2001.

[108] Weimer, D. R.: Models of high-latitude electric potentials derived with a least error fit of spherical harmonic coefficients, J. Geophys. Res., 100 (A10), 19595–19607, 1995.

[109] Yeoman, T. K. , L. J. Baddeley, R. S. Dhillon, T. R. Robinson and D. M. Wright: Bistatic observations of large and small scale ULF waves in SPEAR-induced HF coherent backscatter, Ann. Geophys., 26, 2253–2263, 2008.

[110] Yordanova, E., D. Sundkvist, S. C. Buchert, M. André, Y. Ogawa, M. Morooka, O. Margithu, O. Amm, A. N. Fazakerley and H. Réme: Energy input from the exterior cusp into the ionosphere: correlated ground-based and satellite observations, Geophys. Res. Lett., 34 (L04102), doi:10.1029/2006GL028617, 2007.

[111] Zhou, X.-W., C. T. Russell, G. Le, S. A. Fuselier and J. D. Scudder: The polar cusp location and its dependence on dipole tilt, Geophys. Res. Lett., 26 (3), 429–432, 1999.

[112] Zhu, X., E. R. Talaat, J. B. H. Baker and J.-H. Yee: A self-consistent derivation of ion drag and Joule heating for atmospheric dynamics in the thermosphere, Ann. Geophys., 23, 3313–3322, 2005.

[113] Zou, L., H. Rishbeth, I. C. F. Müller-Wodarg, A. D. Aylward, G. H. Millward, T. J. Fuller-Rowell, D. W. Idenden and R. J. Moffett: Annual and semiannual

variations in the ionospheric F2-layer I. Modelling, Ann. Geophys., 18, 927–944, 2000.

Acknowledgements

First of all I would like to thank Prof. Dr. Hermann Lühr for initiating this thesis and giving me the chance to work on that challenging research topic. Thank you very much for the intensive supervision, countless times of insightful conversation and many helpful ideas as well as the time discussing them.

My special Thanks to the GFZ Section 2.3 members for providing the opportunity to learn and work in a great environment full of stimulating ideas and kind assistance. To those who feel addressed as C3 people - Thank you so much for the broad and patient support, cooperation and helpfulness.

I wish to thank Prof. Dr. Gerd W. Prölss and Prof. Dr. Andreas Hördt for taking over the task to review this thesis. I would also like to thank Prof. Dr. Uwe Motschmann, Prof. Dr. Jürgen Blum, Frauke Zottmann and Elisabeth Vogel at the Technische Universität Carolo-Wilhelmina zu Braunschweig for their help getting through the bureaucratic system at the university.

I would like to thank Wolfgang Köhler for pre-processing the CHAMP data. Many thanks to Dr. Patricia Ritter for her contribution with magnetometer and Hall current data, for the help with all the practical questions and MATLAB advices which made life so much easier. I am grateful to Dr. Martin Rother for providing Fig. 4.1 and the FAC data, and for being this amazingly patient to fix any kind of technical problems.

Thanks to Martin Langteigen, Halvard Boholm, Dr. Mike Rietveld, Prof. Tony van Eyken from EISCAT and to Dr. Matthias Förster for their kind assistance and helpful support during my stay on Svalbard. EISCAT is an international association supported by research organisations in China (CRIRP), Finland (SA), France (CNRS, till end 2006), Germany (DFG), Japan (NIPR and STEL), Norway (NFR), Sweden (VR), and the United Kingdom (PPARC). I am grateful to Prof. Dr. Kristian Schlegel for his help with calculating the conductivities.

A huge Danke/Obrigada to my roommates Kathrin and Ana, and to Christina, for the cheeriness they brought to our working days, for proofreading, and for the innumerable hours spend with brainstorming to solve any kind of problems. Thanks to Jörn F. Hanusch for further proofreading.

I am obliged to the ACE MAG and SWEPAM instrument teams and the ACE Science Center for providing the ACE data. The operational support of the CHAMP mission by the German Aerospace Centre (DLR), the financial support for the data processing by the Federal Ministry of Education and Research (BMBF), as part of the Geotechnology Programme, and the work of Community Coordinated Modeling Centre (CCMC), enabling access to various models, are gratefully acknowledged.

This work was supported by the Deutsche Forschungsgemeinschaft DFG through the DFG Priority Programme "CAWSES", SPP 1176. Thanks to Prof. Dr. Franz-Josef Lübken and the German CAWSES group for the comfortable host and inspiring environment.

Nicht unerwähnt bleiben sollen Frank, meine Freunde und meine wunderbare Familie. Ich danke Euch von Herzen für die grenzenlose Unterstützung und Motivation, dafür, dass Ihr an mich glaubt und mir vermittelt habt, was wirklich wichtig ist im Leben. Gut zu wissen, dass man den Schritt allein machen, aber den Weg nicht allein gehen muss.

Curriculum Vitae

PERSÖNLICHE DATEN

Name	Stefanie Rentz
Geburtsdatum	06. August 1979
Geburtsort	Brandenburg
Staatsangehörigkeit	deutsch

SCHULBILDUNG

1986 – 1991	Karl–Marx–Oberschule Lehnin
1991 – 1992	Grundschule Lehnin
1992 – 1999	Von Saldern–Gymnasium, Städtisches Gymnasium, Brandenburg a. d. Havel (allgemeine Hochschulreife)

STUDIUM

1999 – 2005	Studium der Meteorologie Freie Universität Berlin Diplom in Meteorologie

PROMOTION

Jun. 2005 – Dez. 2008	DFG CAWSES SPP 1176, Projekt 22, Helmholtz-Zentrum Potsdam, Deutsches GeoForschungsZentrum GFZ